ISTANBUL UNIVERSITY CERRAHPASA

EISSN 2619-9831

ELECTRICA

electrica.istanbul.edu.tr

Official journal of İstanbul University-Cerrahpaşa Faculty of Engineering

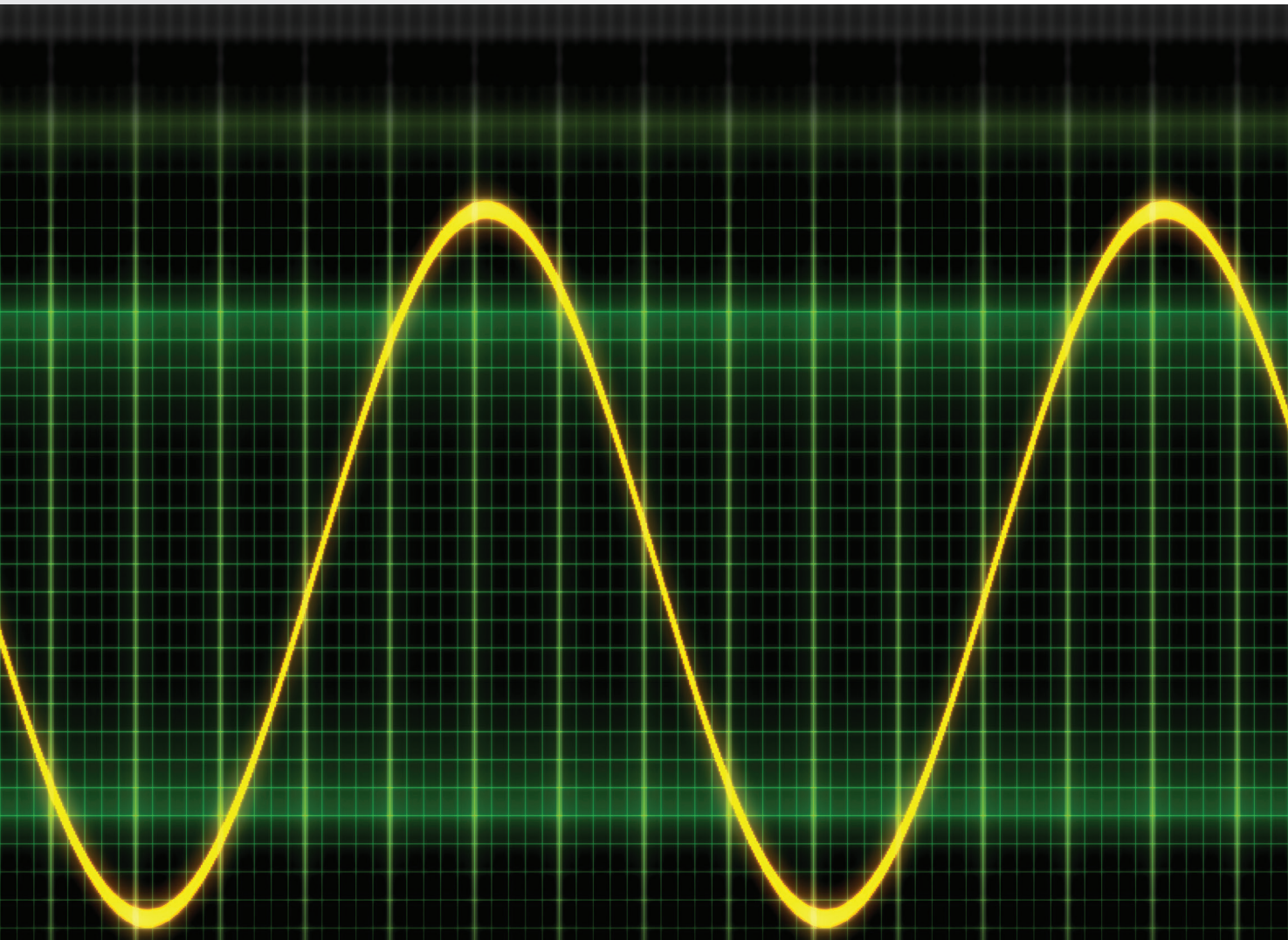

VOLUME 19 » ISSUE 1 » 2019

Editorial Board

Advisory Board

Publisher
İbrahim KARA

Publication Director
Ali ŞAHİN

Editorial Development
Gizem KAYAN

Finance and Administration
Zeynep YAKIŞIRER ÜREN

Deputy Publication Director
Gökhan ÇİMEN

Publication Coordinators
Betül ÇİMEN
Özlem ÇAKMAK
Okan AYDOĞAN
İrem DELİÇAY
Arzu YILDIRIM

Project Coordinators
Sinem KOZ
Doğan ORUÇ

Graphics Department
Ünal ÖZER
Deniz DURAN
Beyzanur KARABULUT

Contact
Address: Buyukdere Street
No: 105/9 34394
Mecidiyekoy, Sisli, Istanbul, TURKEY
Phone: +90 212 217 17 00
Fax : +90 212 217 22 92
E-mail : info@avesyayincilik.com

Aims and Scope

Electrica is an international, scientific, open access periodical published in accordance with indepen¬dent, unbiased, and double-blinded peer-review principles. The journal is the official publication of İstanbul University-Cerrahpaşa Faculty of Engineering and it is published biannually on January and July. The publication language of the journal is English.

Electrica aims to contribute to the literature by publishing manuscripts at the highest scientific level on all fields of electrical and electronics engineering. The journal publishes original research and review articles that are prepared in accordance with ethical guidelines.

The scope of the journal includes but not limited to; electronics, microwave, transmission, control sytems, electrical machines, energy transmission and high voltage.

The target audience of the journal includes specialists and professionals working and interested in all disciplines of electrical and electronics engineering.

The editorial and publication processes of the journal are shaped in accordance with the guidelines of the Institute of Electrical and Electronics Engineers (IEEE), the World Commission on the Ethics of Scientific Knowledge and Technology (COMEST), Council of Science Editors (CSE), Committee on Publication Ethics (COPE), European Association of Science Editors (EASE), and National Information Standards Organization (NISO). The journal is in conformity with the Principles of Transparency and Best Practice in Scholarly Publishing (doaj.org/bestpractice).

The journal is currently indexed in Web of Science-Emerging Sources Citation Index, Scopus, Compendex, Gale and TUBITAK ULAKBIM TR Index.

All expenses of the journal are covered by İstanbul University-Cerrahpaşa. Processing and publication are free of charge with the journal. No fees are requested from the authors at any point throughout the evaluation and publication process. All manuscripts must be submitted via the online submission system, which is available at dergipark.gov.tr/iujeee. The journal guidelines, technical information, and the required forms are available on the journal's web page.

Statements or opinions expressed in the manuscripts published in the journal reflect the views of the author(s) and not the opinions of the Electrica editors, editorial board, and/or publisher; the editors, editorial board, and publisher disclaim any responsibility or liability for such materials.

All published content is available online, free of charge at dergipark.gov.tr/iujeee. Printed copies of the journal are distributed free of charge.

OPEN ACCESS

Editor in Chief : Sıddık YARMAN
Address : İstanbul Üniversitesi -Cerrahpaşa Mühendislik Fakültesi Elektrik-Elektronik Mühendisliği Bölüm Başkanlığı Avcılar Kampüsü, Avcılar, İstanbul, Turkey
Phone : +90 212 4737070
Fax : +90 212 4737064
E-mail : sbyarman@gmail.com

Publisher : AVES
Address : Büyükdere Cad. 105/9 34394 Mecidiyeköy, Şişli, İstanbul, Turkey
Phone : +90 212 217 17 00
Fax : +90 212 217 22 92
E-mail : info@avesyayincilik.com
Web page : www.avesyayincilik.com

Instructions for Authors

Instructions for Authors

Electrica is an international, scientific, open access periodical published in accordance with indepen¬dent, unbiased, and double-blinded peer-review principles. The journal is the official publication of İstanbul University-Cerrahpaşa Faculty of Engineering and it is published biannually on January and July. The publication language of the journal is English.

Electrica aims to contribute to the literature by publishing manuscripts at the highest scientific level on all fields of electricity. The journal publishes original research and review articles that are prepared in accordance with ethical guidelines.

The scope of the journal includes but not limited to; electronics, microwave, transmission, control sytems, electrical machines, energy transmission and high voltage.

The target audience of the journal includes specialists and professionals working and interested in all disciplines of electrical and electronics engineering.

The editorial and publication processes of the journal are shaped in accordance with the guidelines of the Institute of Electrical and Electronics Engineers (IEEE), the World Commission on the Ethics of Scientific Knowledge and Technology (COMEST), Council of Science Editors (CSE), the Committee on Publication Ethics (COPE), the European Association of Science Editors (EASE), and National Information Standards Organization (NISO). The journal conforms to the Principles of Transparency and Best Practice in Scholarly Publishing (doaj.org/bestpractice).

Originality, high scientific quality, and citation potential are the most important criteria for a manuscript to be accepted for publication. Manuscripts submitted for evaluation should not have been previously presented or already published in an electronic or printed medium. The journal should be informed of manuscripts that have been submitted to another journal for evaluation and rejected for publication. The submission of previous reviewer reports will expedite the evaluation process. Manuscripts that have been presented in a meeting should be submitted with detailed information on the organization, including the name, date, and location of the organization.

Manuscripts submitted to Electrica will go through a double-blind peer-review process. Each submission will be reviewed by at least two external, independent peer reviewers who are experts in their fields in order to ensure an unbiased evaluation process. The editorial board will invite an external and independent editor to manage the evaluation processes of manuscripts submitted by editors or by the editorial board members of the journal. The Editor in Chief is the final authority in the decision-making process for all submissions.

The authors are expected to submit researches that comply with the general ethical principles which include; scientific integrity, collegiality, data integrity, institutional integrity and social responsibility.

All submissions are screened by a similarity detection software (iThenticate by CrossCheck).

In the event of alleged or suspected research misconduct, e.g., plagiarism, citation manipulation, and data falsification/fabrication, the Editorial Board will follow and act in accordance with COPE guidelines.

Authorship

Being an author of a scientific article mainly indicates a person who has a significant contribution to the article and shares the responsibility and accountability of that article. To be defined as an author of a scientific article, researchers should fulfil below criteria:

- Making a significant contribution to the work in all or some of the following phases: Research conception or design, acquisition of data, analysis and interpretation.
- Drafting, writing or revising the manuscript
- Agreeing on the final version of the manuscript and the journal which it will be submitted
- Taking responsibility and accountability of the content of the article

Outside the above mentioned authorship criteria, any other form of specific contribution should be stated in the Acknowledgement section.

In addition to being accountable for the parts of the work he/she has done, an author should be able to identify which co-authors are responsible for specific other parts of the work. In addition, authors should have confidence in the integrity of the contributions of their co-authors.

If an article is written by more than one person, one of the co-authors should be chosen as the corresponding author for handling all the correspondences regarding the article. Before submission, all authors should agree on the order of the authors and provide their current affiliations and contact details. Corresponding author is responsible for ensuring the correctness of these information.

Electrica requires corresponding authors to submit a signed and scanned version of the authorship contribution form (available for download through http://dergipark.gov.tr/iujeee) during the initial submission process in order to act appropriately on authorship rights and to prevent ghost or honorary authorship. If the editorial board suspects a case of "gift authorship," the submission will be rejected without further review. As part of the submission of the manuscript, the corresponding author should also send a short statement declaring that he/she accepts to undertake all the responsibility for authorship during the submission and review stages of the manuscript.

Electrica requires and encourages the authors and the individuals involved in the evaluation process of submitted manuscripts to disclose any existing or potential conflicts of interests, including financial, consultant, and institutional, that might lead to potential bias or a conflict of interest. Any financial grants or other support received for a submitted study from individuals or institutions should be disclosed to the Editorial Board. Cases of a potential conflict of interest of the editors, authors, or reviewers are resolved by the journal's Editorial Board within the scope of COPE guidelines.

The Editorial Board of the journal handles all appeal and complaint cases within the scope of COPE guidelines. In such cases, authors should get in direct contact with the editorial office regarding their appeals and complaints. When needed, an ombudsperson may be assigned to resolve cases that cannot be resolved internally. The Editor in Chief is the final authority in the decision-making process for all appeals and complaints.

When submitting a manuscript to Electrica authors accept to assign the copyright of their manuscript to İstanbul University-Cerrahpaşa Faculty of Engineering. If rejected for publication, the copyright of the manuscript will be assigned back to the authors. Electrica requires each submission to be accompanied by a Copyright Transfer Form (available for download at http://dergipark.gov.tr/iujeee). When using previously published content, including figures, tables, or any other material in both print and electronic formats, authors must obtain permission from the copyright holder. Legal, financial and criminal liabilities in this regard belong to the author(s).

Statements or opinions expressed in the manuscripts published in Electrica reflect the views of the author(s) and not the opinions of the editors, the editorial board, or the publisher; the editors, the editorial board, and the publisher disclaim any responsibility or liability for such materials. The final responsibility in regard to the published content rests with the authors.

MANUSCRIPT PREPARATION

Manuscripts can only be submitted through the journal's online manuscript submission and evaluation system, available at http://dergipark.gov.tr/iujeee. Manuscripts submitted via any other medium will not be evaluated.

Manuscripts submitted to the journal will first go through a technical evaluation process where the editorial office staff will ensure that the manuscript has been prepared and submitted in accordance with the journal's guidelines. Submissions that do not conform to the journal's guidelines will be returned to the submitting author with technical correction requests.

Authors are required to submit the following:

- Copyright Transfer Form,
- Author Contributions Form, and

during the initial submission. These forms are available for download at http://dergipark.gov.tr/iujeee.

Preparation of the Manuscript
Title page: A separate title page should be submitted with all submissions and this page should include:

- The full title of the manuscript as well as a short title (running head) of no more than 50 characters,
- Name(s), affiliations highest academic degree(s) and ORCID iD's of the author(s),
- Grant information and detailed information on the other sources of support,
- Name, address, telephone (including the mobile phone number) and fax numbers, and email address of the corresponding author,
- Acknowledgment of the individuals who contributed to the preparation of the manuscript but who do not fulfill the authorship criteria.

Biography page: A separate page should be submitted providing short biographies of the contributing authors with their photographs included.

Abstract: An abstract should be submitted with all submissions except for Letters to the Editor. The abstract of articles should be structured without subheadings. Please check Table 1 below for word count specifications.

Keywords: Each submission must be accompanied by a minimum of three to a maximum of six keywords for subject indexing at the end of the abstract. The keywords should be listed in full without abbreviations.

Manuscript Types
Original Articles: This is the most important type of article since it provides new information based on original research. The main text of original articles should be begun with an Introduction section and finalized with a Conclusion section. The remaining parts can be named relevantly to the essence of the research. Please check Table 1 for the limitations for Original Articles.

Review Articles: Reviews prepared by authors who have extensive knowledge on a particular field and whose scientific background has been translated into a high volume of publications with a high citation potential are welcomed. These authors may even be invited by the journal. Reviews should describe, discuss, and evaluate the current level of knowledge of a topic in the field and should guide future studies. sections Please check Table 1 for the limitations for Review Articles.

Letters to the Editor: This type of manuscript discusses important parts, overlooked aspects, or lacking parts of a previously published article. Articles on subjects within the scope of the journal that might attract the readers' attention, may also be submitted in the form of a "Letter to the Editor." Readers can also present their comments on the published manuscripts in the form of a "Letter to the Editor." Abstract, Keywords, and Tables, Figures, Images, and other media should not be included. The text should be unstructured. The manuscript that is being commented on must be properly cited within this manuscript.

Table 1. Limitations for each manuscript type

Type of manuscript	Word limit	Abstract word limit	Reference limit	Table limit	Figure limit
Original Article	3500	250 (Structured)	30	6	7 or total of 15 images
Review Article	5000	250	50	6	10 or total of 20 images
Letter to the Editor	500	No abstract	5	No tables	No media

Tables
Tables should be included in the main document, presented after the reference list, and they should be numbered consecutively in the order they are referred to within the main text. A descriptive title must be placed above the tables. Abbreviations used in the tables should be defined below the tables by footnotes (even if they are defined within the main text). Tables should be created using the "insert table" command of the word processing software and they should be arranged clearly to provide easy reading. Data presented in the tables should not be a repetition of the data presented within the main text but should be supporting the main text.

Figures and Figure Legends
Figures, graphics, and photographs should be submitted as separate files (in TIFF or JPEG format) through the submission system. The files should not be embedded in a Word document or the main document. When there are figure subunits, the subunits should not be merged to form a single image. Each subunit should be submitted separately through the submission system. Images should not be labeled (a, b, c, etc.) to indicate figure subunits. Thick and thin arrows, arrowheads, stars, asterisks, and similar marks can be used on the images to support figure legends. Like the rest of the submission, the figures too should be blind. Any information within the images that may indicate an individual or institution should be blinded. The minimum resolution of each submitted figure should be 300 DPI. To prevent delays in the evaluation process, all submitted figures should be clear in resolution and large in size (minimum dimensions: 100 × 100 mm). Figure legends should be listed at the end of the main document.

Equations
The equations must be stated separated from the text by a blank line. They should be numbered consecutively in parenthesis at the right side of the equation. Symbols and variables as well as in the main text should be written in italics while vectors and matrices should be written in bold type.

All acronyms and abbreviations used in the manuscript should be defined at first use, both in the abstract and in the main text. The abbreviation should be provided in parentheses following the definition.

When a product, hardware, or software program is mentioned within the main text, product information, including the name of the product, the producer of the product, and city and the country of the company (including the state if in USA), should be provided in parentheses in the following format: "Discovery St PET/CT scanner (General Electric, Milwaukee, WI, USA)"

All references, tables, and figures should be referred to within the main text, and they should be numbered consecutively in the order they are referred to within the main text.

References

While citing publications, preference should be given to the latest, most up-to-date publications. If an ahead-of-print publication is cited, the DOI number should be provided. Authors are responsible for the accuracy of references. In the main text of the manuscript, references should be cited using Arabic numbers in square brackets. The reference styles for different types of publications are presented in the following examples.

Journal Article: J.K. Author, "Name of the article", Abbrev. Title of Periodical, vol. x, no. x, pp. xxx-xxx, Abbrev. Month, year.

Book Section: J. K. Author, "Title of chapter in the book," in Title of His Published Book, xth ed. City of Publisher, Country: Abbrev. of Publisher, year, ch. x, sec. x, pp. xxx–xxx.

Books with a Single Author: J.K. Author, "Title of the Book", Abbrev. Of Publisher, City of Publisher, Country, Year.

Conference Proceedings: J. K. Author, "Title of paper," in Unabbreviated Name of Conf., City of Conf., Abbrev. St ate (if given), year, pp. xxx-xxx.

Report: J. K. Author, "Title of report," Abbrev. Name of Co., City of Co., Abbrev. State, Rep. xxx, year.

Thesis: J. K. Author, "Title of thesis," M.S. thesis, Abbrev. Dept., Abbrev. Univ., City of Univ., Abbrev. State, year.

Standards: Title of Standard, Standard number, date.

Manuscripts Accepted for Publication, Not Published Yet: J. K. Author, "Title of paper," unpublished.

Manuscripts Published in Electronic Format: J. K. Au thor. (year, month). Title. Journal [Ty pe of medium]. volume(issue), pag ing i f g iven. A vailable: site/path/file

REVISIONS

When submitting a revised version of a paper, the author must submit a detailed "Response to the reviewers" that states point by point how each issue raised by the reviewers has been covered and where it can be found (each reviewer's comment, followed by the author's reply and line numbers where the changes have been made) as well as an annotated copy of the main document. Revised manuscripts must be submitted within 30 days from the date of the decision letter. If the revised version of the manuscript is not submitted within the allocated time, the revision option may be cancelled. If the submitting author(s) believe that additional time is required, they should request this extension before the initial 30-day period is over.

Accepted manuscripts are copy-edited for grammar, punctuation, and format. Once the publication process of a manuscript is completed, it is published online on the journal's webpage as an ahead-of-print publication before it is included in its scheduled issue. A PDF proof of the accepted manuscript is sent to the corresponding author and their publication approval is requested within 2 days of their receipt of the proof.

Editor in Chief : Sıddık YARMAN
Address : İstanbul Üniversitesi-Cerrahpaşa Mühendislik Fakültesi Elektrik-Elektronik Mühendisliği Bölüm Başkanlığı Avcılar Kampüsü, Avcılar, İstanbul, Turkey
Phone : +90 212 4737070
Fax : +90 212 4737064
E-mail : sbyarman@gmail.com

Publisher : AVES
Address : Büyükdere Cad. 105/9 34394 Mecidiyeköy, Şişli, İstanbul, Turkey
Phone : +90 212 217 17 00
Fax : +90 212 217 22 92
E-mail : info@avesyayincilik.com
www.avesyayincilik.com

Contents

İSTANBUL UNIVERSITY
CERRAHPAŞA

RESEARCH ARTICLE
Electrica 2019; 19(1): 1-11

The Design and Implementation of a Batteryless Wireless Embedded System for IoT Applications

Mehmet Erkan Yüksel

Department of Computer Engineering, Mehmet Akif Ersoy University, Burdur, Turkey

Cite this article as: Yüksel ME. Design and Implementation of A Batteryless Wireless Embedded System for IoT Applications. *Electrica*, 2019; 19(1): 1-11.

ABSTRACT

With the increasing popularity of embedded systems that consist of identifying, sensing, processing, and communication capabilities, the Internet of Things (IoT) has enabled many new application scenarios in diverse scientific fields and provided a significant opportunity to build efficient industrial systems and applications. Most embedded systems consume power provided by fixed batteries with limited capacity. However, the main disadvantage of batteries is that they must be periodically replaced with new ones or recharged when they are depleted. This kind of maintenance process increases the cost and restricts the use in inaccessible places. When considering the limitations of battery power, alternative energy sources are required for interconnected devices to operate efficiently and effectively. Harvesting or scavenging energy from the environment is an important strategy to design self-powered systems employed in the IoT domain. Traditional energy harvesting applications use large energy storage devices to supply the power to the system whenever needed. Batteryless energy harvesting techniques have advantages to operate long periods without maintenance. In this study, we designed and implemented a supercapacitor-based, solar-powered wireless embedded system that can operate autonomously without the need of maintenance and battery replacement. Our goal is to explore and analyze the applicability of batteryless wireless data communication and the usefulness of self-powered smart devices employing an energy harvesting technique in the IoT environment. In our experiments, we observed that our prototype boards operate well with low-power consumption without any performance degradation.
Keywords: IoT, wireless communication, embedded systems, solar energy, energy harvesting, supercapacitor

Introduction

Internet of Things (IoT) is a rapidly developing technology that has a wide range of application domains, technological innovations, and social impacts. It is a dynamic global network infrastructure consisting of interconnected devices with identification, sensing, data processing, information exchange, and communication capabilities. It provides an intelligent ecosystem for the information society by enabling advanced services, standards, and platforms.

With recent advances in wireless communications, digital electronics, integrated circuits (IC), sensors, and micro-electro-mechanical systems (MEMS) technology, the design and development of low-cost, low-power, multifunctional and autonomous wireless smart devices have become important.The ever-increasing capabilities of these devices enable the realization of various IoT applications based on the collaborative effort of a large number of smart devices [1-3].

The general architecture and basic components of a wireless smart device are shown in Figure 1. It can be an embedded system or a single-board computer to perform multiple tasks. It typically consists of a sensing unit to sense changes in its surroundings; a communication unit to interact with other devices or the Internet to take an active role in the decision-making process; a computing unit to process information; and a power source. Moreover, several components such as an actuator, an external memory, a location finding system, and a power generator can also be integrated into the device depending on the IoT application.

Sophisticated hardware and software features place additional challenges on the operation of wireless smart devices. Wireless smart devices are battery dependent, and power con-

Corresponding Author:
Mehmet Erkan Yüksel

E-mail:
erkanyuksel@mehmetakif.edu.tr

Received: 03.05.2018

Accepted: 30.07.2018

DOI: 10.26650/electrica.2018.28092

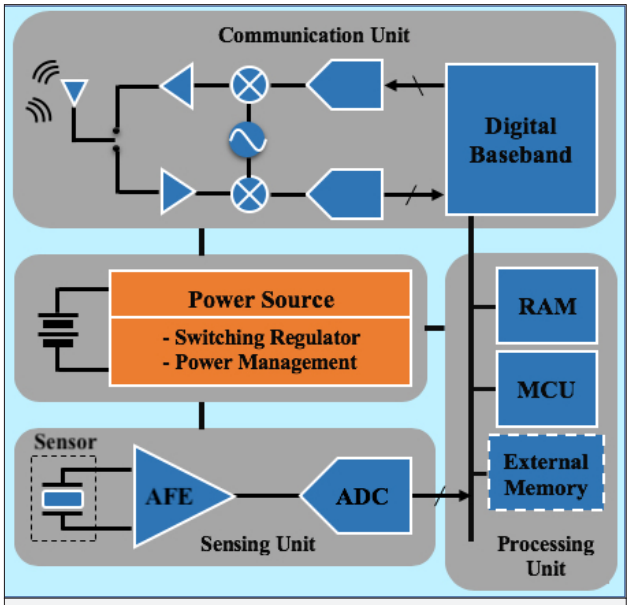

Figure 1. Hardware components of an embedded system

sumption is one of the main factors which significantly influence their design. For most IoT applications (i.e., smart home, remote monitoring and control systems, smart city), these devices must operate autonomously and unattended, and must be adaptive to the environment. It may not be feasible to replace or recharge their batteries. With the limited battery power, the operational lifetime of these devices is also limited. Therefore, power is a scarce and vital resource in the IoT ecosystem. It is possible to extend the operational lifetime of wireless smart devices through energy harvesting techniques. Solar cells provide practical and cost-effective solutions for energy-efficient operations. However, the amount of energy that can be extracted is still limited. Consequently, since wireless smart devices are required to perform their tasks efficiently for long periods of time, harvesting or scavenging energy from the environment is an important strategy to design and develop self-powered systems [4, 5].

Related Work

Autonomous embedded systems with low-power consumption have recently received great attention in the literature due to their applications in many emerging technologies such as home automation, smart cities, smart manufacturing, healthcare, wearables, automotive, precision agriculture, supply chain management, and industrial internet. These applications employ a network infrastructure with limited power sources and need to incorporate various energy harvesting systems for their continuous operations.

Various self-sustaining power supplies for wireless embedded systems have been introduced in the past. In [6], the authors presented a solar-harvesting, energy-wise upgradeable platform for environmental sensor networks. The device contains a solar panel as its power source and rechargeable NiMH batteries as its energy storage element. Its design features are simple hardware structure and cheap energy storage units. The authors study the charging and discharging characteristics of the power supplies. In [7], the authors presented the design, implementation, and performance evaluation of a plug-and-play solar energy harvesting module that powers the Berkeley/Crossbow sensor motes. The module has a solar energy harvesting circuit and a rechargeable battery. It autonomously manages all decisions related to energy harvesting, energy storage, and power routing. It enables harvesting-aware operation by providing instantaneous solar and battery-state information. In [8], the authors designed a platform to build outdoor sensor networks for environmental monitoring and agriculture applications. The platform is equipped with the Nordic nRF905 RF transceiver, two rechargeable NiMH batteries as the primary power source, a solar panel, an on-board battery charging circuit and regulator, a real-time clock, a flash memory, and a temperature sensor. It is capable of monitoring battery voltage, battery current, charging voltage, and charging current. The power input stage of the platform provides the ability to compute both the energy coming in and the energy being consumed. This enables the implementation of distributed energy-aware applications. In [9], the authors proposed a technique consisting of a power distribution switch (to route power sources to subsystems) and a power source-power consumption matching algorithm (to maximize the total utility of the available power from the ambient power sources). The system is composed of sensors that detect the ambient energy intensity, the controller that runs an algorithm to maximize the utilization of power sources, and the switch array that establishes the connections between power sources and subsystems. The higher utility of ambient power is obtained by combining the maximum power point tracking (MPPT) and the power defragmentation. Moreover, the microcontroller control based on the light sensors is also required. In [10], the authors designed a wireless sensor node to show the feasibility of energy harvesting for sub-watt, small-scale systems integrated with durable energy storage in the form of supercapacitors. They proposed a feed-forward, pulse frequency modulated regulator that charges supercapacitors at near-optimal operating points for solar cells. The device stores energy obtained from solar cells in supercapacitors. It employs an MPPT circuit that enables solar cells to efficiently charge supercapacitors (to maximize the amount of available energy). However, the MPPT circuit requires a microcontroller to run the MPPT algorithm. In [11], the authors developed a system that manages energy transfer for perpetual operation (to maximize the lifetime of the sensor device). Their platform uses a solar panel, a charging circuit, and a two-stage storage unit consisting of supercapacitors (a primary buffer charged by a solar panel to power the device) and a Li+ rechargeable battery (a secondary buffer as a reliable emergency backup. It is charged either by solar panel or by the primary buffer).

System Design and Implementation

In our study, we developed a supercapacitor-operated, solar-powered, autonomous wireless embedded system for IoT

applications. The hardware architecture of our system is depicted in Figure 2.

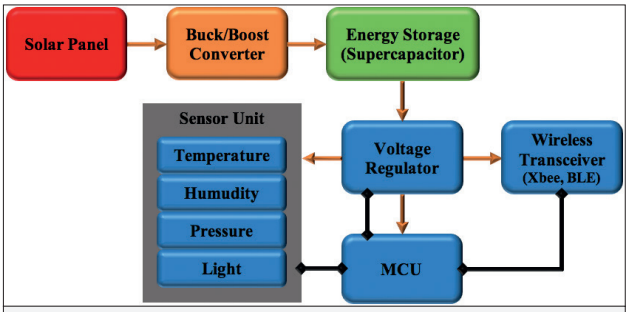

Figure 2. Embedded system architecture

The system is designed for three main tasks: using a solar panel as a power source, charging the supercapacitor through a switching regulator, and performing energy management for all typical sensor and wireless communication functions.

In order to obtain the maximum power from the solar panel (6V 150mA), a buck/boost converter is used. A supercapacitor is chosen instead of a rechargeable battery to store harvested energy. Because, a supercapacitor has infinite charging cycles, and its charging/discharging efficiency is higher than that of a battery. When the available energy in the supercapacitor is insufficient to operate the converter, the initial energy harvesting process is passive. Once enough energy is stored for the reliable startup of the converter, the system transitions to an operational state where it actively manages the energy harvesting and controls the power availability to the embedded device. If the energy stored in the supercapacitor is enough to supply power to the embedded device, then the system enables the device to operate with regulated voltage, while continuing to harvest energy from the solar panel Finally, a microcontroller (Atmega328P) is employed to perform several tasks, such as processing sensor data, energy management, and communication.

Our embedded device provides information about its surrounding environment to a host system through its XBee or BLE module (i.e., BLE supported devices such as smartphones can obtain information from the device). In addition, the application running on the device uses an energy management software to optimize the energy efficiency (or usage). Consequently, all components of our device interact with each other, and therefore, each component influences the energy transfer between them, as well as the power consumption and behavior of the complete system.

Figure 3 shows the implementation of our batteryless wireless embedded system and prototype devices. All of the devices operate autonomously when the solar panel and supercapacitor are integrated with the devices.

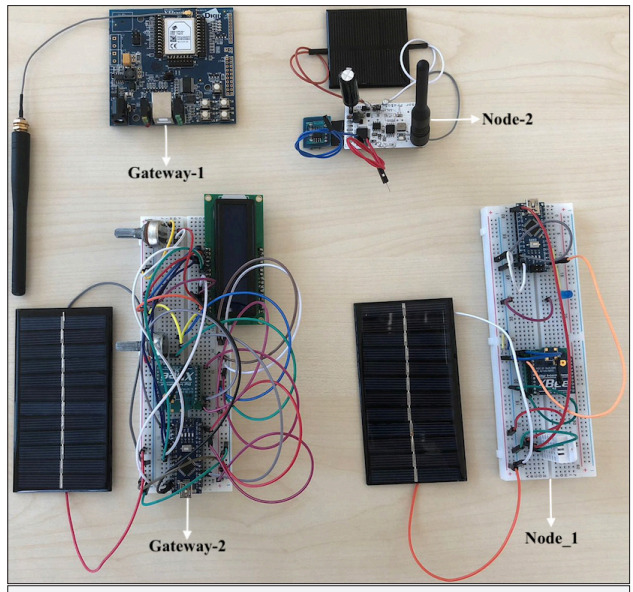

Figure 3. Our prototype boards and development tools

Power source

Solar is an important energy source for autonomous embedded systems, usually due to the following factors:

- Solar energy is clean, sustainable, renewable, and inexhaustible. It is readily available anywhere.
- Solar cells can produce electricity from available light even under low-irradiance conditions (i.e., indoor environments) [12]. They provide high power density compared to other power sources such as acoustic noise, thermal, radio frequency, vibrations, airflow.
- Photovoltaic (PV) systems have advantages such as easy implementation, high reliability, silent operation, long life, low maintenance cost, and employing simple equipments with no moving or rotating parts [12, 13].
- Many embedded systems use solar cells in recent years, because solar energy provides sufficient power for most of today's smart electronic devices that consume up to several hundred mW of power [2, 8, 12-17].

Solar cells generate electricity from sunlight. They are connected together in either series or parallel combinations or both to form a solar module/panel which provides higher output voltages and currents. If solar cells are connected in series the voltage increases. If they are connected in parallel, then the current increases (Figure 4). An energy harvesting circuit fixes the output power of the solar cell and transfers this power to the energy storage unit. It performs avoiding the backflow from the energy storage unit to the solar cell, protecting the energy storage unit from overload, fixing the operating point for the solar cell [13]. The amount of power generated by the solar cell depends on solar irradiation, the physical and chemical char-

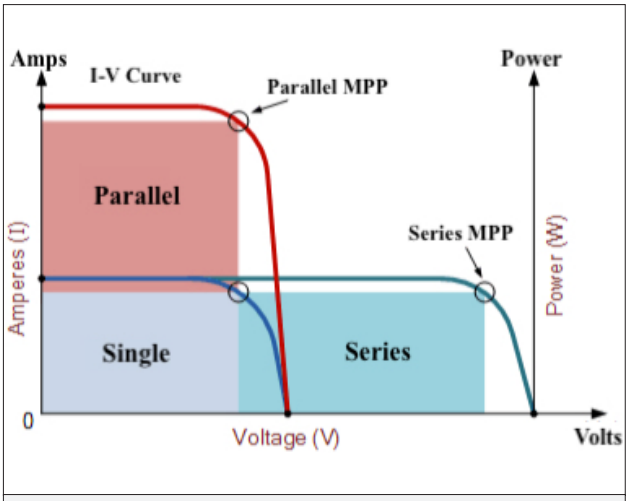

Figure 4. I-V characteristics curve of connected solar cells [18]

acteristics of the solar cell, the operating point of the solar cell, and weather conditions [13].

To understand the behavior of a solar cell, we model the solar cell by using an equivalent circuit shown in Figure 5.

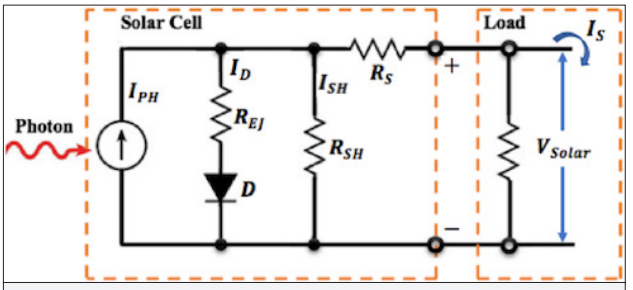

Figure 5. Equivalent circuit of a solar cell

I_{PH}: photogenerated current I_S: solar current

I_D: diode current R_{SH}: shunt resistance

I_{sH}: shunt current R_S: series resistance

R_{EJ}: equivalent junction resistance

Solar cells produce a current, I_{PH}, depending on the incident photons. For instance, considering the n parallel-connected solar cells, I_{PH} is:

$$I_{PH} = n \cdot I_{SC} \tag{1}$$

I_{SC} : short-circuit current

The exact value of the I_{SC} depends on the operational condition of the solar cell (i.e., cell temperature, solar irradiation, physical and chemical properties of the pn-junction). In addition, the performance of a solar cell can be characterized by its open-circuit voltage (V_{OC}).

$$V_{OC} \approx \frac{\eta kT}{q} ln\left(\frac{I_{PH}}{I_0} + 1\right) \quad , * \{I_{PH} \approx I_{SC}\} \tag{2}$$

* for a quality solar cell (high R_{SH}, low R_S and I_O)

As shown in Figure 6, the I-V characteristic curve defines the current and voltage characteristics of a specific solar cell by providing a detailed information about the solar energy conversion ability and efficiency. The I-V characteristics of a solar cell (particularly P_{max}) is crucial to analyze the performance and solar efficiency of the embedded system.

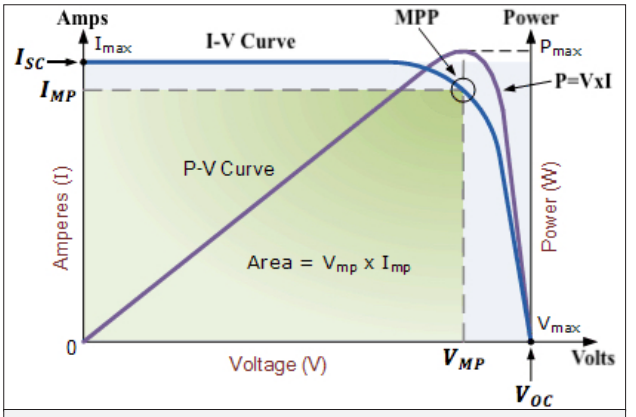

Figure 6. -V characteristics curve of a solar cell [18]

• The current produced by the solar cell:

$$I_S = I_{PH} - I_D - I_{SH} \tag{3}$$

• The output voltage of the solar cell:

$$V_{Solar} = V_{OT} + I_S \cdot R_S \tag{4}$$

V_{OT}: voltage across the output terminals

• The diode current:

$$I_D = I_0 \left(exp\left[\frac{V_{Solar}}{\eta \cdot V_T}\right] - 1\right) \tag{5}$$

V_T=kT/q, thermal voltage (≈ 0.0259V at 25˚)

I_O: reverse saturation current

n: diode ideality factor

q: electron charge constant

k: Boltzmann constant

T: absolute temperature

• The characteristic equation of the solar cell:

$$I_S = I_{PH} - I_0\left(exp\left[\frac{V_{Solar}}{\eta \cdot V_T}\right] - 1\right) - \frac{V_{Solar}}{R_{SH}} \quad (6)$$

*The generated power through the solar cell:

$$P_{Solar} = V_{Solar} \cdot I_S \quad (7)$$

The I-V characteristics of solar cells are non-linear and non-monotonic. Depending on each solar irradiance level, the power reaches a global maximum at a certain voltage (or current), which is the optimal operating point (Maximum Power Point-MPP) to obtain the maximum amount of power from the solar cell (Figure 7).

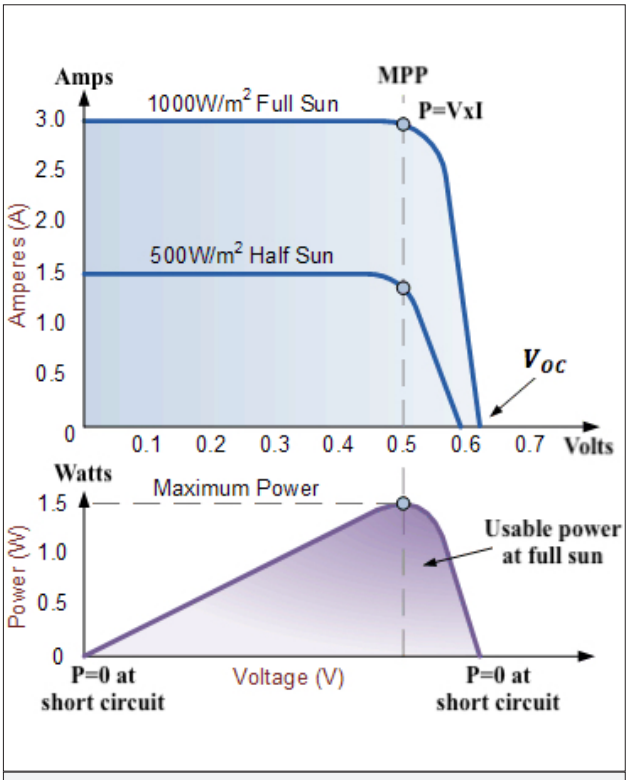

Figure 7. I-V characteristics curve in response to sunlight [18]

The MPP is calculated by the equations below:

$$\frac{dP_{Solar}}{dV_{Solar}} = \frac{dP_{Solar}}{dI_{Solar}} = 0 \quad (8)$$

$$\frac{I_{PH}+I_0}{I_0} = \left(\frac{q \cdot V_{MPP}}{\eta kT} + 1\right) \cdot exp\left(\frac{q \cdot V_{MPP}}{\eta kT}\right) \quad (9)$$

As can be seen from Eq. 9, the MPP can be referred to as a function of I_{PH} and I_O, which depends on the solar irradiance and temperature. V_{MPP} represents the output voltage of the solar cell when the solar cell is operating at the MPP. Eq. 9 can provide a basis for MPP tracking (MPPT). However, the implementation of MPPT in energy harvesting systems is a challenging task because of the need to measure the voltage and current levels of solar cells, temperature, and solar irradiance. Therefore, several MPPT techniques have been proposed in the literature to obtain more accurate results [19-22]. The power generated by a solar panel at a W_{SI} solar irradiance is given below:

$$P_{Solar} = min\left(P_R \cdot \frac{W_{SI}}{W_R}, P_{Solar}^{mAx}\right) \quad (10)$$

P_R: rated power output of the solar cell

W_R: rated irradiance level

Energy storage

It is crucial to choose a well-suited storage device for embedded systems. Many of today's embedded systems use batteries as energy storage. However, batteries are often stated as a major limiting factor that influences the operational lifetime of embedded systems. Batteries have a high energy density; however, they have limited power density (charge-discharge rates). In addition, continuous high rate cycling, inability to hold a full charge for a long time, and harsh environmental conditions (i.e., temperature) adversely affect both battery performance and lifetime. These negative effects lead to periodic maintenance and battery replacement for embedded systems. Unfortunately, such recurring maintenance and replacement can be very expensive if they must be done for many devices, which are likely to be time-consuming, expensive, and difficult to access after deployment. Consequently, the battery is a crucial factor which prevents the embedded systems from operating maintenance-free for more than several years at different data rates [23].

One solution which provides the long-term operation of embedded systems without the need of a battery is to use a supercapacitor. The viable technique is to remove the battery altogether, replace it with the supercapacitor and store energy in it. Supercapacitors are a good choice for embedded systems due to their operational features, particularly the high power density. They have high charge-discharge efficiency, unlimited charging cycles, wide operating temperature range, and long lifetime (Table 1). They do not release any thermal heat during

Table 1. Comparison of supercapacitors and batteries

Property	Supercapacitors	Batteries
Energy density	Low	High
Power density	High	Low
Voltage behavior	Varying	Constant
Cycle life	High	Low
Temperature peformance	Good	Poor
DC life	High	Medium
Form factor	Small	Large
Weight	Light	Heavy

the discharging process. They are also known as a green technology because of the high efficiency and the materials used in production. These outstanding features make supercapacitors a useful energy storage device for embedded systems employed in IoT [24-28].

Supercapacitors have advantages in terms of energy storage. A general idea about the performance of these devices in comparison with normal capacitors and batteries can be obtained by examining their situations on the Ragone plot shown in Figure 8. The Ragone plot describes the relationship between the energy density and power density of various energy storage/energy propulsion technologies. Thus, it is feasible to analyze the device's ability to store energy for long periods (high energy density) against its ability to obtain a large amount of energy in a short time when required (high power density). As shown in Figure 8, supercapacitors are located between capacitors and batteries, depending on their characteristic features. They have higher power density than batteries and higher energy density than normal capacitors. They are not exposed to chemical reactions; therefore, they have a much higher number of charge cycles.

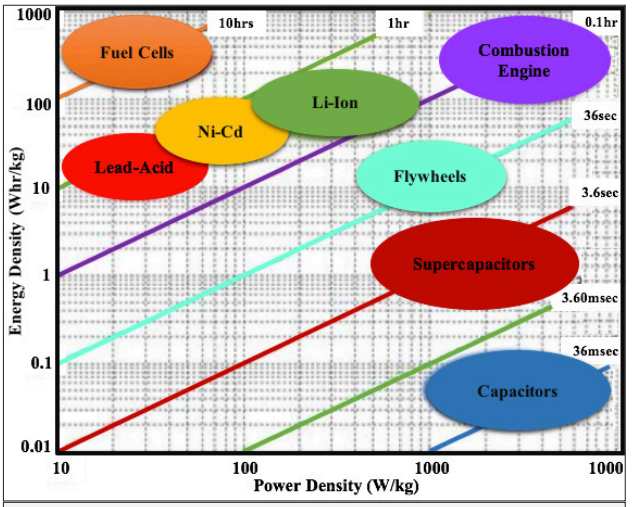

Figure 8. Performane comparison of energy storage devices

Energy harvesting

As shown in Figure 9, our energy harvesting system uses a DC/DC switching regulator that has a wide range of input and output voltages, and high conversion efficiency over the embedded device's operating power range. The regulator is placed between the solar cell and supercapacitor to increase the harvesting efficiency. It prevents the supercapacitor from degrading the operation performance of the solar cell. Such a structure enables energy harvesting to continue even when $V_{OC}<V_{SCOP}$. The regulator also serves as a diode to block reverse current flow from supercapacitor to the solar cell [29].

Wireless embedded systems operate at a constant input voltage. Therefore, the energy storage device rarely has the same voltage. A boost (step-up) converter is employed to increase the input voltage. In the case of a higher storage voltage, a buck (step-down) converter is more efficient. Our choice is to use a buck/boost DC/DC converter that enables up-down voltage conversion to operate the embedded system independent of the supercapacitor voltage efficiently. The reg-

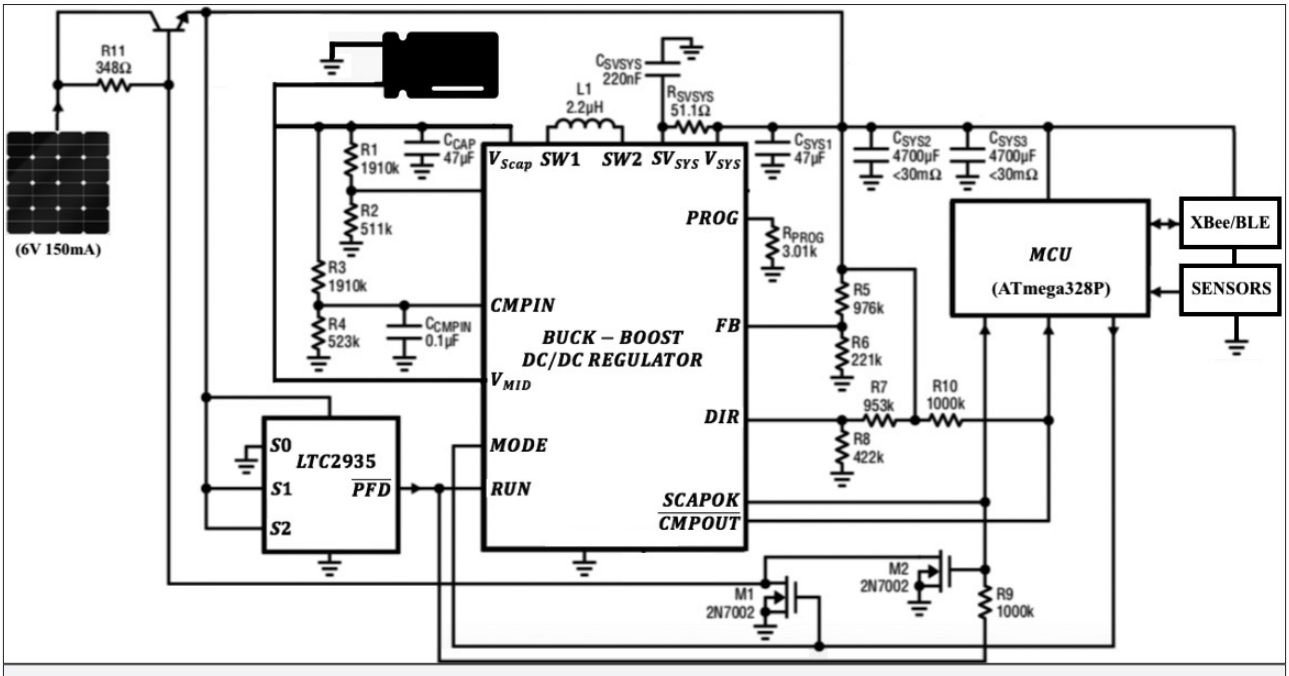

Figure 9. Implementation of the energy harvesting system

ulator is set to operate at the lowest possible voltage level to improve the energy efficiency of the embedded system. In addition, the operating voltage is adjusted by an energy management software using dynamic power management technique to reduce system power consumption without degrading performance. Finally, a secondary switching regulator is employed to operate MCU, wireless transceiver, and sensors, which require different voltage than the embedded system's voltage [27-29].

Energy harvesting method

Power management techniques designed for the energy-efficient operation of embedded systems differ significantly when the power source changes from a battery to an energy harvesting module. One of the reasons which leads to differences is that the ambient energy source is highly variable. Contrary to the stored energy characterized by the amount of the battery's residual energy, ambient energy requires a more sophisticated characterization. Another reason is that ambient energy is not a scarce resource and has the potential to be used forever for the sustainable performance of the embedded systems.

Since the ambient energy source varies a great deal, the main design goal is to increase the overall system performance. Another goal is to determine whether ambient energy is enough for the embedded system to perform its tasks at the desired performance level. If so, the system operates efficiently and effectively. If not, energy harvesting requirements must be specified for the system. Consequently, the aim of developing an energy harvesting technique is to enable an analysis of various energy harvesting technologies with respect to system performance [28-30].

To obtain better results on the performance and lifetime of wireless embedded systems operating from an available energy source, it is necessary to specify the important features/parameters of the energy availability. This situation requires modeling the energy provided by a harvesting system that converts ambient energy into electrical energy and stores it in a supercapacitor. We can make use of a model proposed in [27] to characterize the production and consumption of ambient energy for our prototype board, which employs an energy harvesting system shown in Figure 10.

• The power output of the energy source:

$$E_{Source}(P, e_1, e_2): \begin{matrix} \int_T E_S(t)\,dt \geq PT - e_1 \\ \int_T E_S(t)\,dt \leq PT + e_2 \end{matrix} \quad (11)$$

• The power consumption of the energy consumer:

$$E_{Consumer}(P', e): \int_T E_C(t)\,dt \leq P'T + e \quad (12)$$

In the above definitions, $E_s(P, e_1, e_2)$ denotes the energy source (solar panel), which supplies power to our embedded system. $E_s(t)$ models the power output of the energy source at time t. $E_c(P',e)$ denotes the energy consumer (embedded system), which obtains power from the energy source. $E_c(t)$ models the power consumption of the embedded system at time t. P and P' are the available powers at which the system can operate. The variables (e, e_1, e_2) denote the energy storage capacity of the embedded system.

Figure 10 shows the general architecture of our energy harvesting system, which describes the energy flow in our prototype board. The solar panel produces a current, $I_{Solar} \geq 0$, depending on ambient conditions. The switching regulator (with capacitor charger and balancer features) converts the input voltage to an

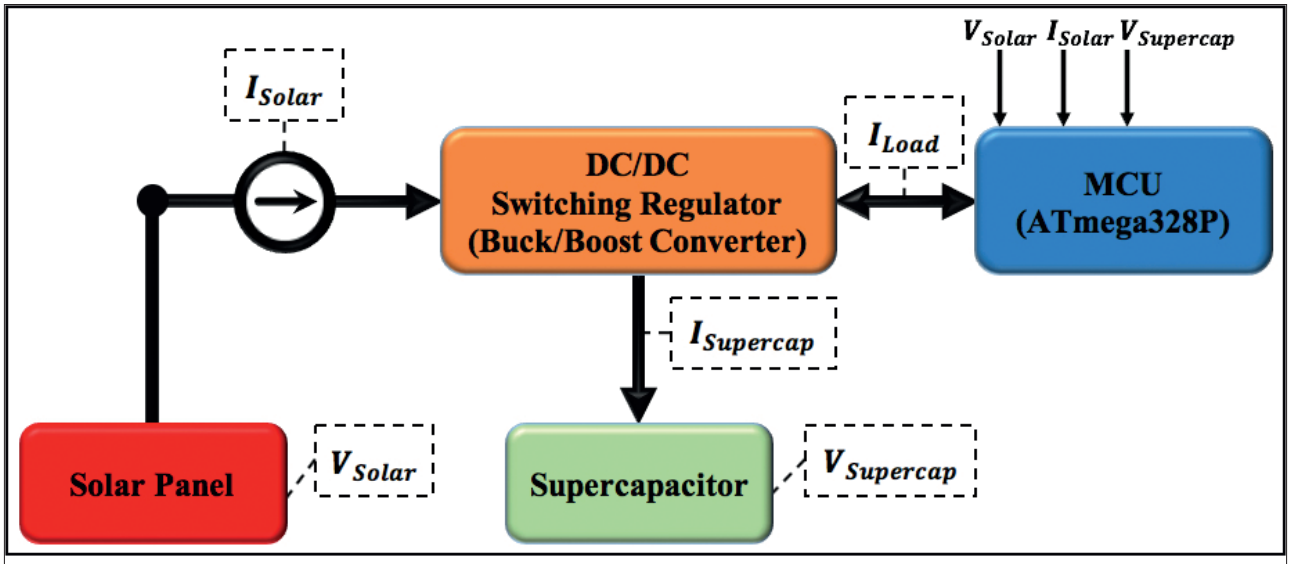

Figure 10. Block diagram of our energy harvesting system

output voltage with high efficiency (Figure 11). The regulator current, I_{Reg}>0, is consumed by the regulator to supply the embedded system with the current I_{Load}>0 at the output voltage V_{Load}. The supercapacitor serves as energy storage. The current I_{Scap} flows into the supercapacitor with a capacity of *C*. If I_{Scap}>0, the supercapacitor is charged; otherwise, it acts as a power source and discharges to supply the system. The supercapacitor voltage, V_{Scap}, cannot exceed V_{max} because of overcharging protection. If V_{Scap} underruns the cut-off voltage V_{cutoff}, then the regulator fails. Finally, the power-conversion efficiency of the regulator,*n*, is a function of I_{Load} and V_{Scap}.

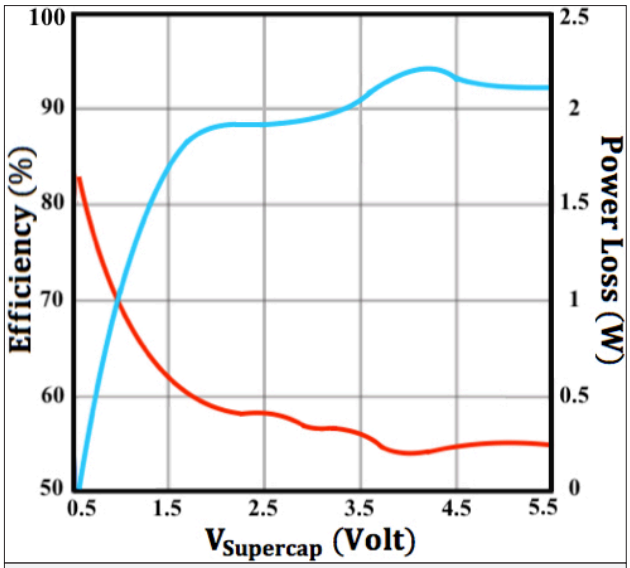

Figure 11. Charge efficiency of the switching regulator

Based on the information mentioned above, we can model the energy flow for our embedded system as follows:

$$I_{Solar} = I_{Reg} + I_{Scap} \quad (13)$$

$$I_{Reg} = \frac{V_{Load} \cdot I_{Load}}{V_{Scap} \cdot \eta \cdot (V_{Scap}, I_{Load})} \ , \ I_{Scap} = C \cdot V_{Scap} \quad (14)$$

The embedded system influences the overall system power consumption by changing its duty cycle. We can model it as a power sink of periodic pulses. In most cases, we only model the average power consumption by assuming the wake time is negligible:

$$P_{avg}^{d} = V_{sup} \cdot \left(d \cdot I_{act} + (1 - d) \cdot I_{slp}\right) \quad (15)$$

where

P_{avg}^{d}: average power consumption

V_{Sup}: supply voltage *d*: duty cycle,

I_{act}: active mode current

I_{stp}: sleep mode current

Results and Discussion

For autonomous wireless embedded systems with limited battery power employed in IoT, continuous power availability and low maintenance cost are crucial. Energy harvesting technologies and batteryless systems have the advantage of being able to operate for long periods of time in IoT applications where the battery replacement is difficult/unsuitable. In addition, wireless technologies such as Zigbee, XBee, LoRa, and BLE have become prominent low-power wireless solutions for both embedded systems and IoT. In order to perform tasks for long periods of time, two approaches can be considered. One is to increase the battery capacity. The other is to reduce system power consumption. The first method increases cost and battery size. It also requires maintenance and battery replacement. To make the system more efficient as well as to reduce the cost and maintenance, it is important to produce low-power types of equipment. There is also one more approach in which batteries are not used. In this method, we have proposed an energy harvesting system consisting of a solar panel, a supercapacitor, a switching regulator, and an energy management software.

In our study, we analyzed how well will wireless technologies, most particularly BLE and XBee, function when employed in a batteryless embedded system that runs on harvested energy and low-power consumption. The generated power is in proportion to the size of the energy harvesting module. In addition, most harvesting systems include energy storage devices to store extra energy. This is used later to meet demand depending on the lack of power when the ambient energy source is temporarily unavailable (i.e., during nights). Energy storage devices can be batteries, supercapacitors, or their combinations. Consequently, our goal is to develop a solar-powered batteryless wireless embedded system considering the low-power consumption and small form factor. We designed a prototype board utilizing a solar panel to harvest energy, a buck/boost DC/DC converter to distribute power, and a supercapacitor to eliminate the battery requirement. Figure 12 shows the performance evaluation of our embedded device with the BLE module at different operation stages.

Since the energy harvester uses a DC voltage, an AC voltage

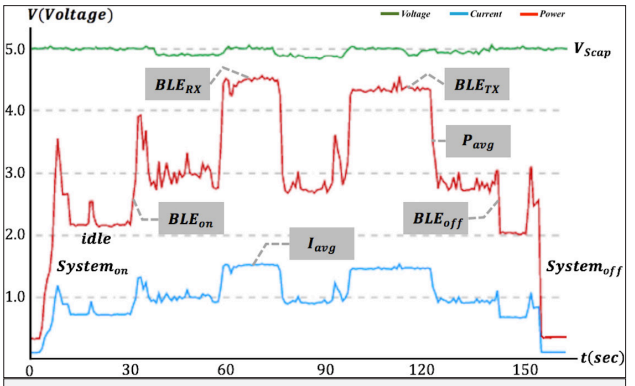

Figure 12. Performance evaluation of the prototype board

source needs a rectifier before the harvester use AC source. In addition, voltage ratings of the power source highly depend on environmental factors. When the voltage level exceeds the allowed harvester features, a voltage limiter is used before the power source is integrated with energy harvester. Our energy harvesting module employs a switching regulator, and its software executes a power monitoring function to obtain a sufficient amount of energy from the power source.

Wireless modules used in embedded systems consume a large amount of energy while sending and receiving data. Therefore, an optimization technique for the communication system has a crucial impact on the self-sustainability of embedded systems. Except for sending and receiving modes, we can remarkably reduce the power consumption by using the sleep mode that exists in most RF chips. To choose the right RF chip is important in order to obtain low power in the sleep mode for embedded systems.

The microcontroller is another component that consumes more power. It controls all peripheral devices on the board. The most influential part for the power consumption of the microcontroller is the operation clock. Speeding up of the clock increases power consumption. The clock control is a critical factor in reducing power consumption. It is important to select a microcontroller that consumes less power as much as possible in sleep mode and keeps it in sleep mode as long as possible. Another critical situation is the wake-up time from sleep mode. Until the crystal oscillator is stabilized, the microcontroller consumes power during the standby mode. Therefore, the short wake up time is essential to reduce power consumption.

Conclusion

IoT has become a paramount technology for the information society and led to a paradigm shift in many research areas. It provides us an intelligent ecosystem with infinite opportunities where smart interconnected devices communicate and interact with each other and the Internet. Since IoT and smart devices have attracted a great deal of attention in recent years, the design of energy-efficient embedded systems has become more important. Embedded systems must perform well in the IoT environment without the possibility of periodic maintenance. The replacement of these devices can be time-consuming very complex and expensive, even when the device itself is of low cost. In addition to achieving their primary goals, they must provide extra functionalities such as energy-efficient operation, self-diagnostics, self-powered, self-sustained, and network compatibility. Moreover, they need to be extremely secure, robust, and reliable. In order to fulfill all mentioned requirements, they need to possess a certain level of intelligence along with a small form factor.

Ambient energy harvesting provides a viable option to supplement the power supply of energy-constrained embedded systems employed in several IoT applications where the required operating lifetime is very long, maintenance and battery replacements are next to impossible. In this study, we analyzed how an energy harvesting aware power management can supply power to an embedded system, further improve the energy usage and system lifetime. We presented an architecture for the perpetual operation of a self-powered embedded system using the ambient energy source. We made use of a model that can be used to characterize the energy source and determine the sustainable performance of the embedded system. We designed and implemented a batteryless wireless prototype board that employs an energy harvesting module consisting of a solar panel, a supercapacitor, and a DC/DC switching regulator. The regulator facilitates energy transfer from the solar panel into the supercapacitor and charges the supercapacitor at near-optimal operating points for the solar panel. The harvesting module sufficiently supplies power to the board when there is not enough sunlight in the environment. We observed that our board efficiently harvests energy while performing sensing, processing, and communication tasks under different weather conditions. Our device is a low-cost solution and easy to use. It has low hardware complexity and low energy demand, which is easily fulfilled by the supercapacitor. Consequently, supercapacitor-operated solar powered embedded systems can be smaller and lighter, and they do not need to be oversized to accommodate high power cycling. They can be adaptable to IoT applications and robustly sustain the prolonged operation. They require less monitoring and less sophisticated management systems and ensure maintenance-free operation.

Peer-review: Externally peer-reviewed.

Conflict of Interest: The author have no conflicts of interest to declare.

Financial Disclosure: The author declared that the study has received no financial support.

References

1. P. Horowitz, W. Hill, "The art of electronics", Cambridge University Press, Cambridge, United Kingdom, 2015.
2. T. Wu, F. Wu, J. M. Redoute, M. R. Yuce, "An autonomous wireless body area network implementation towards IoT connected healthcare applications", IEEE Access, vol. 5, pp. 11413-11422, June, 2017. [CrossRef]
3. F. Wu, C. Rudiger, M. R. Yuce, "Real-time performance of a self-powered environmental IoT sensor network system", Sensors, vol. 17, no. 2, pp. 282-296, Feb, 2017. [CrossRef]
4. T. Wu, M. S. Arefin, J. M. Redoute, M. R. Yuce, "A solar energy harvester with an improved MPPT circuit for wearable IoT applications", in The International Conference on Body Area Networks, Turin, Italy, 2016, pp. 166-170.
5. D. Gunduz, K. Stamatiou, N. Michelusi, M. Zorzi, "Designing intelligent energy harvesting communication systems", IEEE Communications Magazine, vol. 52, no. 1, pp. 210-216, Jan, 2014. [CrossRef]
6. V. Kyriatzis, N. S. Samaras, P. Stavroulakis, H. Takruri-Rizk, S. Tzortzios, "Enviromote: a new solar-harvesting platform prototype for wireless sensor networks", In The 18th IEEE International Symposium on Personal, Indoor and Mobile Radio Communications, Athens, Greece, 2007, pp. 1-5
7. V. Raghunathan, A. Kansal, J. Hsu, J. Friedman, M. B. Srivastava,

"Design considerations for solar energy harvesting wireless embedded systems", in The 4th IEEE International Symposium on Information Processing in Sensor Networks, CA, USA, 2005, pp. 457-462. [CrossRef]

8. P. Sikka, P. Corke, L. Overs, P. Valencia, T. Wark, "Fleck-A platform for real-world outdoor sensor networks", in The 3rd International Conference on Intelligent Sensors, Sensor Networks and Information, Melbourne, Australia, 2007, pp. 709-714. [CrossRef]
9. C. Park, P. Chou, "Power utility maximization for multi-supply systems by a load-matching switch", in The International Symposium on Low Power Electronics and Design, CA, USA, 2004, pp. 168-173.
10. F. Simjee, P. H. Chou, "Everlast: long-life, supercapacitor-operated wireless sensor node", in The International Symposium on Low Power Electronics and Design, Tegernsee, Germany, 2006, pp. 197-202. [CrossRef]
11. X. Jiang, J. Polastre, D. Culler, "Perpetual environmentally powered sensor networks," in The 4th International Symposium on Information Processing in Sensor Networks, ID, USA, 2005, pp. 463-468.
12. M. Habibzadeh, M. Hassanalieragh, A. Ishikawa, T. Soyata, G. Sharma, "Hybrid solar-wind energy harvesting for embedded applications: supercapacitor-based system architectures and design tradeoffs", IEEE Circuits and Systems Magazine, vol. 17, no. 4, pp. 29-63, Nov, 2017. [CrossRef]
13. M. Hassanalieragh, T. Soyata, A. Nadeau, G. Sharma, "UR-SolarCap: an open source intelligent auto-wakeup solar energy harvesting system for supercapacitor based energy buffering", IEEE Access, vol. 4, pp. 542-557, Jan, 2016. [CrossRef]
14. C.-Y. Chen, P. H. Chou, "DuraCap: a supercapacitor-based, power-bootstrapping, maximum power point tracking energy-harvesting system", in ACM/IEEE International Symposium on Low-Power Electronics Design, TX, USA, 2010, pp. 313-318. [CrossRef]
15. C. Renner, Volker Turau, "CapLibrate: self-calibration of an energy harvesting power supply with supercapacitors", in The 23th International Conference on Architecture of Computing Systems, Hannover, Germany, 2010, pp. 349-358.
16. D. Brunelli, C. Moser, L. Thiele, L. Benini, "Design of a solar-harvesting circuit for batteryless embedded systems", IEEE Transactions on Circuits and Systems I: Regular Papers, vol. 56, no. 11, pp. 2519-2528, Feb, 2009. [CrossRef]
17. C. Park, P. H. Chou, "AmbiMax: autonomous energy harvesting platform for multi-supply wireless sensor nodes" in The 3rd Annual IEEE Communications Society Conference on Sensor and Ad Hoc Communications and Networks, VA, USA, 2006, pp. 168-177. [CrossRef]
18. Alternative Energy Tutorials (14.07.2018). Available: http://www.alternative-energy-tutorials.com/solar-power/ solar-power.html.
19. F. I. Simjee, P. H. Chou, "Efficient charging of supercapacitors for extended lifetime of wireless sensor nodes", IEEE Transactions on Power Electronics, vol. 23, no. 3, pp. 1526-1536, May 2008. [CrossRef]
20. P. Bhatnagar, R. K. Nema, "Maximum power point tracking control techniques: state-of-the-art in photovoltaic applications", Renewable and Sustainable Energy Reviews, vol. 23, pp. 224-241, July 2013. [CrossRef]
21. H. Islam, S. Mekhilef, N. B. M. Shah, T. K. Soon, M. Seyedmahmousian, B. Horan, A. Stojcevski, "Performance evaluation of maximum power point tracking approaches and photovoltaic systems", Energies, vol. 11, no. 2, pp. 365-389, Feb, 2018. [CrossRef]
22. T. Esram, P. L. Chapman, "Comparison of photovoltaic array maximum power point tracking techniques", IEEE Transactions on Energy Conversion, vol. 22, no. 2, pp. 439-449, June 2007. [CrossRef]
23. S. Kim, K.-S. No, P. H. Chou, "Design and performance analysis of supercapacitor charging circuits for wireless sensor nodes", IEEE Journal on Emerging and Selected Topics in Circuits and Systems, vol. 1, no. 3, pp. 391-402, Sep, 2011. [CrossRef]
24. D. Dondi, A. Bertacchini, D. Brunelli, L. Larcher, L. Benini, "Modeling and optimization of a solar energy harvester system for self-powered wireless sensor networks", IEEE Transactions on Industrial Electronics, vol. 55, no. 7, pp. 2759-2766, July, 2008.[CrossRef]
25. C. Moser, L. Thiele, D. Brunelli, L. Benini, "Adaptive power management for environmentally powered systems", IEEE Transactions on Computers, vol. 59, no. 4, pp. 478-491, Apr, 2010. [CrossRef]
26. C. Bergonzini, D. Brunelli, L. Benini, "Comparison of energy intake prediction algorithms for systems powered by photovoltaic harvesters", Microelectronics Journal, vol. 40, no. 11, pp. 766-777, Nov, 2010. [CrossRef]
27. A. Kansal, D. Potter, M. B. Srivastava, "Performance aware tasking for environmentally powered sensor networks", in Joint International Conference on Measurement and Modeling of Computer Systems, NY, USA, 2004, pp. 223-234. [CrossRef]
28. J. Hsu, S. Zahedi, A. Kansal, M. B. Srivastava, V. Raghunathan, "Adaptive duty cycling for energy harvesting systems", in The International Symposium on Low Power Electronics and Design, Tegernsee, Germany, 2006, pp.180-185. [CrossRef]
29. A. Kansal, M. B. Srivastava, "Energy harvesting aware power management", Wireless Sensor Networks: A Systems Perspective, ch. 9, pp. 1-10, Artech House, MA, USA, 2005.
30. A. Kansal, J. Hsu, S. Zahedi, M. B. Srivastava, "Power management in energy harvesting sensor networks", ACM Transactions on Embedded Computing Systems, vol. 6, no. 4, pp. 1-35, Sep, 2007. [CrossRef]

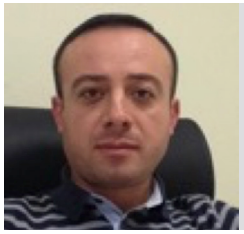

Mehmet Erkan Yüksel received his B.S. degree in Computer Engineering from Firat University in 2007, his MSc and PhD degrees in Computer Engineering from Istanbul University in 2010 and 2014, respectively. In 2015, he joined the Department of Computer Engineering at Burdur Mehmet Akif Ersoy University, where he is now an Assistant Professor. His research interest includes embedded systems, wireless communications, wireless sensor networks, software defined networks, RFID, agent-based modelling and simulation, artificial intelligence, machine learning, and data mining.

İSTANBUL UNIVERSITY
CERRAHPAŞA

RESEARCH ARTICLE
Electrica 2019; 19(1): 12-21

FPGA Based Low Cost Automatic Test Equipment for Digital Circuits

Alp Arslan Bayrakci

Department of Computer Engineering, Gebze Technical University, Kocaeli, Turkey

Cite this article as: Bayrakci AA. FPGA Based Low Cost Automatic Test Equipment for Digital Circuits. *Electrica*, 2019; 19(1): 12-21.

ABSTRACT

Testing of digital circuits is a crucial problem. There are two types of Automatic Test Equipment (ATE): Very precise but complex and expensive test equipments called high-end ATE and their approximate but cheap alternatives called low-end ATE. In this paper we propose a very cheap, FPGA based embedded low-cost ATE (ELATE) that is capable of functional, speed/delay and power consumption tests. It is composed of FPGA hardware with six FSM modules written in Verilog and a computer software (user interface) communicating with the FPGA through UART. It can handle different I/O combinations and can detect delay with 4ns precision. It can both visually show the resultant voltage/current-time graphs and store them as text files. The ATE is tested on different Design Under Test (DUT) devices like 8-bit and 12-bit adders and a square root circuit implemented on FPGA.
Keywords: FPGA, automatic test equipment, digital circuit, functional, delay, power, test

Introduction

Importance of digital circuit testing increases while the complexity and difficulty to test also increase. There are different approaches in the literature for testing of digital circuits. Tests of ASICs with hundreds of input output pins and speeds at GHz rates are really complex and difficult. On the other hand many types of digital circuit prototypes need to be tested much before manufacturing phase.

This necessitates two types of automatic test equipments (ATE): high-end and low-end. High-end ATE is powerful, fast but expensive and complex. Big companies such as Advantest [1] and Teradyne [2] construct such fast and complex ATE with multi million dollars of cost in order to test many manufactured ASICs in a small amount of time and for many input test vectors. However, they are difficult to learn and too costly to be used by many digital circuit designers.

On the other hand, low-end ATE is relatively cheap and easier to use. There are different companies like Teseda [3], which try to lower the ATE cost [4]. Recently, due to the improvements at the FPGA technology, ATE based on FPGAs are popular in the literature [5, 6, 7]. They either can only handle functional tests or require reconfigurability to be adapted to different test circuits.

In this paper, we devise an ATE, capable of performing functional, speed and power tests without the need for reconfiguration, adaptively detecting when to stop the tests and consuming a reasonable amount of space. It was first introduced in [8] roughly. In this paper, we not only present the technical implementation of ATE using software and FSMs missing in [8] but also perform more tests on different arithmetic circuits implemented on FPGA. Also the use of satisfiability (SAT) is suggested to support functional tests.

Section 2 proposes the use of satisfiability for functional test expected output computation. Section 3 explains the implemented ATE software and Section 4 gives the technical implementation of ATE hardware module by module to enable researchers implement their own ATE. Last section presents the results.

Corresponding Author:
Alp Arslan Bayrakci

E-mail:
abayrakci@gtu.edu.tr

Received: 30.04.2018

Accepted: 30.07.2018

DOI: 10.26650/electrica.2018.28093

Satisfiability for Functional Tests

Satisfiability can be used to detect the output of the circuit when a particular input is given as well as detecting true paths in the circuit.

The circuit description can be converted into a *conjunctive normal form* (CNF) formula. Each logic gate has its own CNF convertion shown in as shown in Table 1 [9]. After converting each logic gate in the circuit into the equivalent CNF form and ANDing these CNFs into one CNF representing the whole circuit, the input test vector for which the corresponding output is required, must be inserted into this circuit CNF.

Table 1. Conversion of logic gates to 3-CNF

Logic Gate	CNF
F=A' (NOT)	(A+F).(A'+F')
F=A+B (OR)	(A+B+F').(A'+F).(B'+F)
F=A.B (AND)	(A'+B'+F).(A+F').(B+F')

*All other gates can be derived from AND, OR and NOT

The resultant circuit CNF can be used to detect the expected output when the primary inputs are inserted into the CNF circuit description. For that purpose, the primary input signals with logic-1 should be directly inserted to CNF whereas for others (with logic-0) the complements of the primary input signals must be inserted into the circuit CNF. The resultant CNF formula can be given to a sat-solver [10]. As a result, all logic values for all nodes inside the circuit as well as the primary outputs can be extracted from the sat-solver result. The primary output values gathered from this result are the expected outputs for the corresponding input vector, which can be used in functional tests as expected outputs that will be clarified later.

ATE Software

Automatic test equipments software is written by C# on Visual Studio IDE. It is responsible from the communication with ATE hardware, adjustment of test vectors/settings and visualizing the test results with necessary graphics. It has to parse the incoming message from the hardware and convert it to the visual graphs and text files filled with the results. There are different tabs for settings, functional test, propagation delay test and power consumption test as shown in Figure 1.

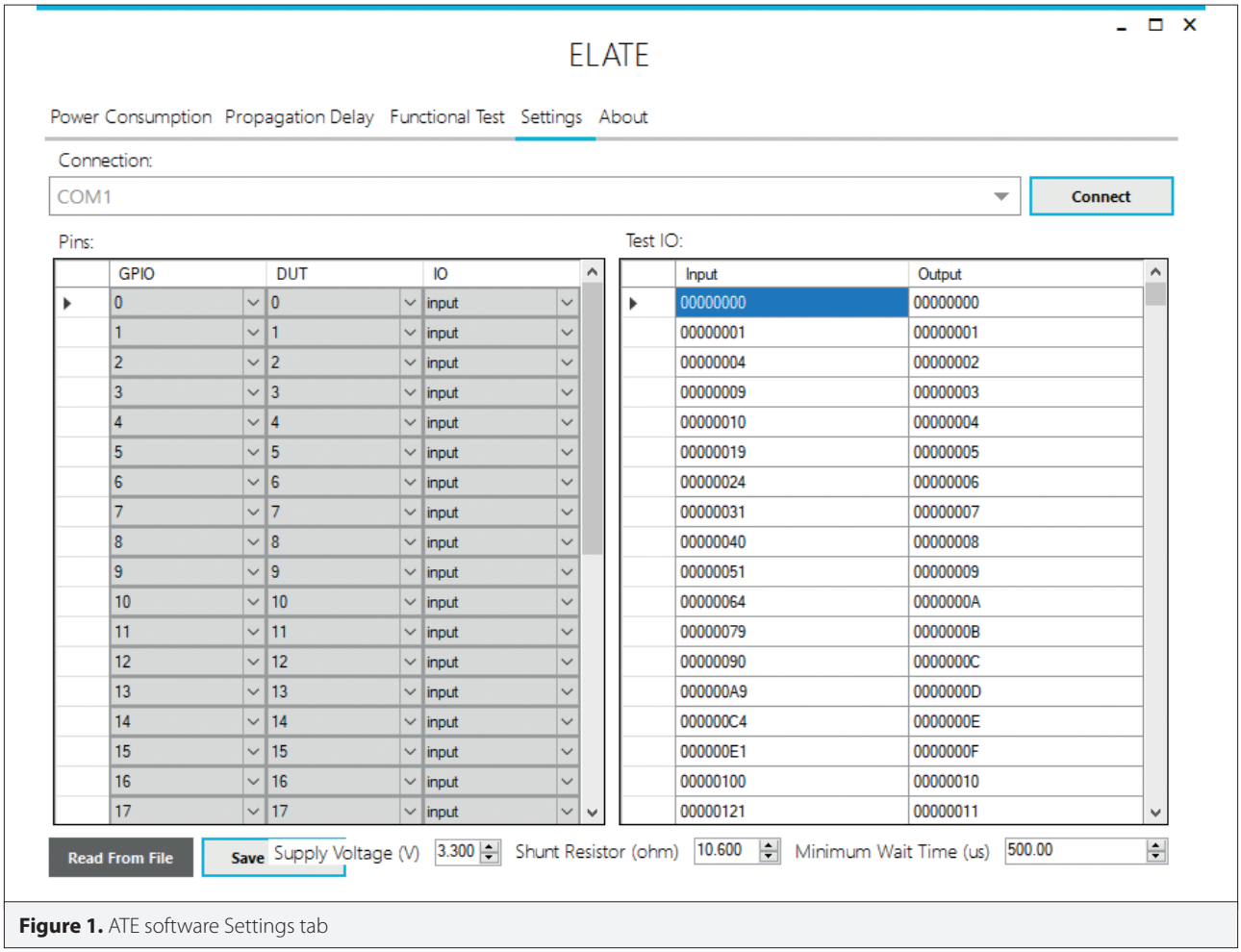

Figure 1. ATE software Settings tab

Settings tab includes four panes as shown in Figure 1. Top pane is for selecting the UART communication port with the ATE hardware. Left pane is for setting the input/output pin configurations. Right pane is for entering the input test vectors and the expected output vectors. Bottom pane is for entering the minimum wait time, supply voltage and shunt resistor values. All these settings can be saved as text file or they can be imported from a text file as shown in Figure 2. All vectors are given in hex format. This text file can be generated automatically by an automatic test pattern generation algorithm similar to the one devised in Section 2.1.

Functional test tab explained in Section 5.1 has a start test button for starting the functional test with the vectors shown in Settings tab. Each output test vector is taken from ATE hardware through UART communication and shown at the functional test tab until all test vectors are over. If the resultant actual output vector is different than the expected one it is shown with red filled cell otherwise it is shown with green filled cell.

Propagation delay tab explained in Section 5.2 has two buttons, one for starting the tests and other for saving the results to text file. There is also a graphics pane to show output signals corresponding to an input vector.

Power consumption tab is very similar to the propagation delay tab except the graph shows time vs. supply current data instead of output voltages. The resultant graphs can also be stored as jpeg or png images.

```
-input-
i0-p4
i1-p5
i2-p6
i3-p7
-output-
o13-p12
o14-p13
o15-p14
o16-p15
-io-
00000000-00000000
00000010-00001000
00000020-00002000
-wait-500-
-shunt-10.600-
-voltage-3.300-
```

Figure 2. Text file to import user settings

ATE Hardware

Proposed ATE has six main modules each of which is designed as finite state machine (FSM) in Verilog HDL and with Quartus II v16.1 software of Altera.

UART module

UART module consists of an eight state FSM for receiving data from the ATE software and a three state FSM for transmitting data to the ATE software. It is responsible not only to receive all user settings and the input test vectors but also to send back all test results to the ATE software. It is basically the slightly modified version of the module in [11]. The UART communication is handled through a USB cable using virtual COM port drivers at the computer side. Different BAUD rates can be adjusted by setting parameters inside the module.

SPI module

This is a four state FSM module, which is only used to communicate with the analog to digital converter (ADC). It implements the SPI communication protocol and reads the resultant 12 bit digital output of the ADC chip whenever a measurement is required.

Test control module

This is one of the most important modules of ATE hardware. Having an eight state FSM, it is responsible to perform the pin

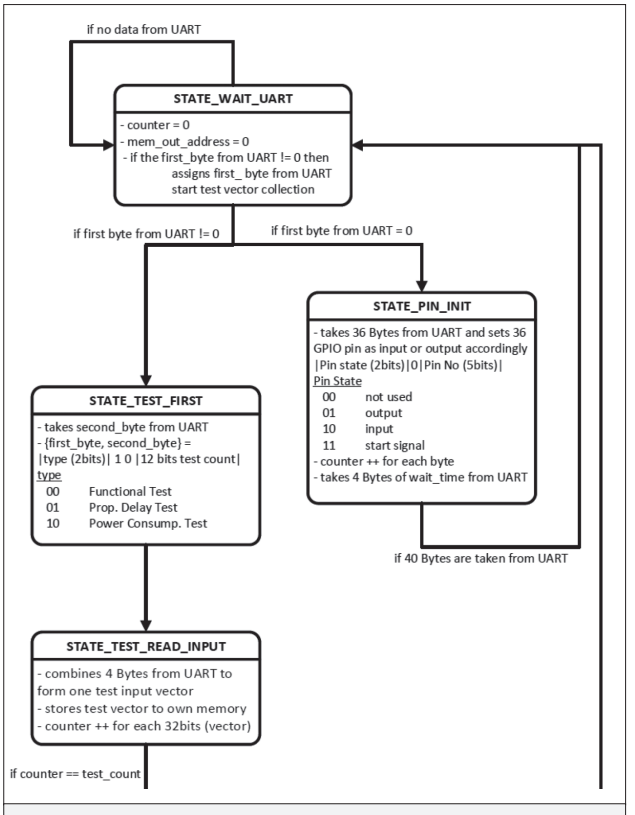

Figure 3. First four stages of Test Control Module

input/output settings according to the user inputs, store input test vectors in its internal memory, start and manage all tests. Figure 3 shows the first four states while Figure 4 shows the second four states of the module.

STATE_WAIT_UART is the idle state waiting for incoming data from UART module. When a byte of data comes it checks whether it is zero. If it is zero, it transits into STATE_PIN_INIT state, where it adjusts each GPIO pin either as input or output pin or not used. All GPIO pin settings are resolved at this state and by using the circuit shown in Figure 5.

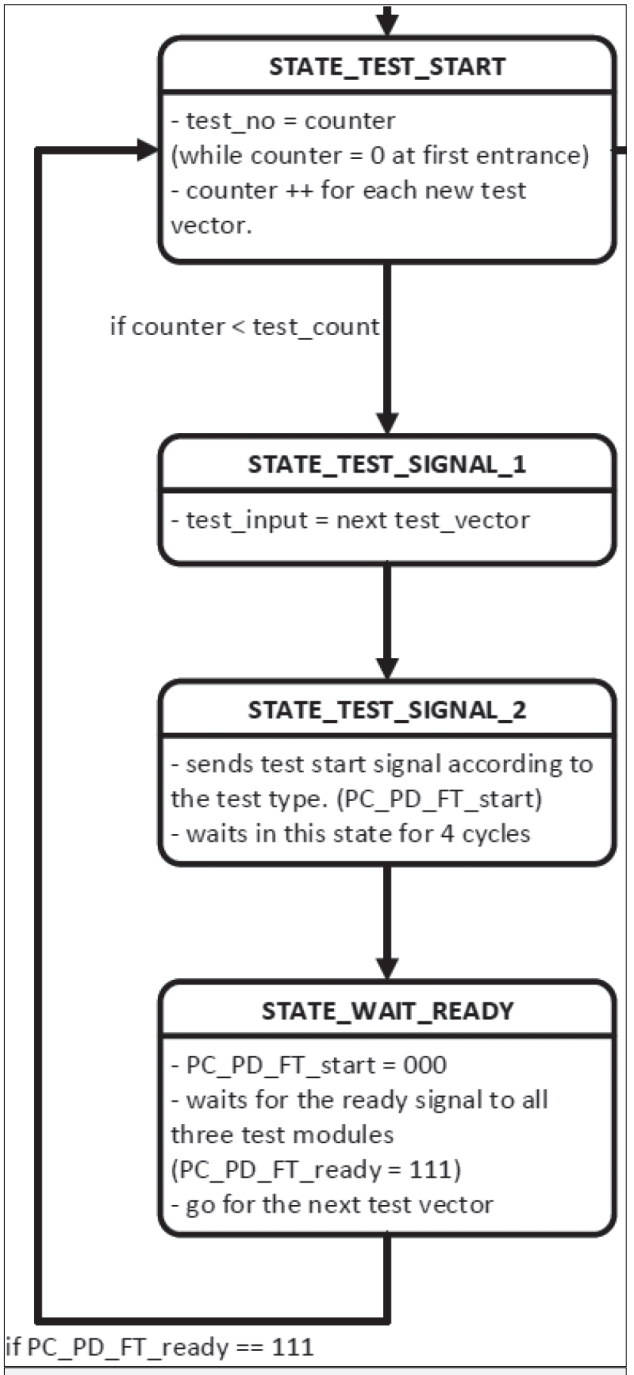

Figure 4. Second four stages of Test Control Module

In Figure 5 red output_select[31:0] signal and brown input_select[35:0] signal are determined according to the pin setttings coming from UART. These two signals adjusts a GPIO pin using the multiplexers shown by two column of rectangles in the figure. Left hand side multiplexor input signals are 36 GPIO pins whereas the input signals of right hand side multiplexors are 32 bits inputs. This circuit enables to adjust any GPIO pin of the ATE hardware as input to DUT or as output from DUT, which resolves the issue of compatibility to any test circuit with any input/output pin configuration provided that the total number of pins is bounded by 36.

This solution is better than reconfiguring the ATE hardware (FPGA) each time the DUT is changed as devised in [5].

After the multiplexor select signals are adjusted according to the current DUT by STATE_PIN_INIT state and with the first incoming byte the state changes to STATE_TEST_FIRST where two bytes incoming from UART are combined and parsed in order to understand the test type (functional, delay or power). After the test type is determined in order to receive input test vectors the next state is STATE_TEST_READ_INPUT. FSM stays at this state until all input test vectors are stored inside the internal memory of Test Control Module.

Last four states shown in Figure 4 are used for testing the DUT with each input test vector. The next two states (…TEST_START and …_SIGNAL_1) are responsible from sending the next stored input test vector to the corresponding test module. Then, STATE_TEST_SIGNAL_2 sends the start signal to the same module. This start signal activates the corresponding module that is responsible for finalizing the test and sending all results back to ATE software via UART module. STATE_WAIT_READY state waits until the testing for the corresponding test vector finishes and all results are sent back. After all tasks corresponding to the current input test vector finishes, the next test is initiated until all input test vectors are utilized and test is over.

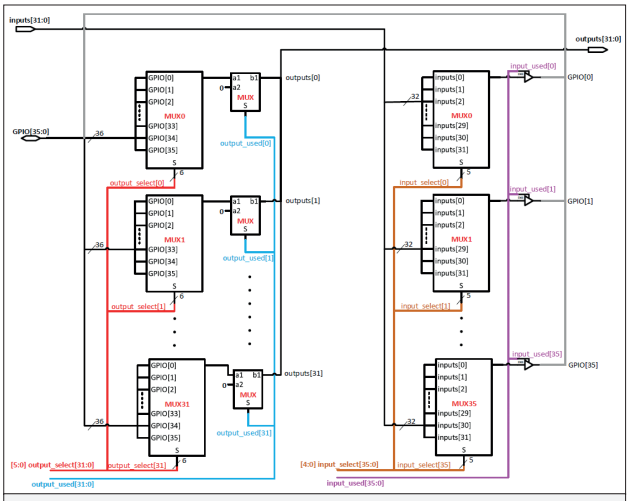

Figure 5. Pin Adjustment circuit in Test Control Module

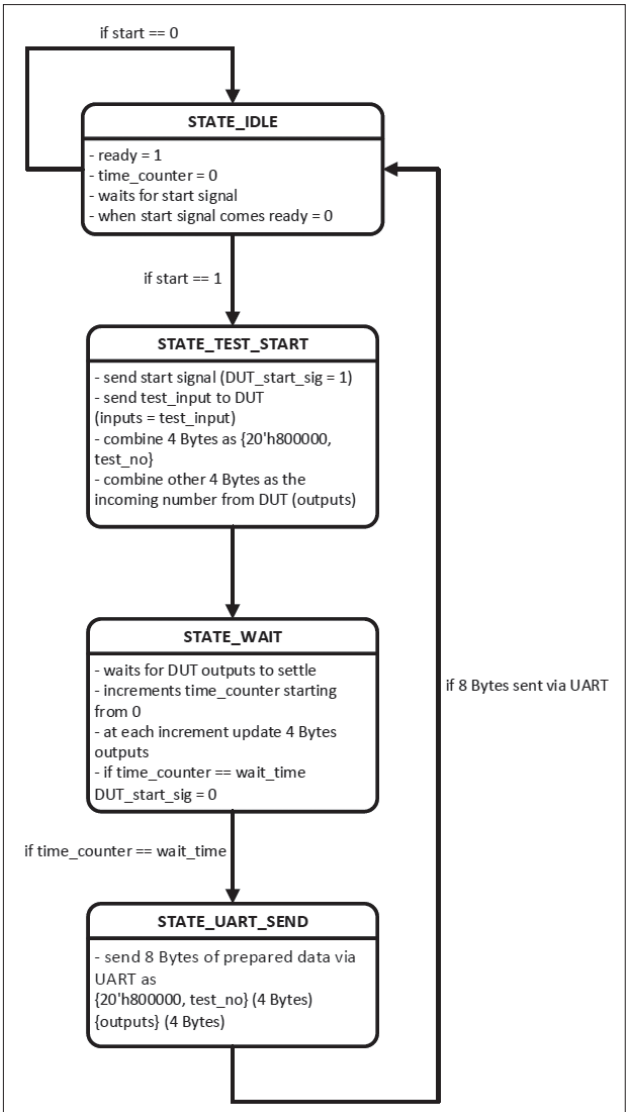

Figure 6. Functional Test Module FSM

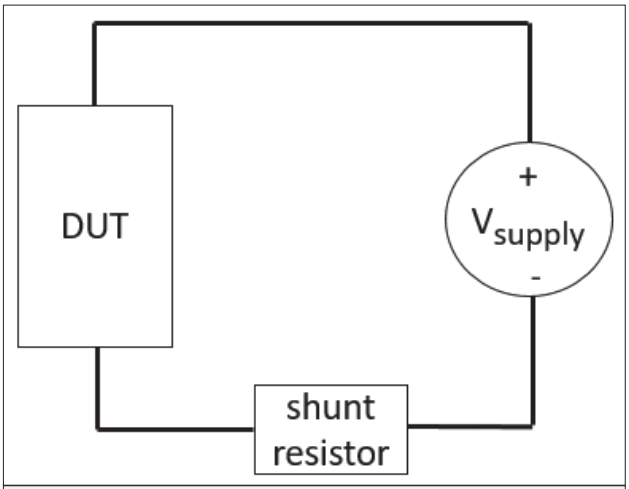

Figure 7. Connection of shunt resistor for power tests

Functional test module

This module has four states as shown in Figure 6. It waits at STATE_IDLE until a start signal comes from Test Control Module. Start signal initiates the test by transisiton to STATE_START_TEST state, where it connects the current test vector coming from Test Control Module to the DUT inputs. Then it changes into STATE_WAIT state where it stays until the outputs are stabilized.

This part is crucial in order to ignore glitches at any of the outputs. At this state, it waits a user given amount of time, which is specified through ATE software Settings Tab. During that time period if any of the outputs changes the timer is reset to zero. As a result, this state can only be exited when none of the outputs changes during the user specified minimum wait time. This guarantees that the outputs are stabilized. Resultant stable DUT outputs are recorded and the state changes to STATE_UART_SEND where the resultant DUT output is sent back to ATE software through UART Module. Then for the next input test vector, the iteration restarts from STATE_IDLE until all test iterations are over.

Here there is another critical choice of sending all data corresponding to a test vector back to ATE software before starting next test. This method results in much lower memory utilization than storing all data corresponding to all test vectors.

Propagation delay test module

This module has four states. It is very similar to the functional test module except it traces the time information and also records the time instant at which an alteration occurs at one of the outputs. It checks the output signals 250,000,000 times in one second, i.e. with 4 nanoseconds intervals, which means that it cannot precisely detect delays for circuits faster than 250MHz.

The main problem of this method is that recording the output signals 250 million times in one second require a huge amount of space. Nonetheless, output alterations must be recorded in order to visually see the voltage vs. time plots of all output signals. We avoid this issue by just recording the times that an output signal changes inside the memory module. By this way, instead of 250 million records, the number of records are limited by the number of output alterations. Allowing about 32000 alterations, a 256KB memory is practically enough. Second precaution is that all data corresponding to an input test vector is sent back to ATE software before starting the new test with the next input test vector.

Power consumption test module

This module has four states similar to the functional test module. It stays at STATE_IDLE until a start signal comes. Then it transits into STATE_ADC_READ, where it starts the analog to digital conversion of the voltage over the the shunt resistor connected to the circuit as in Figure 7. The voltage values are read via SPI Module at this state.

```
-input-
i0-p4
i1-p5
i2-p6
i3-p7
-output-
o13-p12
o14-p13
o15-p14
o16-p15
-io-
00000000-00000000
00000010-00001000
00000020-00002000
-wait-500-
-shunt-10.600-
-voltage-3.300-
```

```
STATE_BEGIN: begin

    num <= GPIO[19:0];
    square <= 20'd0;
    d <= 12'd1;
    root <= 12'd0;
    flag <= 0;
    next_state <= STATE_WHILE;
    end

STATE_WHILE: begin
    if(square <= num) begin
        root <= root + 12'd1;
        square <= square + d;
        d <= d + 12'd2;
        end

    else if(!flag) begin
        root <= root - 1;
        flag <= 1;
        end

    if(flag == 1 && num != GPIO[19:0]) begin
        next_state <= STATE_BEGIN;
        end
    end
```

Figure 8. Integer square root implemented as FSM (root=sqrt (num))

At this point, it is important to know when to stop the ADC readings. In our solution, the reading of the analog voltage values continues until the values return back to the values at the idle state, which means that the dynamic power consumption due to the given input test vector is over.

The last state named as STATE_UART_SEND sends all recorded data of the current input test vector back to the ATE software through UART module as it is done in delay test. Then the FSM returns back to the initial state, i.e. STATE_IDLE in order to start the test for the next input test vector coming from Test Control Module.

Again the strategy to send back all data of the current test vector before switching to the next test vector avoids the memory insufficiency. Another technique that helps that is to avoid any recording unless there is a significant change in the shunt resistor voltage values, which is used to compute the instantaneous current drawn from the supply, and plotted as current vs. time graph.

ELATE

Power Consumption | Propagation Delay | Functional

Test No	Input	Output	Result
0	00001A81	009B0000	009B0000
1	00006368	00CB0000	00CB0000
2	00008DF3	01800000	01800000
3	0000F15C	014D0000	014D0000
4	00001B4D	00680000	00680000
5	00001981	008A0000	009A0000
6	00001275	00870000	00870000
7	0000BB88	01430000	01430000
8	00007040	00B10000	00B00000
9	0000EA8B	01750000	01750000
10	0000F836	012E0000	012E0000
11	00009EF0	018E0000	018E0000
12	00008595	011A0000	011A0000
13	0000A991	013A0000	013A0000
14	00009F99	00380000	01380000
15	0000ED19	01060000	01060000
16	00004CFB	01470000	01470000
17	0000CBB1	017C0000	017C0000
18	000028B7	00DF0000	00DF0000
19	0000DFDD	01BC0000	01BC0000
20	0000B813	00CB0000	00CB0000

Figure 9. 8-bit adder functional test result

Results

The test circuits are implemented on Altera Cyclone V GX board of Terasic. Tests performed for 8-bit, 12-bit adders and a square root unit written in Verilog by Quartus II tool. All test vectors are generated by a C program and given as text file input to the ATE software.

The minimum wait time supplied by the user is determined adaptively by checking the functional test results and increasing the minimum wait time until all results match with the expected ones.

We implemented a square root arithmetic circuit unit on Altera Cyclone V FPGA by writing the module with two state FSM as shown in Figure 8. It takes 20 bits of input and 12 bits of output as the integer square root of the input. The adders are written in behavioral Verilog using the classical '+' operator.

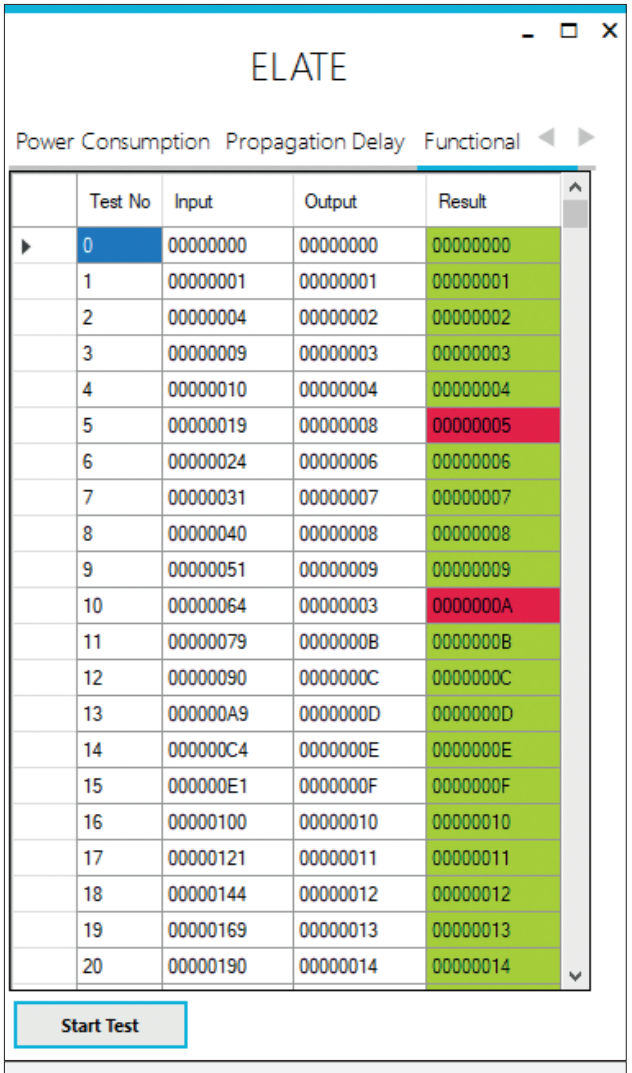

	Test No	Input	Output	Result
▶	0	00000000	00000000	00000000
	1	00000001	00000001	00000001
	2	00000004	00000002	00000002
	3	00000009	00000003	00000003
	4	00000010	00000004	00000004
	5	00000019	00000008	00000005
	6	00000024	00000006	00000006
	7	00000031	00000007	00000007
	8	00000040	00000008	00000008
	9	00000051	00000009	00000009
	10	00000064	00000003	0000000A
	11	00000079	0000000B	0000000B
	12	00000090	0000000C	0000000C
	13	000000A9	0000000D	0000000D
	14	000000C4	0000000E	0000000E
	15	000000E1	0000000F	0000000F
	16	00000100	00000010	00000010
	17	00000121	00000011	00000011
	18	00000144	00000012	00000012
	19	00000169	00000013	00000013
	20	00000190	00000014	00000014

Figure 10. Square root functional test result

Functional test results

The results of functional test for 8-bit adder and square root units are shown by Figure 9 and 10 respectively. Only the first 20 test vectors are shown for demonstration purposes. The input column shows the input vector, the output column shows the expected output and the result column shows the actual result taken from DUT. Green represents that the DUT result is same as the expected output. As it is seen in both figures there are red entries which means that the result is different from the expected output. The red entries are made intentionally in order to show that the ATE works accurately. In other words, for the red entries, we intentionally write wrong numbers as expected output.

In Figure 9, the 6th input 00001275 means that the adder takes $(12)_{16}$ and $(75)_{16}$ as input numbers to be added and the result is $(87)_{16}$, which is written as 00870000 as the two digits next to the most significant two digits represent the output of DUT. The 5th entry is red because the addition result is different than the expected output, which is intentionally written false.

Similarly in Figure 10, the 10th input is 00000064 means that the input number is $(64)_{16}$ and the actual square root result is 10 which is shown as 0000000A. It is shown as red because we intentionally write $(003)_{16}$ as the expected output to check the proposed ATE.

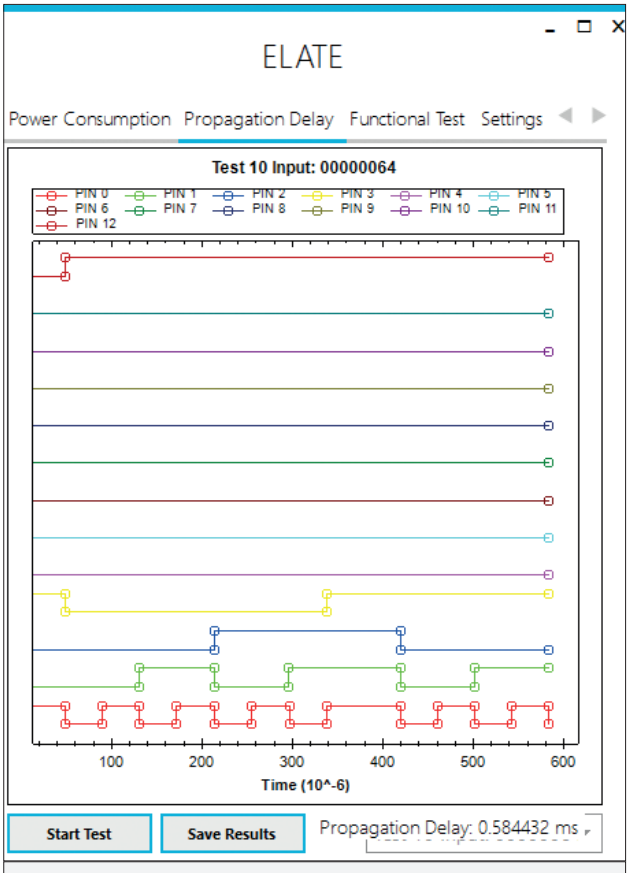

Figure 11. Propagation delay plot for input test vector $(64)_{16}$

Functional tests with 1024 random samples for each of all three test circuits resulted accurately.

Propagation delay test results

Propagation delay for square root test circuit is computed for 512 input test vectors increasing from 0 to 512^2. Therefore the resultant square root results are 0, 1, …, 512.

Figure 11 shows DUT outputs vs. time graph for a sample input test vector given to square root unit. It belongs to input 100 for which the resultant root is 10 as expected. As it is seen at the end of the plot at Figure 11 the result for 100 (64 in hex) comes out to be 10, i.e. 0000 0000 1010. The worst case delay for the square root circuit is 29.8ms whereas the average delay is 11.3ms with increasing nature of delay by the increasing input value.

The propagation delay results for different test circuits are shown in Table 2. Average delay column shows the average delay for 1024 different test vectors generated randomly whereas the worst case delay column represents the worst delay among these 1024 test vectors.

The resultant worst case delay is higher for 8-bit adder although the average delay is smaller. This is because the 1024 input test vectors are selected randomly using srand() in C. But the average delay represents the characteristic better than the worst case one. Also in FPGAs, the delay depends on the usage of LUTs which may result in a convergence for the delays of 8-bit and 12-bit adders if same number of LUTs are utilized for both.

Table 2. Average and worst case delay for test circuits

Circuit	Average Delay	Worst Case Delay
8-bit Adder	44.5ns	112ns
12-bit adder	49.5ns	84ns

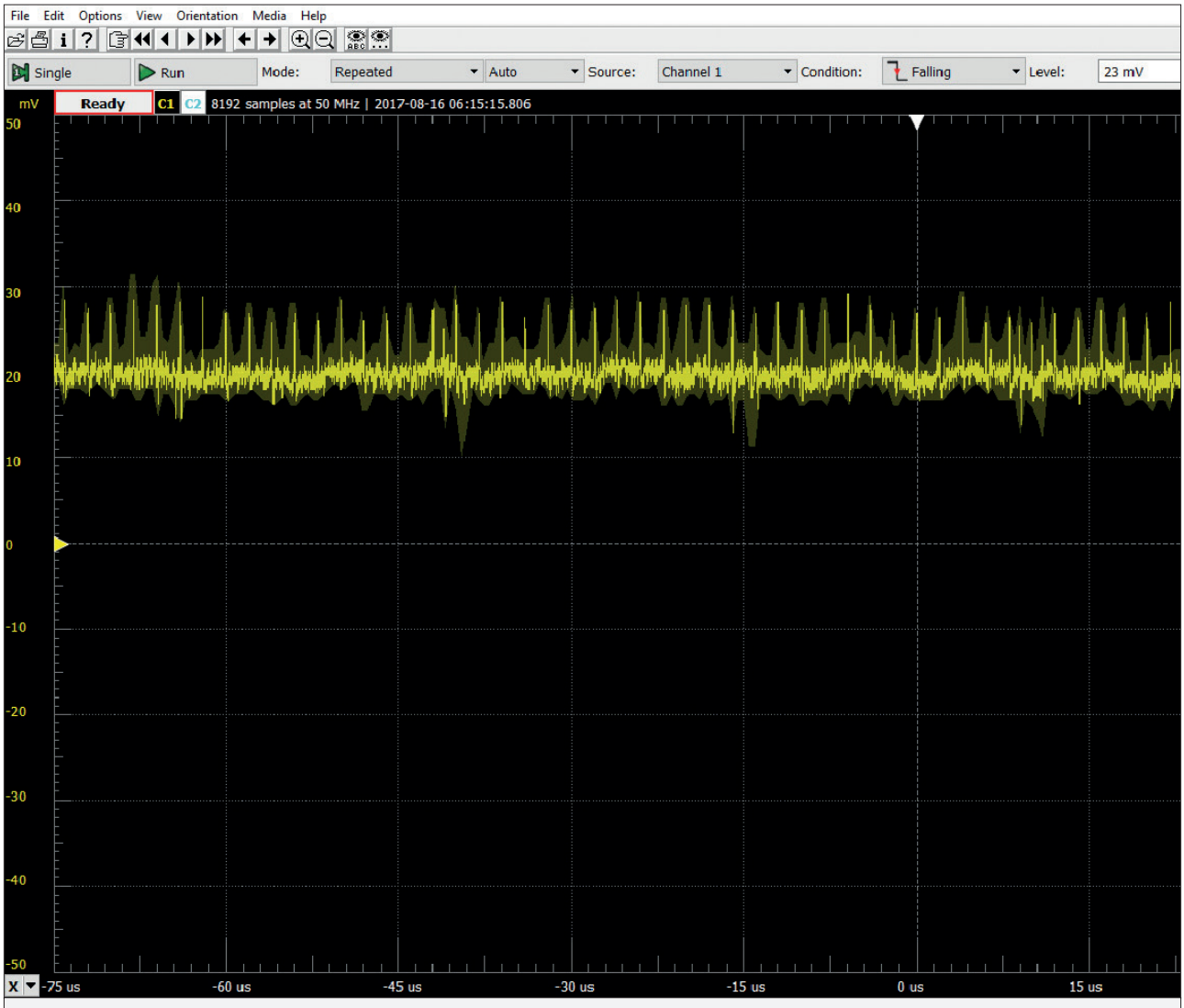

Figure 12. Oscilloscope output for shunt resistor voltage

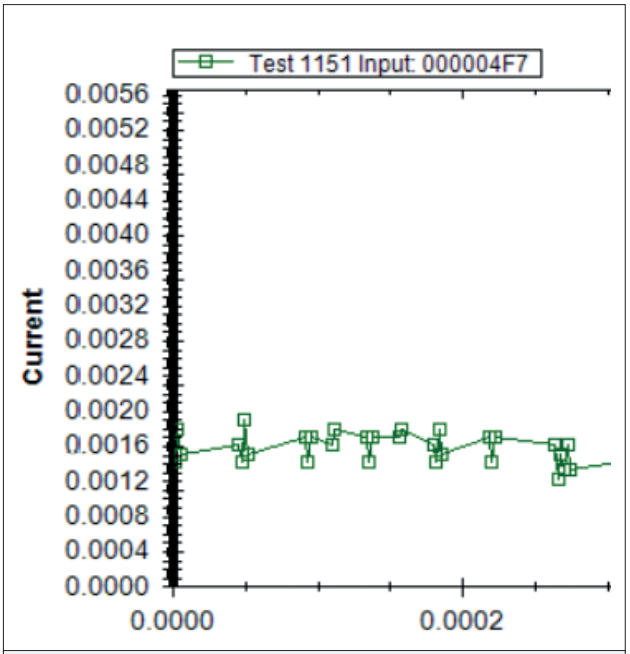

Figure 13. Square root circuit current-time graph

Power consumption test results

Power consumption is the weakest part of our ATE. Because the sampling rate of the used ADC is as low as 500ksps, therefore the dynamic current fluctuations in nanosecond intervals cannot be captured by our ADC. However we tested the accuracy of our power consumption test by comparing with the Analog Discovery oscilloscope output where we only manage to measure the idle power consumption for the Stellaris Lauchpad MCU development board of Texas Instruments. Figure 12 shows the Analog Discovery oscilloscope output for shunt resistor voltage for 100us interval and Figure 13 shows the resultant ATE shunt resistor current plot captured by ATE software for 300us interval. As the shunt resistor is about 11Ohm both plots give similar results which emprically verify the power consumption test result of ATE.

Conclusion

The proposed ATE performs very well in all functional tests. Although the final output voltage values are accurate for propagation delay voltage-time plots, further investigation and improvement are required in order to be sure about the actual delay. For that purpose precise tools to detect the actual delay of the circuits can be employed. Power consumption tests are working but the sampling rate of ADC must be really very high in tens of GHz in order to detect dynamic supply current changes. However, ATE proposed in this paper constitutes a good start from scratch and this model can further be improved by inserting more expensive but precise hardware as well as hardware and software enhancements.

Peer-review: Externally peer-reviewed.

Conflict of Interest: The author has no conflicts of interest to declare.

Financial Disclosure: This work is supported by The Scientific and Technological Research Council of Turkey (TUBITAK) under Grant No. 116E296.

References

1. IC Test Systems – Advantest (March 2018).Available: https://www.advantest.com/products/ic-test-systems.
2. Production Board Test Teradyne (March 2018). Available: http://www.teradyne.com/products/production-board-test.
3. Teseda Corporation: Silicon Failure Analysis and Yield Enhancement (March 2018). Available: http://www.teseda.com.
4. Teseda breaks $200 per pin ATE barrier (March 2018). Available: http://www.eetimes.com/document.asp?doc_id=1175064.
5. L. Mostardini, L. Bacciarelli, L. Fanucci, L. Bertini, M. Tonarelli, M. De Marinis, "FPGA-based low-cost automatic test equipment for digital integrated circuits", IEEE International Workshop on Intelligent Data Acquisition and Advanced Computing Systems: Technology and Applications, Rende, pp. 32-37, 2009. [CrossRef]
6. J. H. M. Escobar, J. SachBe, S. Ostendorff, H. D. Wuttke, "Automatic generation of an FPGA based embedded test system for printed circuit board testing", 13th Latin American Test Workshop (LATW), Quito, Ecuador, pp. 1-6, 2012. [CrossRef]
7. I. Aleksejev, A. Jutman, S. Devadze, S. Odintsov, T. Wenzel, "FPGA-based synthetic instrumentation for board test," IEEE International Test Conference, Anaheim, CA, pp. 1-10, 2012. [CrossRef]
8. A. A. Bayrakci, "ELATE: Embedded low cost automatic test equipment for FPGA based testing of digital circuits", 2017 10th International Conference on Electrical and Electronics Engineering (ELECO), Bursa, 2017, pp. 1281-1285.
9. F. S. Marques, R. P. Ribas, S. Sapatnekar, and A. I. Reis. "A new approach to the use of satisfiability in false path detection." Proceedings of the 15th ACM Great Lakes symposium on VLSI (GLSVLSI '05). ACM, New York, NY, USA, pp 308-311, 2005. [CrossRef]
10. N. Eén, N. Sörensson. "An extensible SAT-solver", International conference on theory and applications of satisfiability testing. Springer, Berlin, Heidelberg, 2003.
11. Documented Verilog UART (March 2018). Available: https://opencores.org/project/osdvu.

Alp Arslan Bayrakçı received the B.S. degree in electrical and electronics engineering from Middle East Technical University, Ankara, Turkey, in 2004, and the Ph.D. degree in computer engineering from Koç University, Istanbul, Turkey, in 2010. He has been with Gebze Technical University, Gebze, Turkey, since 2011. His current research interests include statistical timing analysis, hardware security, and computer-aided design methodologies.

İSTANBUL UNIVERSITY
CERRAHPAŞA

RESEARCH ARTICLE
Electrica 2019; 19(1): 22-28

Comparative Analysis of Wind Speed Models Using Different Weibull Distributions

Emrah Dokur[1], Salim Ceyhan[2], Mehmet Kurban[1]

[1]Department of Electrical Electronics Engineering, Bilecik Şeyh Edebali University, Bilecik, Turkey
[2]Department of Computer Engineering, Bilecik Şeyh Edebali University, Bilecik, Turkey

Cite this article as: Dokur E, Ceyhan S, Kurban M. Comparative Analysis of Wind Speed Models Using Different Weibull Distributions. *Electrica*, 2019; 19(1): 22-28.

ABSTRACT

A wide variety of distribution functions are used in the literature for wind speed modelling. It is the most widely used Weibull distribution (WD) function in wind speed modelling. In this paper, two-parameter WD, Rayleigh distribution (RD) which is a special form of WD, and Inverse Weibull distribution (IWD) offered for a new seasonal wind speed modelling are considered and analyzed for six different regions (Gökçeada, Bozcaada, Bandırma, Bilecik, Yalova and Sakarya regions) in the Northwest of Turkey, comparatively. The hourly wind speed data for the period of October 2015 to 30 September 2016 is taken from Turkish State Meteorological Service. As a result of the comparison, it is seen that the WD is generally suitable, although IWD has good seasonal results in some regions. All the comparative results are given in tables.
Keywords: Wind speed modeling, weibull distribution, rayleigh distribution, inverse weibull distribution

Introduction

Energy is one of the most important parts of our life. Clean form of energy production in parallel with the needs of today's growing demand for power is of great importance. Thus, the use of renewable energy resources is increasing rapidly. Consequently, it is foreseen that the renewable energy resources in the generation systems will increase by the year 2020 rapidly and the major part of these resources will be wind energy as 12% [1]. Hence, wind energy conversation systems have great importance among renewable energy sources.

The detailed information of wind data characteristics such as direction, speed and duration should be investigated while determining the wind energy potential for the selected region [2]. Several distribution functions were proposed for wind speed modelling in literature. The two-parameter Weibull [3-5], the log-normal distribution [6-9], the inverse Gaussian distribution [10], the wake by [11, 12], three-parameter log normal [13], the gamma distribution [14, 15], two-parameter gamma distribution [16], hybrid distributions [17, 18], Finsler geometry approach [19], the three parameter generalized gamma distribution [20, 21],and similar distribution functions were used about energy and other research areas.

The use of Inverse Weibull distribution (IWD) function on the purpose of wind speed modeling is proposed by Akgül et al. [22]. Two parameter Weibull distribution (WD) and IWD are compared for the seasonal wind speed data in their study. The aim of this paper is to addresses that monthly and seasonal wind speed data for six different regions of Turkey are modeled using WD,IWD and Rayleigh distributions (RD) function, comparatively. Analyses are made for the regions taken from stations of the Marmara region which have low and high wind speed regimes. Especially, the modelling performance of the IWD is compared with the WD and RD for monthly analysis. This paper is structured as follows: the WD,RD and IWD methods are explained by Section 2. Comparative modelling results for monthly and seasonal analysis are presented in Section 3. Finally, conclusions are given in Section 4.

Corresponding Author:
Emrah Dokur

E-mail:
emrah.dokur@bilecik.edu.tr

Received: 23.05.2018

Accepted: 05.08.2018

DOI: 10.26650/electrica.2018.28091

Methods for Wind Speed Modelling

The two-parameter WD function that is suitable for wind speed modelling is given by Equation (1):

$$f(\mathrm{v}) = \frac{k}{c}\left(\frac{v}{c}\right)^{k-1} e^{-\left(\frac{v}{c}\right)^{k}}, \tag{1}$$

where f(v) is the probability density function (pdf) of wind speed v, the Weibull scale parameter is c which has with unit equals to the wind speed unit (m/s) and, the shape parameter of WD is k. While the value of k shows the wind speed, higher c indicates more stability [23].

The cumulative distribution function (cdf) of WD, F(v) is expressed by the following Equation (2) [24-25]:

$$\mathrm{F(v)} = 1 - e^{-\left(\frac{v}{c}\right)^{k}}. \tag{2}$$

The Rayleigh is a special form of WD function in which the shape factor of the WD is a fixed value (k=2).

The pdf and cdf of IWD are given in below [22]:

$$f_{IWD}(\mathrm{v}) = \frac{k}{c}\left(\frac{v}{c}\right)^{-k-1} e^{-\left(\frac{v}{c}\right)^{-k}} \tag{3}$$

and

$$\mathrm{F}_{IWD}(\mathrm{v}) = e^{-\left(\frac{v}{c}\right)^{-k}}. \tag{4}$$

There are several methods for estimating of k and c parameters, such as maximum likelihood method, graphical method, method of Justus, method of Lysen, power density method, information geometry method etc. [26-29]. In this paper, maximum likelihood methods is used for parameter estimation [30].

k and c parameters are calculated for WD by Equation (5, 6). Where n is number of observed wind speed data.

$$k = \left(\frac{\sum_{i=1}^{n} v_i^{k} \ln(\mathrm{v}_i)}{\sum_{i=1}^{n} v_i^{k}} - \frac{\sum_{i=1}^{n} \ln(\mathrm{v}_i)}{n}\right)^{-1} \tag{5}$$

$$c = \left(\frac{\sum_{i=1}^{n} (v_i)^{k}}{\sum_{i=1}^{n} v_i^{k}}\right)^{1/k} \tag{6}$$

The determination of scale and shape parameter for IWD are given in below;

$$k = \frac{n\sum_{i=1}^{n} v_i^{-k}}{\sum_{i=1}^{n} \ln \mathrm{v}_i \sum_{i=1}^{n} v_i^{-k} - n\sum_{i=1}^{n} v_i^{-k} \ln v_i} \tag{7}$$

$$c = \left(\frac{n}{\sum_{i=1}^{n} v_i^{-k}}\right)^{1/k} \tag{8}$$

Performance criteria of analysis is shown by using Root Mean Square Error (RMSE) in Equation (9).

$$RMSE = \sqrt{\frac{1}{n}\sum_{i=1}^{n} (\mathrm{y}_i - \mathrm{x}_i)^2} \tag{9}$$

Where, y_i and x_i are observed and estimated wind speed probability value, respectively. And the number of observations is expressed as n.

Comparative Analysis of Wind Speed Models

In this paper, the six different regions which have low and high wind speed characteristics are comparatively analyzed by the three different methods. Wind speed data, consisting of hourly wind speed records between October 2015-September 2016 were obtained from the Gökçeada, Bozcaada, Bandırma, Bilecik, Yalova and Sakarya Meteorological Stations. They are located in Northwest of Turkey, Marmara region, as shown in Figure 1.

The biggest island of Turkey is Gökçeada which is in the Northern Aegean Sea and also another island in Aegean Sea is Bozcaada. Bandırma, Bilecik, Yalova and Sakarya in Marmara region are located close to each other as shown in Figure 1. The geographical data and wind speed period for these region are given in Table 1.

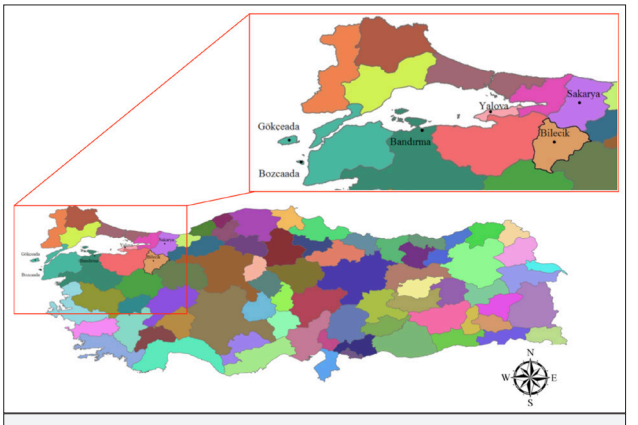

Figure 1. Locations of the sample wind speed data regions in Turkey

Table 1. The geographical data and wind data period of six different regions

Station	Latitude (oN)	Longitude (oE)	Altitude (m)	Wind Data Period
Bandırma	40° 21'	27o 58'	20	October 2015-September 2016
Sakarya	40° 46'	30o 22'	31	October 2015-September 2016
Yalova	40° 39'	29o 15'	30	October 2015-September 2016
Bozcaada	39° 48'	26o 02'	20	October 2015-September 2016
Gökçeada	40° 10'	25o 50'	48	October 2015-September 2016
Bilecik	40° 05'	30o 05'	850	October 2015-September 2016

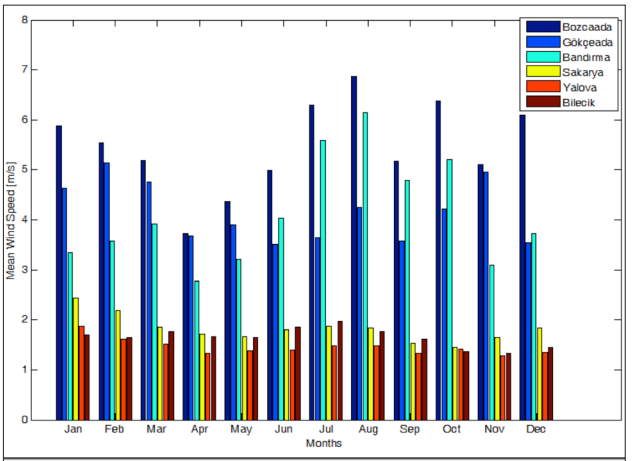

Figure 2. Mean wind speed data for six region

Mean wind speed data for six regions are given in Figure 2. Bozcaada, Bandırma and Gökçeada have higher wind speed profile than Sakarya, Bilecik and Yalova.

The IWD function for wind speed modeling was proposed for seasonal analysis by Akgül et al. [22]. In this paper, the performance of Inverse Weibull Distribution function not only in seasonal analyzes but also in monthly analyzes is realized for different regions. The monthly analysis for six different regions using IWD, WD and RD methods are given in Table 2. Root Mean Square Error (RMSE) that is given in Equation (9) is selected for performance criteria.

As seen in Table 2, Two-parameter Weibull distribution is suitable model for Bandırma region. However, Rayleigh distrubition is better than WD for January and February of Bandırma region. The IWD and WD methods are shown to be suitable for Sakarya region. In particular, the IWD method for monthly analysis seems more appropriate for the Sakarya and Yalova regions than other regions. Especially, the performance of IWD method is good fit for eight months in Yalova. WD method has better performance than the other methods for other regions that are Bilecik, Gökçeada and Bozcaada.

The methods are compared in terms of seasonal analysis perspective in the Table 3. When the analyzes are considered as seasonally, it can be seen that the two-parameter WD method is generally more appropriate than the other methods. The IWD method gives good fit only winter and summer that have Sakarya and Yalova, respectively.

It is important that to determine the wind characteristics of wind resource in site where the wind energy system will be adapted. In order to achieve a feasible project, many observations, analyses and calculations must be done. For the wind resource analysis the wind characteristics of the site must be determined. Important performance criterion for the wind energy conversion system is energy output calculations. Energy production of a wind turbine is predicted by monitoring its energy output over long time periods. At the design stage of wind energy system, for energy calculations conventional approaches are followed such as Weibull or Rayleigh. In addition, IWD which is the special form of Weibull is proposed in the literature. In this study focuses specifically on matching the structure and performance of different Weibull distributions.

As a result of the comparison, it is seen that the WD is generally suitable, although IWD has good seasonal results in some regions in Table 3.

Conclusion

In this paper, the six different regions of Turkey are analysed for wind speed data records between October 2015-September 2016 using WD, IWD and RD comparatively. The following conclusions of this study can be obtained as:

The IWD method was newly proposed for seasonal wind speed modeling in literature. In this study, monthly and seasonal analysis for six different regions that have different wind speed profiles are presented using three different methods, comparatively. In this context, the IWD appears to be a suitable method for some regions that are Yalova and Sakarya which have low wind speed profile.

Table 2. The results of comparative monthly analysis of six regions using WD, IWD and RD

		BANDIRMA			SAKARYA			BOZCAADA			YALOVA			GÖKÇEADA			BILECIK		
Months	**Methods**	**k**	**c**	**RMSE**	**k**	**c**	**RMSE**	**k**	**c**	**RMSE**	**k**	**c**	**RMSE**	**k**	**c**	**RMSE**	**k**	**c**	**RMSE**
January	WD	1.5623	3.7486	0.0582	1.9682	2.7627	0.0919	1.8045	6.6232	0.0307	1.7410	2.3207	0.0880	1.3428	5.0590	0.0418	1.6461	1.9157	0.0953
	IWD	1.1515	2.9619	0.0600	1.1924	1.8577	0.0823	0.9265	3.7083	0.0475	1.0463	1.4903	0.0794	0.8861	3.2446	0.0445	1.0408	1.4973	0.1001
	RD	2.0000	2.8730	0.0544	2.0000	1.9608	0.1013	2.0000	4.8133	0.0418	2.000	1.7013	0.1090	2.0000	4.1057	0.0609	2.000	1.4372	0.1138
February	WD	1.4723	3.9865	0.0526	1.9261	2.4819	0.0755	1.6015	6.1965	0.0367	2.1647	1.8286	0.1189	1.3051	5.5598	0.0428	1.8733	1.8738	0.0837
	IWD	1.0543	3.0466	0.0542	1.3922	1.9224	0.0726	0.9071	3.6235	0.0407	1.5447	1.5618	0.1301	0.7942	3.0087	0.0459	1.2361	1.4339	0.0861
	RD	2.0000	3.1593	0.0497	2.0000	1.7710	0.0744	2.0000	4.6698	0.0521	2.000	1.2713	0.1369	2.0000	4.4978	0.0666	2.000	1.3470	0.1008
March	WD	1.4180	4.3319	0.0450	2.0228	2.1096	0.0826	1.7867	5.8550	0.0325	2.1652	1.7105	0.1569	1.5189	5.2773	0.0401	1.9676	2.0109	0.0586
	IWD	1.0324	3.3361	0.0483	1.3296	1.6490	0.0890	1.1443	3.8262	0.0365	1.5903	1.4862	0.1680	0.7970	2.8500	0.0495	1.0602	1.3871	0.1043
	RD	2.0000	3.4856	0.0544	2.0000	1.4878	0.1089	2.0000	4.2631	0.0433	2.000	1.1888	0.1615	2.0000	4.0362	0.0581	2.000	1.4274	0.1136
April	WD	1.4740	3.0964	0.0656	1.9425	1.9414	0.1078	1.6364	4.1676	0.0460	2.1101	1.5135	0.1542	1.2784	3.9648	0.0544	1.9534	1.8862	0.0809
	IWD	1.1083	2.5888	0.0753	1.3709	1.5494	0.1102	0.8152	2.2832	0.0601	1.4875	1.3092	0.1703	0.8169	2.3124	0.0629	1.2219	1.4635	0.1021
	RD	2.0000	2.4504	0.0685	2.0000	1.3825	0.1190	2.0000	3.1097	0.0702	2.000	1.0575	0.1692	2.0000	3.2268	0.0931	2.000	1.3414	0.1189
May	WD	1.8045	3.6287	0.0507	2.1874	1.8982	0.1076	2.0583	4.9181	0.0413	2.4932	1.5593	0.1907	1.5182	4.3269	0.0460	2.0486	1.8816	0.0769
	IWD	1.2190	2.6545	0.0528	1.4121	1.4535	0.1083	0.8346	2.5515	0.0804	1.6508	1.1059	0.1504	0.9244	2.5723	0.0553	1.2414	1.4124	0.1036
	RD	2.0000	2.6356	0.0606	2.0000	1.3171	0.1434	2.0000	3.4576	0.0710	2.000	1.0614	0.2423	2.0000	3.3112	0.0692	2.000	1.3234	0.1301
June	WD	1.6328	4.5150	0.0477	2.0188	2.0526	0.1027	1.6549	5.5660	0.0355	2.4608	1.5837	0.1890	1.5583	3.9031	0.0855	2.1354	2.0912	0.0619
	IWD	1.1530	3.1024	0.0520	1.3476	1.5468	0.0891	0.8038	2.6544	0.0554	1.7143	1.3308	0.1866	0.8461	1.7734	0.1209	1.2414	1.4124	0.1011
	RD	2.0000	3.3790	0.0639	2.000	1.4483	0.1167	2.000	4.1143	0.0629	2.000	1.0798	0.2177	2.0000	2.8753	0.1340	2.000	1.4590	0.1336
July	WD	2.5125	6.2834	0.0453	1.8042	2.1176	0.1294	2.5944	7.0754	0.0375	2.0939	1.6823	0.1659	2.0412	4.0798	0.0453	2.6047	2.2152	0.0725
	IWD	1.1490	3.1454	0.0837	1.3756	1.5461	0.1063	0.9914	3.0676	0.0816	1.5833	1.1814	0.1477	1.1490	3.1454	0.0837	1.2783	1.3162	0.1720
	RD	2.0000	4.3024	0.0864	2.000	1.5390	0.1210	2.000	4.8267	0.0756	2.000	1.1535	0.2202	2.0000	4.3024	0.0864	2.000	1.5039	0.1897
August	WD	2.6025	6.9199	0.0353	1.9255	2.0917	0.1211	2.7271	7.7120	0.0349	2.3836	1.6882	0.1506	2.2751	4.7470	0.0537	2.3304	2.0004	0.0934
	IWD	1.1677	3.4542	0.0732	1.5350	1.6011	0.1116	0.9470	3.5991	0.0743	1.5166	1.2609	0.1452	0.8318	2.0100	0.1113	1.3071	1.2458	0.1523
	RD	2.0000	4.7124	0.0734	2.000	1.4928	0.1171	2.000	5.2297	0.0702	2.000	1.1575	0.2093	2.0000	3.2934	0.1062	2.000	1.3751	0.1750
September	WD	1.8575	5.3794	0.0542	1.7849	1.7416	0.1427	2.0247	5.8461	0.0336	2.3544	1.5084	0.1599	2.0404	4.0454	0.0615	2.2881	1.8204	0.0722
	IWD	1.0928	2.8811	0.0678	1.4073	1.4738	0.1509	0.8056	2.7155	0.0683	1.5706	1.1682	0.1547	0.8435	1.7806	0.1060	1.1278	1.1483	0.1646
	RD	2.0000	3.8617	0.0833	2.000	1.2716	0.1211	2.000	4.1237	0.0608	2.000	1.0351	0.2196	2.0000	2.8505	0.1115	2.000	1.2556	0.1816
October	WD	1.8129	5.8586	0.0479	1.9550	1.6481	0.1177	2.0730	7.2087	0.0353	2.2958	1.6051	0.1568	1.7396	4.7091	0.0459	2.3304	1.5460	0.0683
	IWD	1.1690	3.5906	0.0580	1.4277	1.4271	0.1419	1.1342	3.9799	0.0519	1.5495	1.2293	0.1313	0.8177	2.2914	0.0726	1.1850	0.9874	0.1680
	RD	2.0000	4.2331	0.0717	2.000	1.1719	0.1245	2.000	5.0678	0.0554	2.000	1.1052	0.1891	2.0000	3.4331	0.0787	2.000	1.0632	0.2048
November	WD	1.4656	3.4498	0.0640	1.6827	1.8591	0.1344	1.6233	5.7244	0.0464	2.0936	1.4494	0.2007	1.5134	5.5136	0.0398	1.8810	1.5050	0.0939
	IWD	1.1569	2.9564	0.0755	1.3118	1.7153	0.1580	1.1590	3.7346	0.0485	1.4843	1.3278	0.2201	0.8072	2.9672	0.0507	0.9168	0.9942	0.1740
	RD	2.0000	2.7327	0.0704	2.000	1.3879	0.1094	2.000	4.2814	0.0623	2.000	1.0139	0.1977	2.0000	4.2350	0.0531	2.000	1.0814	0.1301
December	WD	1.2553	4.0254	0.0945	1.5851	2.0589	0.1222	1.9482	6.8862	0.0365	2.1847	1.5250	0.1879	1.1198	3.7053	0.0597	1.9703	1.6487	0.0893
	IWD	1.0727	2.9619	0.0977	1.2511	1.8612	0.1408	1.0950	4.0143	0.0408	1.5062	1.2830	0.1824	0.8141	2.4122	0.0713	1.1334	1.1267	0.1112
	RD	2.0000	3.3966	0.1185	2.000	1.5742	0.1079	2.000	4.8969	0.0508	2.000	1.0584	0.1977	2.0000	3.2546	0.1087	2.000	1.1699	0.1371

Table 3. The results of comparative seasonal analysis of six regions using WD, IWD and RD

		Bandırma			Sakarya			Bozcaada		
Years	**Methods**	**k**	**c**	**RMSE**	**k**	**c**	**RMSE**	**k**	**c**	**RMSE**
Winter	WD	1.4113	3.9266	0.0490	1.7849	2.4241	0.0773	1.7735	6.5834	0.0192
	IWD	1.0441	3.3531	0.0575	1.1231	1.8980	0.0759	0.8758	4.0794	0.0321
	RD	2.0000	3.1500	0.0586	2.0000	1.7674	0.0805	2.0000	4.7969	0.0364
Spring	WD	1.4923	3.6876	0.0375	2.0330	1.9842	0.0781	1.7500	4.9851	0.0201
	IWD	1.0247	3.5010	0.0558	1.3079	1.7188	0.0996	0.7914	3.0610	0.0462
	RD	2.0000	2.8972	0.0425	2.0000	1.3977	0.1007	2.0000	3.6484	0.0427
Summer	WD	2.0652	5.9418	0.0306	1.9877	1.8021	0.1177	2.1758	6.8172	0.0250
	IWD	1.1310	3.3237	0.0528	1.3756	1.5461	0.1351	0.7948	2.9871	0.0641
	RD	2.0000	4.1763	0.0636	2.0000	1.2762	0.1333	2.0000	4.7532	0.0595
Autumn	WD	1.6017	4.8877	0.0398	1.8630	1.7863	0.0981	1.8516	6.2764	0.0233
	IWD	1.0411	3.4317	0.0435	1.3118	1.7153	0.1384	0.7867	3.2689	0.0442
	RD	2.0000	3.6696	0.0631	2.0000	1.2872	0.0933	2.0000	4.5157	0.0457

Years		Yalova			Gökçeada			Bilecik		
	Methods	**k**	**c**	**RMSE**	**k**	**c**	**RMSE**	**k**	**c**	**RMSE**
Winter	WD	2.1817	1.8227	0.1123	1.2276	4.7335	0.0328	1.7828	1.8118	0.0745
	IWD	1.2558	1.3670	0.1153	0.7885	3.2038	0.0407	1.0384	1.5177	0.0973
	RD	2.000	1.2660	0.1514	2.0000	3.9763	0.0648	2.000	1.3222	0.0939
Spring	WD	2.3103	1.6026	0.1227	1.4162	4.5515	0.0317	1.9833	1.9267	0.0511
	IWD	1.4690	1.3528	0.1338	0.7968	2.8871	0.0419	1.0481	1.4708	0.0978
	RD	2.000	1.1022	0.1684	2.0000	3.5706	0.0596	2.000	1.3651	0.1050
Summer	WD	2.4038	1.6524	0.1494	1.8835	4.2572	0.0526	2.3310	2.1039	0.0541
	IWD	1.5007	1.2856	0.1418	0.8177	2.2732	0.0808	1.2414	1.4124	0.1192
	RD	2.000	1.1313	0.2014	2.0000	3.0452	0.0944	2.000	1.4469	0.1497
Autumn	WD	2.2305	1.5224	0.1445	1.6613	4.6731	0.0207	2.1075	1.6247	0.0489
	IWD	1.4516	1.3792	0.1692	0.7950	2.9146	0.0517	0.9098	1.0730	0.1692
	RD	2.000	1.0527	0.1705	2.0000	3.4659	0.0547	2.000	1.1361	0.1464

-Two-parameter WD function calculated for the investigated locations is more suitable than IWD and RD function according to RMSE controls.

-The RD is not suitable method for six regions that are located in the Northwest of Turkey, Marmara region.

As a result, it is considered that IWD and two-parameter WD are generally more suitable methods than RD for modelling the wind speed of the Marmara region.

Peer-review: Externally peer-reviewed.

Conflict of Interest: The authors have no conflicts of interest to declare.

Financial Disclosure: The authors declared that the study has received no financial support.

References

1. H. Saleh, A.A.E.A. Aly, S. Abdel-Hady, "Assessment of different methods used to estimate Weibull distribution parameters for wind speed in Zafarana wind farm, Suez Gulf, Egypt", Energy, vol. 44, pp. 710-719, 2012. [CrossRef]
2. M. Gökçek, H.H. Erdem, A. Bayülken, "A techno-economical evaluation for installation of suitable wind energy plants in Western Marmara, Turkey", Energy Exploration & Exploitation, vol. 25, pp. 407-427, 2007. [CrossRef]
3. M. Bassyouni, S.A. Gutub, U. Javaid, M. Awais, S. Rehman, S.S. Hamid, M.H. Abdel-Aziz, A. Abouel-Kasem, H. "Shafeek Assessment and analysis of wind power resource using weibull parameters", Energy Exploration & Exploitation, vol. 33, pp.105-122, 2015. [CrossRef]
4. J. Yingni, Y. Xiuling, C. Xiaojun, P. Xiaoyun, "Wind potential assessment using the Weibull model at the Inner Mongolia of China" Energy Exploration and Exploitation, vol. 24, pp. 211-221, 2006. [CrossRef]
5. H. Yue, G. Li and M. Zhou, "A probabilistic approach to small signal stability analysis of power systems with correlated wind sources", Journal of Electrical Engineering and Technology, vol. 8, pp. 1605-1614, 2013. [CrossRef]
6. A. Garcia, J.L. Torres, E. Prieto, A. De Francisco, "Fitting wind speed distributions: a case study", Solar Energy, vol. 62, pp. 139-144, 1998. [CrossRef]
7. R.E. Luna, H.W. Church, "Estimation of long-term concentrations using a "universal" wind speed distribution" Journal of Applied Meteorology, vol. 13, pp. 910-916, 1974. [CrossRef]
8. C.G. Justus, W.R. Hargraves, A. Yalcin, "Nationwide assessment of potential output from wind-powered generators", Journal of Applied Meteorology, vol. 15, pp. 673-678, 1976. [CrossRef]
9. P. Kiss, I.M. Jánosi, "Comprehensive empirical analysis of ERA-40 surface wind speed distribution over Europe", Energy Conversion and Management, vol. 49, pp. 2142-2151, 2008. [CrossRef]
10. W.E. Bardsley, "Note on the use of the inverse Gaussian distribution for wind energy applications", Journal of Applied Meteorology", vol. 19, pp.1126-1130, 1980. [CrossRef]
11. R.M. Vogel, T.A. McMahon, F.H. Chiew, "Floodflow frequency model selection in Australia", Journal of Hydrology, vol. 146, pp. 421-449, 1993. [CrossRef]
12. N.B. Guttman, J.R.M. Hosking, J.R. Wallis, "Regional precipitation quantile values for the continental United States computed from L-moments", Journal of Climate, vol. 6, pp. 2326-2340, 1993. [CrossRef]
13. J.R. Stedinger, "Fitting log normal distributions to hydrologic data" Water Resources Research, vol. 16, pp. 481-490, 1980. [CrossRef]
14. F.C. Kaminsky "Four probability densities/log-normal, gamma, Weibull, and Rayleigh/and their application to modelling average hourly wind speed", In International Solar Energy Society Annual Meeting, vol. 19, 1977, pp.6-10.
15. R.H. Sherlock, "Analyzing winds for frequency and duration" In on Atmospheric Pollution. American Meteorological Society, pp. 42-49, 1951.
16. E.C. Morgan, M. Lackner, R.M. Vogel, L.G. Baise, "Probability distributions for offshore wind speeds", Energy Conversion and Management, vol. 52, pp. 15-26, 2011. [CrossRef]
17. E. S. Takle, J. M. Brown, "Note on the use of Weibull statistics to characterize wind-speed data", Journal of Applied Meteorology, vol. 17, pp. 556-559, 1978. [CrossRef]
18. O.A. Jaramillo, M.A. Borja, "Wind speed analysis in La Ventosa, Mexico: a bimodal probability distribution case", Renewable Energy, vol. 29, pp. 1613-1630, 2004. [CrossRef]
19. E. Dokur, S. Ceyhan, M. Kurban, "Finsler Geometry for Two-Parameter Weibull Distribution Function", Mathematical Problems in Engineering, vol. 2017, pp. 1-6, 2017. [CrossRef]
20. J.A. Carta, P. Ramirez, S. Velazquez, "A review of wind speed probability distributions used in wind energy analysis: Case studies in the Canary Islands", Renewable and Sustainable Energy Reviews, pp.13, pp. 933-955, 2009.
21. L. Van der Auwera, F. De Meyer, L.M. Malet "The use of the Weibull three-parameter model for estimating mean wind power densities", Journal of Applied Meteorology, vol. 19, pp. 819-825, 1980. [CrossRef]
22. F.G. Akgül, B. Şenoğlu, T. Arslan, "An alternative distribution to Weibull for modeling the wind speed data: Inverse Weibull distribution", Energy Conversion and Management, vol. 114, pp. 234-240, 2016. [CrossRef]
23. M. Carrasco-Díaz, D. Rivas, M. Orozco-Contreras, O. Sánchez-Montante, "An assessment of wind power potential along the coast of Tamaulipas, northeastern Mexico", Renewable Energy vol. 78, pp. 295-305, 2015. [CrossRef]
24. J.F. Manwell, J.G. McGowan, A.L. Rogers "Wind energy explained: theory, design and application" John Wiley & Sons, 2010.
25. S. Mathew "Wind energy: fundamentals, resource analysis and economics", Heidelberg: Springer, vol. 1, 2006. [CrossRef]
26. C.G. Justus, W.R. Hargraves, A. Mikhail, D. Graber, "Methods for estimating wind speed frequency distributions", Journal of Applied Meteorology, vol. 17, pp. 350-353, 1978. [CrossRef]
27. S.A. Akdag, A. Dinler, "A new method to estimate Weibull parameters for wind energy applications", Energy Conversion and Management, vol. 50, pp. 1761-1766, 2009. [CrossRef]
28. M. Kurban, E. Dokur, S. Ceyhan. "A novel information geometry method for estimating parameters of the Weibull wind speed distribution." Proceedings of the Estonian Academy of Sciences vol. 67, pp. 39-49, 2018. [CrossRef]
29. E.H. Lysen "Introduction to wind energy", Consultancy services wind energy developing countries (CWD), 1982.
30. M.J.M. Stevens, P.T. Smulders, "The estimation of the parameters of the Weibull wind speed distribution for wind energy utilization purposes", Wind engineering vol. 3, pp. 132-145, 1979.

Emrah Dokur received the B.Sc. in Electrical and Electronics Engineering, Istanbul University, Turkey in 2010 and M.Sc. degrees in Electrical Engineering, Istanbul Technical University, Turkey in 2013. He received the Ph.D. degree at Energy System Engineering in Bilecik S.E. University. Since 2017, he has been assistant professor in the same University. His research areas include high voltage engineering, renewable energy systems, and power system analysis.

Salim Ceyhan received the B.Sc. M.Sc. and Ph.D. degrees in Mathematical Engineering at Istanbul Technical University (ITU) in 1987, 1991 and 1994, respectively. Since 2011, he has been assistant professor in the Bilecik S.E. University. His research areas include applied mathematics, differential geometry, and metric spaces.

Mehmet Kurban graduated from Istanbul Technical University (ITU) in Turkey as an Electrical Engineer from Faculty of Electrical and Electronics Engineering in 1991. He got M. Sc and Ph.D. degree from ITU in 1994 and 2001, respectively. Since 2015, he has been professor in the Bilecik S.E. University. His research areas include renewable energy and power system analysis.

İSTANBUL UNIVERSITY
CERRAHPAŞA

RESEARCH ARTICLE
Electrica 2019; 19(1): 29-36

Enhanced SPIHT Algorithm with Pipelined Datapath Architecture Design

Serap Çekli, Ali Akman

Department of Computer Engineering, Maltepe University, Istanbul, Turkey

Cite this article as: Çekli S, Akman A. Enhanced SPIHT Algorithm with Pipelined Datapath Architecture Design. *Electrica*, 2019; 19(1): 29-36.

ABSTRACT

Set partitioning in hierarchical trees (SPIHT) is an efficient algorithm which is used for the image compression widely. SPIHT operates sequentially so, its parallel implementation is difficult. In this study, the SPIHT algorithm is improved for providing that it is suitable for the parallel processing applications, and the corresponding pipelined datapath is designed for the proposed enhanced SPIHT algorithm. The datapath is designed to have three stages as preprocessing, list generation and output stream. In the preprocessing stage, the flags which are supports the list generation stage are constituted. List of insignificant sets (LIS), list of insignificant pixels (LIP) and list of significant pixels (LSP) are formed in list generation stage. These lists contain the bit values which generate the output bit stream. The performance of the improved datapath design has been tested by compressing different images, and the obtained results are given.
Keywords: SPIHT, enhanced SPIHT, image compression, pipelined datapath

Introduction

The images require large storage capacity and high transmission bandwidth resulting from including considerable information. The compression operation which provides to eliminate the redundant information is advantageous for many aspects such as storage capacity, transmission speed.

Therefore, several studies have been fulfilled for the image compression, and still much efforts continue to improve the compression performance from some different aspects. Some of these studies have been focused on wavelet transform which provides the multi resolution analysis, based compression algorithms such as embedded zero tree wavelet (EZW), set partitioning in hierarchical trees (SPIHT), optimal truncated embedded block coding (EBCOT) used in JPEG2000 standard [1-3].

Set partitioning in hierarchical trees is a discrete wavelet transform (DWT) based, efficient, adaptive and computationally fast compression algorithm [2]. This algorithm is known as an enhanced implementation of the EZW algorithm which has improved performance, which provides embedded coding output. The algorithm provides satisfactory PSNR (peak signal to noise ratio) values, effective image quality and compression ratio, and fast processing time. It can be used for the lossy or lossless data compression according to the necessary application. By means of the mentioned advantages, SPIHT is a suitable option for image compression applications especially for small devices with limited power consumption and memory capacity [4, 5].

Until today, some studies have been performed to increase the performance of the SPIHT coders, and many researches are carried on in this field yet. Several studies which have been fulfilled have aimed at providing improvement of the compression performance [6], reduction of the memory requirement [4, 5, 7, 8], decrease of the output coding time [9-12], to provide efficient hardware resource usage [13, 14], security of the SPIHT algorithm [15, 16] or biomedical applications [17].

Corresponding Author:
Serap Çekli

E-mail:
serapcekli@maltepe.edu.tr

Received: 03.08.2018

Accepted: 27.08.2018

DOI: 10.26650/electrica.2018.15101

The use of breadth first search (BFS) procedure is a suitable option while implementing the architectural design of SPIHT algorithm to examine the SOTs. At first, BFS deals with the examination of neighboring pixels in the same level. By this means, extra register necessity is eliminated when the inspection is carried out for the decision process on a tree, and also parallel processing architecture could be designed.

The rest of the study can be summarized as follows; The SPIHT algorithm and the system architecture are described after the underlying concepts of the SPIHT algorithm are given. Then, the obtained results have been presented and discussed. As the last, the conclusion section is given.

SPIHT algorithm

In the SPIHT algorithm, the image is divided into quadtree structure repeatedly by calculating the DWT coefficients. In the algorithm, the values or positions of the pixels in the subbands are not transmitted. Instead, the decision points that define the structural properties of the image in the tree structure and the results of the decisions at these points are coded as output. Since the positions of the decision points in the tree structure and the output values are known, the image can be recovered in the decoder.

The SPIHT algorithm is consists of three steps which are initialization, sorting pass, and refinement pass. The algorithm uses three types of list structures for memory operations: LIS; list of insignificant sets, LIP; list of insignificant pixels, and LSP; list of significant pixels. A threshold value is determined considering the maximum coefficient value at the initialization step. Significant coefficients in LIP and LIS are determined at the sorting pass. For a value of n, a C_{ij} coefficient is significant if satisfies the condition $|C_{ij}|\geq 2^n$, otherwise it is insignificant. The significance test is applied to coefficients by arranging as sets, and the sets are partitioned by spatial orientation trees (SOTs). The SOTs are given in Figure 1.

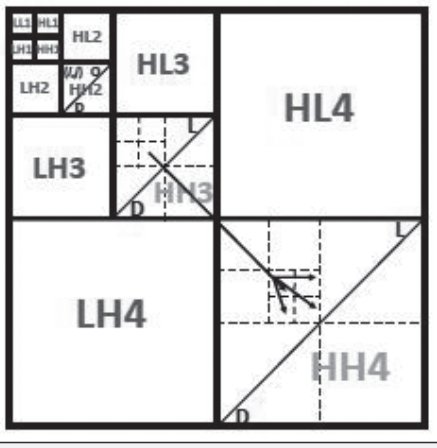

Figure 1. The spatial orientation trees of SPIHT algorithm, and subbands

Each pixel has four offspring except for the upper left pixel. $O(i,j)$: Defines the set of the coordinates of the four offspring of a pixel at the (i,j).

• $D(i,j)$: The set of all descendants of a position (i,j).

• $H(i,j)$: The set including the coordinates of the roots of all SOTs.

• $L(i,j)$: The set of the coordinates of all descendants excluding offspring of a position (i,j), and given as $D(i,j) - O(i,j)$.

The entries in the lists are determined by a (i,j) coordinate. These coordinates represent the individual pixels in LIP and LSP, and also an A type entry of the set $D(i,j)$ or a B type entry of the set $L(i,j)$.

The significance test applied to a given set of is defined in the following equation;

$$S_n(T) = \begin{cases} 1, & max_{(i,j)\in T}|c_{i,j}| \geq 2^n \\ 0, & \text{otherwise} \end{cases}, \quad (1)$$

Enhanced SPIHT algorithm

One of the main obstacles to design of the high performance digital system of the SPIHT compression algorithm is difficulty of the parallel implementation resulting from use of lists obtained in one step of algorithm in the next step. In this study, a novel algorithm which reconfigures the constitution of LIP and LIS is proposed to eliminate this drawback, and the outline of the proposed algorithm is given in the Figure 2. The algorithm performs list constitution based on BFS in quadtree structure.

In the step of construction of LIP and LIS, the constitution of LIP and LIS for the corresponding threshold value is fulfilled. The dependency between consecutive threshold values is removed because the constitution of these lists are repeated again for each new threshold value. Construction of LIP and LIS starts with four coefficients located at the lowest frequency band of wavelet transform coefficient matrix. Coefficient coordinates not in LSP are inserted in LIP. Other entries of LIP are obtained while the construction of LIS.

LIS is obtained by testing in sequence the roots of three subtrees. The root (i,j) of subtree is inserted to LIS. The offspring $(O(i,j))$ of that coordinate not in LSP is inserted to LIP, if the result of significance test of all descendants of (i,j) coordinate is $Sn(D(i,j))=1$. After that, significance test of all descendants excluding offspring of (i,j) coordinate is performed.

If $Sn(L(i,j))=1$ then (i, j) subtree is tested using BFS. In this test, if significance test of all descendant excluding offspring of the parent pixel of a (k,l) coordinate in subtree is $Sn(L(parent(k,l)))=1$, this (k,l) coordinate is added to LIS. If the significance test of all descendant of that (k,l) coordinate is $Sn(D(k,l))=1$, then offspring $(O(k,l))$ not in LSP are added to LIP. Thus, test continues on the other subtree upon completion of scanning entire subtree.

Step1. *Initialization:* $n = \lfloor log_2 max_{i,j}(c_{i,j}) \rfloor$ is transmitted. LSP is constructed as an empty list.

Step2. *Construction of LIP ve LIS:*

LIP and LIS lists are constructed as empty sets.

Each $(i,j) \in H$ and $(i,j) \notin$ LSP pixels are added to

For each $(i,j) \in H$

If $(i,j) \neq (0,0)$ then (i,j) is added to LIS.

If $S_n(D(i,j)) = 1$ then

Each $(k,l) \in O(i,j)$ and $(k,l) \notin$ LSP pixels are added to LIP.

If $S_n(L(i,j)) = 1$ then

BFS(i,j) set is constructed from set $D(i,j)$ by breadth first search.

For each $(k,l) \in$ BFS(i,j)

If $S_n(L(parent(k,l))) = 1$ then

(k,l) is added to LIS.

If $O(i,j) \neq \emptyset$ and $S_n(D(i,j)) = 1$

Each $(p,r) \in O(k,l)$ and $(p,r) \notin$ LSP pixels are added to LIP.

Step3. *LIS output stream:*

For each $(i,j) \in$ LIS

If $S_n(D(i,j)) = 1$ then a 1 otherwise a 0 is added to LIS output stream.

If $S_n(L(i,j)) = 1$ then a 1 otherwise a 0 is added to LIS output stream.

Step4. *LIP output stream and LSP set:*

For each $(i,j) \in$ LIP

If $S_n(i,j) = 1$ then

A 1 is added to LIP output stream.

The sign of $c_{i,j}$ is added to LIP output

(i,j) is adde to LSP.

If $S_n(i,j) = 0$ then a 0 is added to LIP output

Step5. *LSP output stream:* For each entry of (i,j) n-th most significant bit of $|c_{i,j}|$ is added to LSP output stream except for entries appended in last sorting pass (for the same n).

Step6. *Output stream:* LIS, LIP and LSP output streams are added to output stream.

Step7. *Quantization step update:* n is decreased 1 and if there is need the process continues from Step2.

Figure 2. Enhanced SPIHT coding algorithm

In LIS output stream, two bits are coded in for significance of all descendant and all descendant excluding offspring for each coefficient. Each coefficient in LIP is subjected to significance test. If the result of significance test for coefficient is 1, a 1 and sign of coefficient is added to LIP output stream. This coefficient coordinate is added to LSP. Otherwise, 0 is coded to LIP output stream. LIP output stream and LSP are completed by this manner. The LSP output stream is similar to the refinement pass in the original algorithm. The threshold value is halved and the process continues by the construction of the new LIP and LIS. The enhanced SPIHT coding algorithm is given in Figure 2.

Proposed SPIHT architecture

The architectural design of the enhanced SPIHT algorithm is described in this section. This architectural design has been performed in pipelined datapath form. The system flow diagram of the designed architecture is given in Figure 3.

The block diagram of the proposed SPIHT architecture is given in Figure 4. The architecture is designed in the form of a three stage pipelined architecture corresponding with the system flow in Figure 3. The first stage of the designed architecture is the preprocessing stage. This stage starts with the reading the four successive coefficients from the Main Memory. The transform coefficients are stored in the main memory according to the Morton scanning order from lower addresses to higher addresses. In the preprocessing unit, these coefficients are read in the reverse of the Morton scanning order beginning from

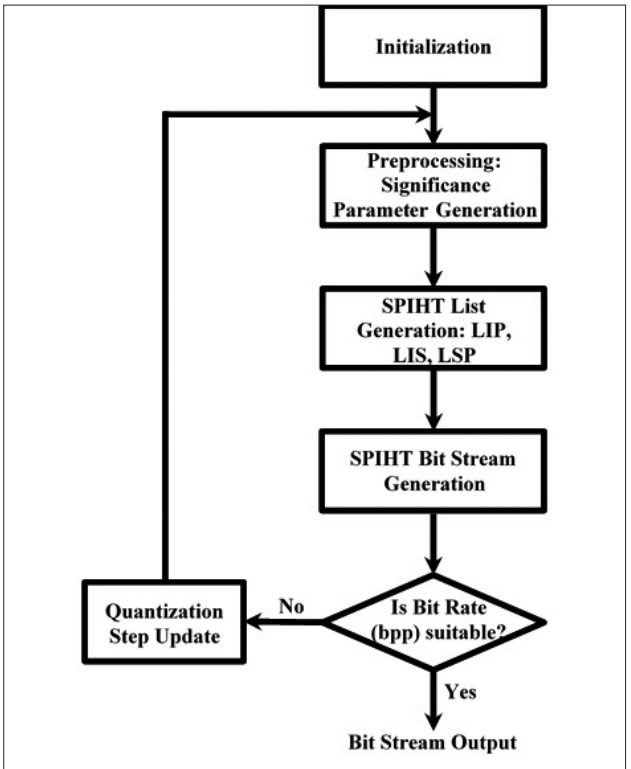

Figure 3. SPIHT encoder flow diagram

higher addresses. In this manner, data gathering starts from the lower right corner of the image, so that it is avoided that examination of the same pixels by visiting same positions.

Performing reading operation of the coefficients in this way provides considerable advantages in the significance tests of all descendants ($D(i,j)$) and all descendants excluding offspring ($L(i,j)$). If a coefficient is significant then all descendants of the parent and also all descendants of grandparent excluding offspring of that coefficient is significant. Since the coefficients in the SPIHT algorithm are arranged according to the quadtree structure, the same situation is also valid for the parent and grandparent of each four coefficients. By this means, reading of four coefficients from the main memory at the same time for the preprocessing stage provides efficiency in execution time. Moreover, four coefficients can be tested in parallel. Coefficient test unit fulfils the determination operation of five flags of a coefficient. These flag bits are defined as the significance of the coefficient, the sign bit if the coefficient is significant, significance of all descendants of the coefficient, the significance of all descendants excluding offspring of the coefficient, and the refinement bit. The flags of four coefficients are stored in the significance flag memory by aligning in accordance with the data structure given in Figure 5.

The flag data of concerned coefficient is read from the significance flags memory to find the significance flag value of all descendants or all descendants excluding offspring for a pixel. This data contains flags which possibly may have been written earlier belonging to offspring while examining offspring of that pixel.

Therefore, that data is necessary to calculate the significance flag of all descendants or all descendants excluding offspring for a coefficient. If the significance flag of a coefficient is 1, this situation affects the significance flags of all descendants of parent of the coefficient and all descendants excluding offspring of grandparent of the coefficient. Hence, the flag data stored in the significance flags memory of the parent pixels and grandparent pixels should be updated. The related fields of the data structure is updated by taking the flag data of parent pixel from memory, and data is stored to significance flags memory again. The same operation process is repeated for the grandparent pixel.

Another important unit at this stage is significance flags memory. The memory structure shown in Figure 6 also acts as pipeline register between pipeline stages since enhanced SPIHT encoder is designed to conform to pipelined datapath architecture. This designed memory structure is consisting of two individual memory unit, essentially. The use of data calculated in previous stage is made possible in the second stage while significance flag data is created in the first stage.

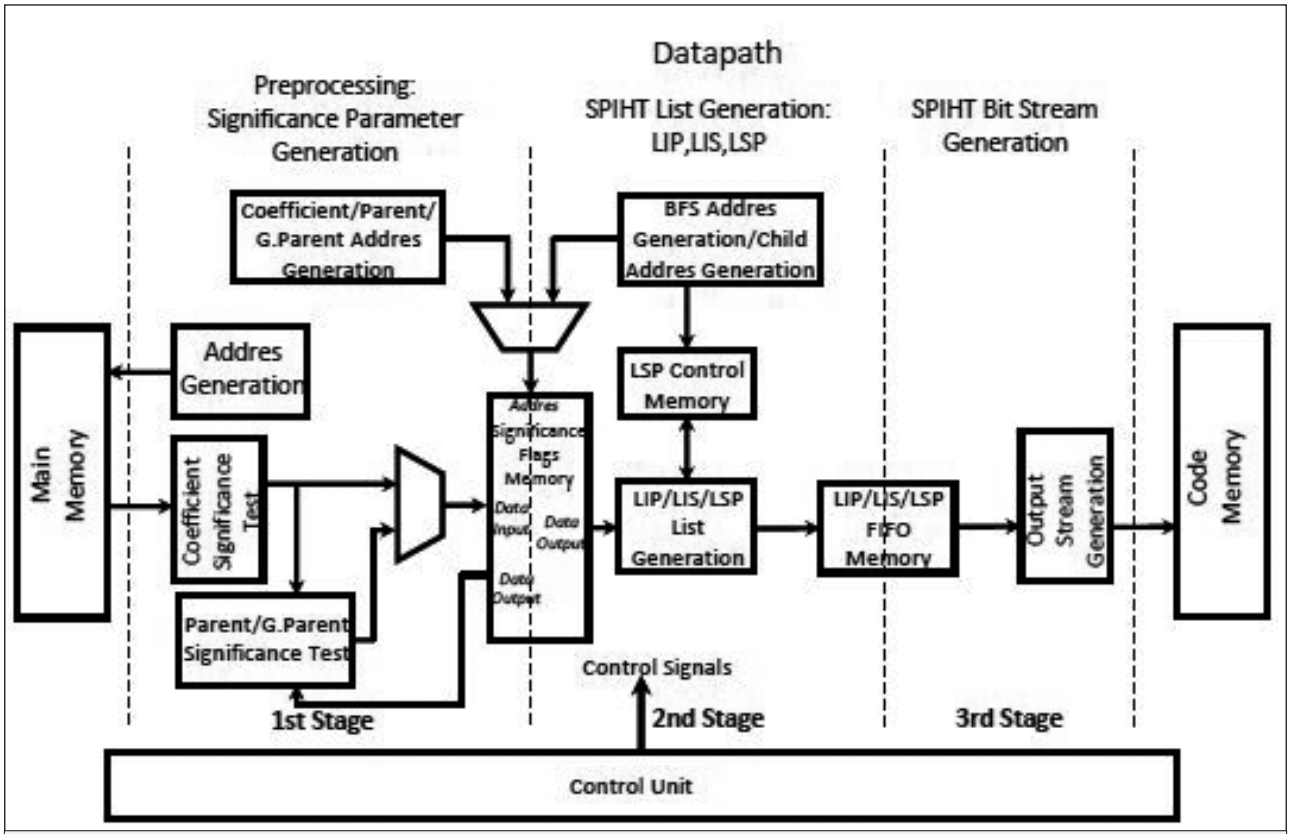

Figure 4. SPIHT encoder architecture

The second stage of the proposed architecture is generation of SPIHT Lists. Lists are constructed using flags generated in the first stage. Because of the quadtree structure and the fact that the flags are structured in quadtree form at first stage, the coefficients are also processed as quadtree form at this stage.

Initially, the flags of the first four coefficients are read. The second, third and fourth coefficients of the first four coefficients are the roots of quadtrees. Each quadtree is processed in parallel.

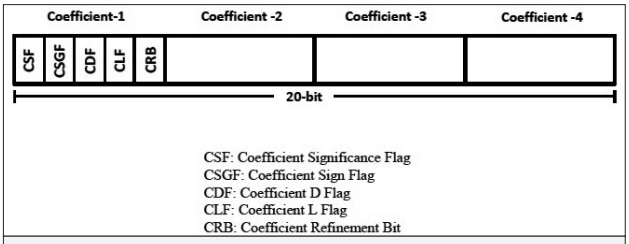

Figure 5. The data structure of coefficient significance flags

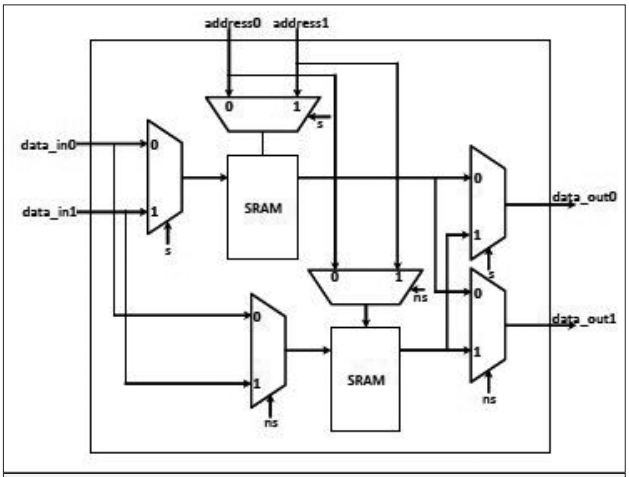

Figure 6. Design of significance flags memory (ns → ~s)

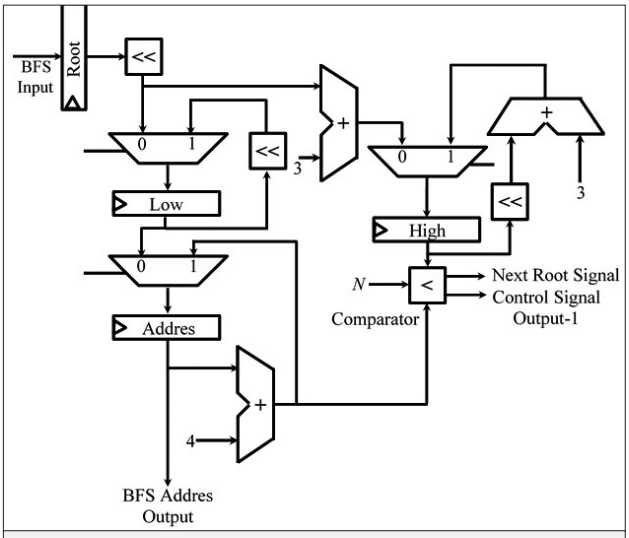

Figure 7. Design of BFS address generator

LIP, LIS and LSP are generated in FIFO (first in first out) memory structure. The size of lists is determined depending on image size and are not altered later. Some fields may stay empty in lists because all coefficients may not enter into these lists in an encoding stage. A 1-bit data, v-bit, is used to discriminate the empty and used fields. If this bit is 1, then this means that this field is used, and next bits will be coded in the output stream. There is a two-bit data field in LIP for each coefficient which enters this list except for the v-bit. These fields are the coefficient significance flag (CSF) and coefficient sign flag (CSGF). Two fields are defined in the LIS except for the v-bit. These fields are CDF and CLF bits. The CRB bit is existed in LSP except for the v-bit.

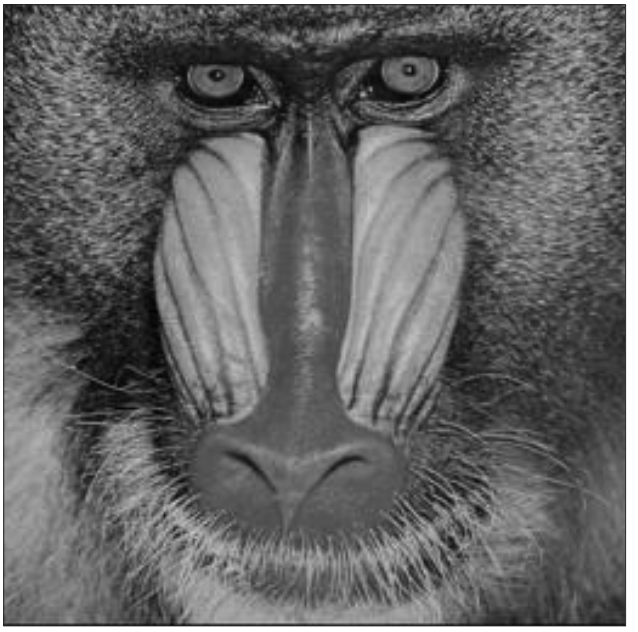

Figure 8. Test images

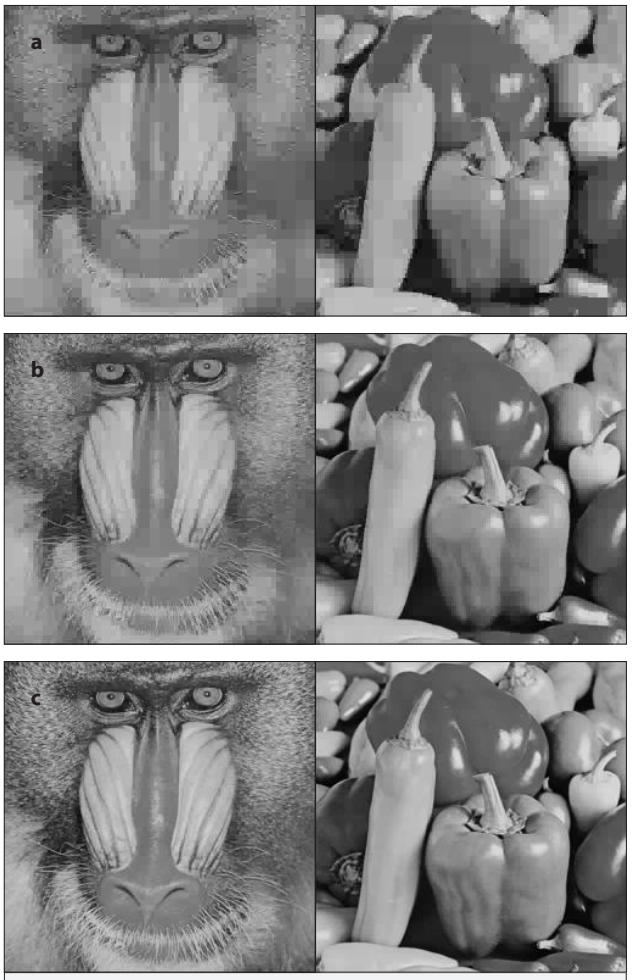

Figure 9. a-c. Reconstructed images for different bit rates. Reconstructed images for 0.035 bpp (a). Reconstructed images for 0.12 bpp (b). Reconstructed images for 0.44 bpp (c)

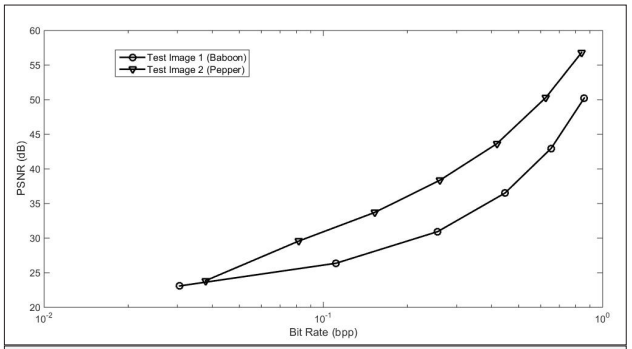

Figure 10. The variation of PSNR values with bit rate of the reconstructed images

Besides other list memories, another memory (LSP check) else is used to indicate which coefficient is inserted into LSP. The size of this memory is *NxN* bits. In LSP check memory, corresponding Morton order number bit of this coefficient is set as 1 when a coefficient enters into LSP. LIP and LIS memories are reseted at beginning of each quantization step. LSP and LSP check memories are used during the encoding without cleared. In other words, the entries in a quantization step are added following the entries of previous step. The memory structures of these lists are designed in complying with the memory structure used in the first stage and given in Figure 6.

Since the coefficients are processed using BFS in this stage the BFS address generator block given in Figure 7 is crucial.

Three registers are used in the design. Address of the coefficient at the root of the tree which will be scanned initially is recorded to the first register. The addresses of the coefficients on the left and right sides of these levels are recorded in the Low and High registers as the sublevels in the tree are examined by. The address scan starts from the Low register and continues to until the reach of the value in the High register. When the High register value is reached, the register values are updated according to the new level by descending one level down in the tree.

The third stage is the output stream stage. In the second step, list data stored in FIFO memory is transmitted to the output stream. Firstly, LIS FIFO memory, secondly LIP FIFO memory, and finally LSP FIFO memory contents are transmitted to the output stream.

Results

The designed SPIHT datapath has been tested using different images with 256×256 pixels. The wavelet coefficients of images at this size can be expressed by a 16-bit sign-magnitude representation.

First of all, the memory analysis necessary for encoding the images used in the tests has been performed. Since the coefficients and the output stream are stored in main memory, the memory space used for this data is not included in the analysis. Two types of memory have been used in the SPIHT datapath: The registers used for the intermediate operations, and SRAM between pipeline stages memories (significance flags memory and list memories). The analysis is performed for SRAM memory elements, since the memory space used for the registers is negligible as compared to the other memory space.

In significance flags memory, a 20-bit field is used for each of the four coefficients. Therefore, the total memory space used;

$$Significance\ Flags\ Memory\ Space = (2N^2/4)\times 20bit \quad (2)$$

If *N*=256 then this value is 80 Kbyte. The contents of LIP and LIS memories change at every calculation step. The size of the list memories has been determined by taking into account the maximum list size obtained in the tests performed and fixed for each calculation step. The number of coefficients entering the LIS increases as the threshold value decreases. The number of coefficients have the maximum value when the threshold value is equal to 1, and all the coefficients enter into this list except for the first one.

$$LIS\ Memory = 2(N^2 - 1) \times 3bit \quad (3)$$

If *N*=256 then this value is 48 Kbyte. The number of coefficients entering LIP memory has been determined by conducting different trials. As a result of the different trials, it has been concluded that the maximum size of LIP changes from 45% to 65% of number of coefficients. The size of the memory has been determined as given follows ensuring that not to overflow the memory.

$$LIP\ Memory = 2(0.75N^2) \times 3bit \quad (4)$$

If *N*=256 then this value is 36 Kbyte. LSP memory and LSP check memory contains all the coefficients, so the total LSP memory is given as;

$$LSP\ Memory = N^2 \times 3bit \quad (5)$$

If *N*=256 then this value is 24 Kbyte. Total memory space is 188 Kbyte if *N*=256.

The images used in the trials are given in Figure 8. The simulation of the design has been performed by storing the wavelet transform coefficients of these images to main memory. The output bitstreams for the different bit rates are also has been stored in the main memory. The images have been recovered by decoding the output bit streams in the decoder. The recovered images are shown in Figure 9. The PSNR criterion has been used to measure the similarity of the reconstructed images with the original image. The variation of PSNR values with bit rate of the reconstructed images is given in Figure 10.

Conclusion

In this study, the SPIHT image compression algorithm has been improved providing that the more compatible with hardware design process. The pipelined datapath design of the proposed enhanced SPIHT algorithm has been also performed. This datapath is comprised of three stages as preprocessing, list generation and output stream. As distinct from present studies, taking the coefficients in reverse Morton order avoids the unnecessary repeated operations for significance tests of all descendants and all descendants excluding offspring, in preprocessing stage. In list generation stage, the BFS has been considered, and a BFS address generator has been designed. The designed datapath has been tested by using different images. According to these tests, memory analysis of the datapath has been fulfilled and the obtained compression results has been given. The proposed method can be used for fast and less complex calculation required image compression systems in which low power and low capacity devices.

Peer-review: Externally peer-reviewed.

Conflict of Interest: The authors have no conflicts of interest to declare.

Financial Disclosure: The authors declared that this study has received no financial support.

References

1. J. M. Shapiro, "Embedded Image Coding Using Zerotrees of Wavelet Coefficients", IEEE Trans Sig Proc, vol. 41, no. 12, pp. 3445-3462, 1993. [CrossRef]
2. A. Said, A.P. William, "A New, Fast, and Efficient Image Codec Based on Set Partitioning in Hierarchical Trees", IEEE Trans Circ Sys V Tech, vol.6, no.3, pp.243-250, 1996. [CrossRef]
3. D. Taubman, "High Performance Scalable Image Compression with EBCOT", IEEE Trans Im Proc, vol.9, no.7, pp.1158-1170, 2000. [CrossRef]
4. M. Akter, M. B. Reaz, F. Mohd-Yasin, F. Choong, "A Modified-Set Partitioning in Hierarchical Trees Algorithm for Real-Time Image Compression", Jour Com Tech Elec, vol. 53, no.6, pp. 642-650, 2008. [CrossRef]
5. Z. E. Hanaa, A. E. Mostafa, A. A. Hesham, "A Modified Listless Strip Based SPIHT for Wireless Multimedia Sensor Networks", Elsevier Comp Elec Eng, vol. 56, pp. 519-532, 2016. [CrossRef]
6. N. R. Rema, A. O. Binu, P. Mythili, "Image Compression Using SPIHT with Modified Spatial Orientation Trees", Elsevier Proce Comp Sci, vol. 46, pp.1732-1738, 2015. [CrossRef]
7. Y. Sun, H. Zhang, G. Hu, "Real-Time Implementation of a New Low-Memory SPIHT Image Coding Algorithm Using DSP Chip", IEEE Trans Im Proc, vol. 11, no. 9, pp. 1112-1116, 2002. [CrossRef]
8. L. W. Chew, L. M. Ang, K. P. Seng, "New Virtual SPIHT Tree Structures for Very Low Memory Strip-Based Image Compression", IEEE Sig Proc Lett, vol. 15, pp. 389-392, 2008. [CrossRef]
9. Y. Jin, H. J. Lee, "A Block-Based Pass-Parallel SPIHT Algorithm", IEEE Trans Circ Syst V Tech, vol. 22, no. 7, pp.1064-1075, 2012. [CrossRef]
10. H. J. O. Dominguez, O. O. V. Villegas, V. G. C. Sanchez, "Modified Set Partitioning in Hierarchical Trees Algorithm Based on Hierarchical Subbands", Jour Elec Im, vol. 24, no. 3, pp.1-12, 2015.
11. S. Cekli, A. Akman, "An Efficient SPIHT Algorithm and System Architecture for Image Compression", Sig Proc Com App Conf (SIU), 15-18 May, Turkey, 2017. [CrossRef]
12. J. H. Hsieh, R. C. Lee, K. C. Hung, M. J. Shih, "Rapid and Coding-Efficient SPIHT Algorithm for Wavelet-Based ECG Data Compression", Elsevier Int, VLSI Jou, vol. 60, pp. 248-256, 2018. [CrossRef]
13. T. W. Fry, S. A. Hauck," SPIHT Image Compression on FPGA", IEEE Trans Circ Syst V Tech, vol.15, no. 9, pp.1138-1147, 2005. [CrossRef]
14. S. Kim, D. Lee, J. S. Kim, H. J. Lee, "A High-Throughput Hardware Design of a One-Dimensional SPIHT Algorithm", IEEE Trans Multimedia, vol. 18, no. 3, pp. 392-404, 2016. [CrossRef]
15. T. Hadjem, M. S. Azzaz, C. Tanougast, S. Sadoudi, "A New Image Crypto-Compression System SPIHT-PSCS", Int Conf Cont, Dec Inf Tech (CoDIT), 3-5 November, France, 2014. [CrossRef]
16. M. Zhang, X. Tong, "Joint Image Encryption and Compression Scheme Based on IWT and SPIHT", Elsevier Opt Lasers Eng, vol. 90, pp. 254-274, 2017. [CrossRef]
17. Z. Lu, D. Y. Kim, W. A. Pearlman, "Wavelet Compression of ECG Signals by the Set Partitioning in Hierarchical Trees Algorithm", IEEE Trans Bio Eng, vol. 47, no. 7, pp. 849-856, 2000. [CrossRef]

Serap Çekli was born in Germany in 1978. She received her BSc. degree in Electronics Engineering from Istanbul University in 2000, MSc. degree in Electronics and Communication Eng. from Istanbul Technical University in 2003. She has received PhD. degree from Istanbul University, Elect. Electronics Eng. Dept. in 2009. She worked for Istanbul University Engineering Faculty as a research assistant between2001-2009. She has been working as a asistant professor at Maltepe University, Computer Engineering Department since 2009. Her research interests are digital systems, digital design, computer organization and architecture.

Ali Akman received her BSc., MSc. and PhD. degrees in Electronics Engineering from Uludağ University, Bursa, Turkey in 1993, 1996 and 2004, respectively. He has been working as a asistant professor at Maltepe University, Computer Engineering Department since 2007. Pirior to joining Maltepe University, he worked for Uludağ University, Department of Electronics Engineering as a research assistant and lecturer. His research interests are digital systems, computer architecture, embedded systems, networked embedded systems and wireless sensor networks.

İSTANBUL UNIVERSITY
CERRAHPAŞA

RESEARCH ARTICLE
Electrica 2019; 19(1): 37-47

The Adaptive Chaotic Symbiotic Organisms Search Algorithm Proposal for Optimal Reactive Power Dispatch Problem in Power Systems

Enes Yalçın[1], M. Cengiz Taplamacıoğlu[1], Ertuğrul Çam[2]

[1]Department of Electrical and Electronics Engineering, Gazi University, Ankara, Turkey
[2]Department of Electrical and Electronics Engineering, Kırıkkale University, Kırıkkale, Turkey

Cite this article as: Yalçın E, Taplamacıoğlu MC, Çam E. "The Adaptive Chaotic Symbiotic Organisms Search Algorithm Proposal for Optimal Reactive Power Dispatch Problem in Power Systems", *Electrica*, 2019; 19(1): 37-47.

ABSTRACT

This paper presents an adaptive chaotic symbiotic organisms search algorithm (A-CSOS) for finding the solution of optimal reactive power dispatch (ORPD) problem which is one of the main issues of power system planning and operations. The most important advantage of symbiotic organisms search algorithm (SOS) is that is not need any particular algorithm parameters. However, the SOS algorithm has some features to be enhanced, like falling into local minima and sluggish convergence. A-CSOS algorithm with adding new and improved features like adaptivity and chaos to conventional SOS algorithm is proposed to solve ORPD problem. The ORPD problem is mainly focused on minimization of transmission loss (Ploss) and total voltage deviation (TVD). To determine the optimal set points of control variables including generator bus voltages, tap positions of transformers, and reactive power outputs of shunt VAR compensators is very crucial for minimization to Ploss and TVD. The proposed algorithm is implemented on IEEE 30-bus test power systems for ascertaining the performance of A-CSOS algorithm on ORPD problem. The results showed that the proposed approach is up to 10.39% better than many of which the latest algorithms in literature and encourage the researchers to implement A-CSOS algorithm to ORPD problem.
Keywords: Adaptive chaotic symbiotic organisms search, power loss minimization, reactive power dispatch, symbiotic organisms search, voltage deviation minimization

Introduction

Efforts to find the optimum solution for power system planning and operational problems continue today. One of these problems is the optimal reactive power dispatch (ORPD) problem which is a highly nonlinear and non-convex optimization problem [1]. The ORPD can be defined as an ideal allocation of reactive power in the power system to minimize predefined objective function while satisfying the numerous constraints. Though active power loss (Ploss) is mostly preferred as an objective function to be minimized, minimization of absolute value of total voltage deviation (TVD) and voltage stability index can be used as an objective functions in ORPD studies. Therefore, minimization of Ploss and TVD have been chosen as objective functions in this study. The parameters that are controlled to minimize the objective function are generator bus voltages, tap settings of transformers and reactive power outputs of shunt compensators [2].

Up to now, many algorithms from classical optimization techniques to modern optimization and hybrid algorithms have been used to determine the ideal values of the control parameters. Many different modern optimization techniques such as particle swarm optimization (PSO) [3], differential evalution (DE) [4], biogeography based optimization (BBO) [5], gravitational search algorithm (GSA) [6], artificial bee colony (ABC) [7], firefly algorithm (FA) [7], bacteria foraging optimization algorithm (BFOA) [7], bat algorithm (BA) [8], cuckoo search algorithm (CSA) [8], ant lion optimization (ALO) [9], gray wolf optimization (GWO) [9], teaching learning based optimization (TLBO) [10], whale optimization algorithm (WOA) [11], quasi-oppositional chemical reaction optimization (QOCRO) [12] are being developed and applied to ORPD and other optimization problems. However, these algorithms also have features that can be positive and negative or improved. For this reason, existing algorithms continue to

Corresponding Author:
Enes Yalçın

E-mail:
gaziyalcine@gmail.com

Received: 16.07.2018

Accepted: 26.11.2018

DOI: 10.26650/electrica.2019.18008

be improved either by hybridization with more than one algorithm or by adding various features to the existing algorithm. The comprehensive learning PSO (CLPSO) [3], hybrid particle swarm optimization and gravitational search algorithm (PSOGSA) [6], opposition-based gravitational search algorithm (OGSA) [13], hybrid firefly algorithm (HFA) [7], modified ant lion optimization (MALO) [8], quasi-oppositional teaching learning based optimization (QOTLBO) [10], modified differential evolution (MDE) [14], improved gravitational search algorithm with conditional selection strategies (IGSA-CSS) [15], chaotic improved particle swarm optimization (MOCIPSO) [16], chaotic parallel vector evaluated interactive honey bee mating optimization (CPVEIHBMO) [17], hybrid particle swarm optimization and imperialist competitive algorithm (PSO-ICA) [18] can be given as example of algorithms developed with this approach for solving the ORPD problem. However, most of these modern optimization algorithms contain some parameters that must be determined sensitively and affecting the result significantly.

As a solution to this problem, Symbiotic Organisms Search algorithm (SOS) is introduced [19]. SOS is an algorithm that is inspired by the interaction of the organisms in an ecosystem and does not contain any particular algorithmic parameters. SOS algorithm has been implemented on some power system problems such as economic load dispatch by Guvenc et al. [20], optimal placement of distributed generations in radial distribution systems by Das et al. [21. However, SOS algorithm offers many important advantages but also SOS may suffer from premature convergence that will lead the optimization falling into local optima when it is applied for high dimension large-scale problems. For this reason, some researchers such as Secui [22] and Saha et al. [23] have achieved better results than standard SOS by making some modifications based on the standard SOS. To find a better result in global solution set by improving searching capability and avoid falling into local optima, principle of chaos approach adapted to algorithms. The making some modifications and using hybridization techniques affect positively to performance of originals. However, handling the constraints within limits cannot be assured when using these methods to solve especially complex optimization problems. To find global optimum solution for large-scale problems like ORPD problem, not only to improve the original methods but also to handle constraints have to be required well simultaneously. In many studies, quadratic penalty function is used to overcome all equality and inequality constraints, but this method has some penalty parameters that significantly affect the solution and to be needed a large amount of time to determine the optimal values. In addition to this, static penalty method also has some coefficients that significantly affect the solution and be required time-consuming trial and errors. More recently, adaptive penalty schemes have been introduced with the goal of eliminating above-mentioned problems and evaluating each candidate solution using specific feedback information for every iteration. One of the most promising self-adaptive penalty approach is the Global Competitive Ranking (GCR) method [24].

In this paper, adaptive chaotic symbiotic organisms search algorithm (A-CSOS) is designed by integrating the chaos and adaptive penalty features into SOS. The proposed A-CSOS algorithm is applied to ORPD problem comprising the Ploss and TVD minimization on IEEE 30-bus test power system. Simulations are performed on four different test cases which are Ploss minimization with continuous variables, Ploss minimization with discrete variable transformer taps and shunt compensator outputs, TVD minimization with continuous variables, TVD minimization with discrete variable transformer taps and shunt compensator outputs. Simulation results show that the proposed algorithm gives substantially better result than the best result of many other state-of-art algorithms. Therefore, A-CSOS will be one of the most promising algorithm for ORPD and an encouraging algorithm for other constrained optimization problems.

Problem Description

The minimization of Ploss which is the first objective function in this study, means the amount of active power losses in transmission lines. TVD minimization, which is taken as the second objective function in this study, is used for minimizing absolute deviations of all the actual PQ bus voltages from their desired or set values. The value of set voltage (V_i^{set}) is considered 1.0 p.u. for TVD minimization. The formulation of Ploss and TVD minimization are shown in Eq. (1) and Eq. (2), respectively.

$$f_1(x_1, x_2) = \sum_{br=1}^{N_{br}} \left[G_{br} \left(V_i^2 + V_j^2 - 2V_i V_j \cos \delta_{ij} \right) \right] \tag{1}$$

$$f_2(x_1, x_2) = \sum_{l=1}^{N_{PQ}} \left| V_l - V_l^{set} \right| \tag{2}$$

In Eq. (1) and (2), f_1 and f_2 denote to first and second objective functions, respectively; x_1 and x_2 denote to dependent and independent variables, respectively; N_{br} express the total number of branches; G_{br} is the conductance of line-*br* connecting buses *i* and *j*; V_i is the bus voltage magnitude at bus *i*; δ_{ij} is the phase angle difference between bus-*i* and *j*; N_{PQ} is the number of PQ-bus.

Subject to equality and inequality constraints are represented by Eq. (3) and Eq. (4), respectively.

$$g(x_1, x_2) = 0 \tag{3}$$

$$h(x_1, x_2) \leq 0 \tag{4}$$

The vector of state variable, x_1 shown in Eq. (5), compose of load bus voltages (V_l), generators' Mvar outputs (Q_G) and line

$$x_1 = \left[V_{l1}, \dots, V_{lN_{PQ}}, Q_{G1}, \dots, Q_{GN_{PV}}, S_{br1}, \dots, S_{brN_{br}} \right] \tag{5}$$

x_2, shown in Eq. (6), represents the control variables including bus voltage magnitudes of PV bus (V_G), tap ratios of transformers (T) and Mvar output of shunt compensators (Q_c), respectively.

$$x_2 = \left[V_{G1}, \dots, V_{GN_{PV}}, T_1, \dots, T_{N_T}, Q_{c1}, \dots, Q_{cN_c}\right] \quad (6)$$

where N_{PV} is the number of PV-bus, N_T is the number of tap changing transformers, N_c is the number of VAR compensators.

While both two objective functions are minimized, all equality and inequality constraints must be satisfied simultaneously.

The equality constraints denoted by g in Eq. (3) are shown in Eq. (7) and (8).

$$P_{G_i} - P_{L_i} - V_i \sum_{j=1}^{N_B} V_j \left[G_{ij} \cos(\delta_i - \delta_j) + B_{ij} \sin(\delta_i - \delta_j)\right] = 0, \quad i \in N_{PQ} \quad (7)$$

$$Q_{G_i} - Q_{L_i} - V_i \sum_{j=1}^{N_B} V_j \left[G_{ij} \sin(\delta_i - \delta_j) - B_{ij} \cos(\delta_i - \delta_j)\right] = 0, \quad i \in N_{PQ} \quad (8)$$

where N_B is the number of bus, P_{Gi} and Q_{Gi} are the amount of of active and reactive power generation for bus i, respectively; P_{Li} and Q_{Li} are the amount of of active and reactive power load for bus i, respectively.

The inequality constraints denoted by h in Eq. (4) are composed of the maximum and minimum limits of generator and load bus voltages, the minimum and maximum reactive power outputs of generators and shunt compensators, the minimum and maximum ratios of tap changing transformers, the maximum line capacity expressed in Eq. (9-14), respectively.

$$V_{Gi}^{min} \le V_{Gi} \le V_{Gi}^{max}, \quad i = 1,2, \dots, N_{Gen} \quad (9)$$

$$V_{li}^{min} \le V_{li} \le V_{li}^{max}, \quad i = 1,2, \dots, N_{PQ} \quad (10)$$

$$Q_{Geni}^{min} \le Q_{Geni} \le Q_{Geni}^{max}, \quad i = 1,2, \dots, N_{Gen} \quad (11)$$

$$Q_{Ci}^{min} \le Q_{Ci} \le Q_{Ci}^{max}, \quad i = 1,2, \dots, N_C \quad (12)$$

$$T_i^{min} \le T_i \le T_i^{max}, \quad i = 1,2, \dots, N_T \quad (13)$$

$$\left|S_{br_i}\right| \le S_{br_i}^{max}, \quad i = 1,2, \dots, N_{br} \quad (14)$$

Methods

The SOS algorithm has been developed as an important alternative to algorithms that have some algorithmic parameters that affect solution accuracy significantly and that must be specified by the user. Due to this advantage, it has been applied to many optimization problems to date and successful results have been obtained.

However, as the problem of applying the SOS algorithm becomes more complicated, the convergence time of the algorithm is prolonged and the accuracy of solution is insufficient. Therefore, the exploration and exploitation capabilities, and convergence speed of standard SOS should be enhanced.

In this section, the standard SOS algorithm is briefly explained, and then the modifications on the SOS are described in the subheadings.

SOS Algorithm

Symbiotic Organisms Search algorithm inspired by the symbiotic interactions between different organisms living in an ecosystem [19]. The mutualism, commensalism, and parasitism constitute the basic relations of SOS.

Mutualism:

Mutualism is a relationship based on the fact that the two organism in the ecosystem benefit more or less from one another. The relationship between bee and flower is an example of this phenomenon. Not only bees get benefited by collecting nectar from flower for producing into honey, but also flowers get benefited from bees that help to flowers to become fruit by pollination. This phase is mathematically expressed as follows in the standard SOS.

$$X_i^{new} = X_i^{act} + rand \times \left(X_{best} - \frac{X_i^{act} + X_j^{act}}{2} \times BF_1\right) \quad (15)$$

$$X_j^{new} = X_j^{act} + rand \times \left(X_{best} - \frac{X_i^{act} + X_j^{act}}{2} \times BF_2\right) \quad (16)$$

$$BF_1 = round(1 + rand) \quad (17)$$

$$BF_2 = round(1 + rand) \quad (18)$$

In above equations, X_i^{act} represents an organism that corresponds to ith organism in the ecosystem, X_j^{act} represents a randomly selected organism that interacts with X_i^{act}; X_{best} represents an organism with the minimum fitness value in the ecosystem; X_i^{new} and X_j^{new} denote the new obtained organisms after performing mutualism; the *rand* expression is a random value between 0 and 1; BF_1 and BF_2 are benefit factors which represent the level of benefit to each organism. If the value of BF is 1, organisms are benefitted partially; otherwise one organism is benefited fully from this relationship. The new obtained organisms X_i^{new} and X_j^{new} are compared with X_i^{act} and X_j^{act} according to their fitness value and then the organisms that have better fitness value are accepted.

Commensalism:
Commensalism is the type of relationship in which one organism in the ecosystem benefits from this relation while the other is unaffected. The relationship between shark and remora fish is an example of this phenomenon. Remora fish adhere to the shark and feeds by eating residue from shark's food. Therefore, the remora fish get benefit, whereas the shark is not affected by the natural process of remora fish. This phase is mathematically expressed as follows in standard SOS:

$$X_i^{new} = X_i^{act} + rand(-1,1)\left(X_{best} - X_j^{act}\right) \tag{19}$$

where X_i^{new} denotes the new obtained organism after performing commensalism; the expression *rand(-1,1)* is the random value between -1 and 1. The assessment of the obtained new organism X_i^{new} is the same as in the mutualism phase.

Parasitism:
Parasitism is defined as the type of relationship that one of the two organisms in the ecosystem has benefited from this relation while the other is harmed. The interaction between a plasmodium anopheles and human is an example of this phenomenon. If an infected anopheles mosquito bites at human, anopheles gets benefit because of feeding. The human, by contrast, is damaged by a fatal parasite that causes malaria.

X_i^{act} denotes to parasite vector. To be a parasite vector, modifies itself by the help of a random vector. For hosting to the parasite vector, an organism X_j^{act} is randomly selected. The fitness value of infected vector X_j^{act} and parasite vector X_i^{act} is calculated. If the parasite vector has a better fitness value than infected vector, kills to infected vector and substitute X_j^{act}, otherwise, X_j^{act} kills to parasite vector and remain the position of X_j^{act}.

A-CSOS Algorithm

Symbiotic Organisms Search algorithms has some disadvantages such as slow convergence and falling into local optima. Therefore, the global and local searching abilities, and convergence capability of standard SOS can be enhanced.

Chaos maps are known to significantly increase the exploration and exploitation proficiencies of the algorithms. On the other hand, the success of an algorithm depends not only on its own capabilities but also on the chosen constraint handling strategy. Standard SOS is enhanced by incorporating the chaos and adaptive penalty features. The modifications are specified in following subsections.

Chaos Integration in Mutualism and Commensalism Phases

In this study, logistic map that is one of the most used chaotic maps is preferred. The logistic map is applied to the *rand* statement in mutualism phase and *rand(-1,1)* statement in commensalism phase which is expressed in state equation form as:

$$c_{i,j}^k = 4c_{i,j-1}^k\left(1 - c_{i,j-1}^k\right) \tag{20}$$

where $c_{i\,j}^k$ represents the *j*th chaotic variable of *i*th individual in the *k*th iteration; initial value of chaotic variable C_0 can take any value between 0 and 1 except 0.25, 0.5, and 0.75. The updated formulas of the mutualism and commensalism phases after the modifications are shown in Eq. (21-23).

$$X_i^{new} = X_i^{act} + c_i^k\left(X_{best} - \frac{X_i^{act} + X_j^{act}}{2} \times BF_1\right) \tag{21}$$

$$X_j^{new} = X_j^{act} + c_j^k\left(X_{best} - \frac{X_i^{act} + X_j^{act}}{2} \times BF_2\right) \tag{22}$$

$$X_i^{new} = X_i^{act} + (2c_i^k - 1)\left(X_{best} - X_j^{act}\right) \tag{23}$$

Global Compatitive Ranking

In most studies, if one of the constraints is exceeded, a penalty value is added to the objective function for manipulating candidate individual from infeasible to feasible region. Commonly used fitness function for ORPD problem is given as follow:

$$F(X_i) = f(X_i) + k_v \sum_{i=1}^{N_{PQ}} \left(V_{l_i} - V_{l_i}^{lim}\right)^2 + k_Q \sum_{i=1}^{N_{Gen}} \left(Q_{Gen_i} - Q_{Gen_i}^{lim}\right)^2 \tag{24}$$

where $f(X_i)$ denotes the objective function value of or organism-*i*; k_V and k_Q are expressed as static penalty factors; V_{li}^{lim} and V_{Gini}^{lim} are the permissible limits of load bus voltage and Mvar output of generators, respectively. These limits are considered as follows:

$$V_{l_i}^{lim} = \begin{cases} V_{l_i}^{min}, if\ V_{l_i} < V_{l_i}^{min} \\ V_{l_i}^{max}, if\ V_{l_i} > V_{l_i}^{max} \\ V_{l_i}, if\ V_{l_i}^{min} \le V_{l_i} \le V_{l_i}^{max} \end{cases} \tag{25}$$

$$Q_{Gen_i}^{lim} = \begin{cases} Q_{Gen_i}^{min}, if\ Q_{Gen_i} < Q_{Gen_i}^{min} \\ Q_{Gen_i}^{max}, if\ Q_{Gen_i} > Q_{Gen_i}^{max} \\ Q_{Gen_i}, if\ Q_{Gen_i}^{min} \le Q_{Gen_i} \le Q_{Gen_i}^{max} \end{cases} \tag{26}$$

It is very difficult and time-consuming process to determine ideal values of the penalty parameters in static penalty method. Moreover, the solution is very sensitive to penalty coefficients. The mentioned drawbacks of the static penalty function blight the performance of the SOS algorithm. For this reason, Global Competitive Ranking has an important advantage with this aspect.

One of the adaptive penalty methods is Global Competitive Ranking (GCR) developed by Runarsson and Yao. GCR is a ranking-based constraint handling method and strikes a balance between objective function and the sum of constraints violations using the following expressions [24]

$$F(X_i) = P_f \frac{rank_1 - 1}{N - 1} + (1 - P_f) \frac{rank_2 - 1}{N - 1} \quad (27)$$

where

$$rank_1 = rank\big(f(X_i)\big) \quad (28)$$

$$rank_2 = rank\left(\sum_{j=1}^{m} v_j(X_i)\right) \quad (29)$$

$$v_j(X_i) = max\{0, g_j(X_i)\} \quad (30)$$

In above equations, N is the number of candidate solution in the population; $rank(f(X_i))$ and $rank(\sum_{j=1}^{m} v_j(X_i))$ denote the current ranking position of the candidate solution X_i based on its objective function value and the sum of its constraint violations, respectively; $v_j(X_i)$ is the amount of violation of the j-th constraint for the candidate solution X_i; P_f represents the probability that an individual's fitness function value is determined according to its objective function value. It is suggested by the author that a value between 0 and 0.5 for the P_f value.

The flow diagram for solving the ORPD problem with the A-CSOS algorithm is shown in Figure 1.

Findings

Optimal reactive power dispatch problem is applied on IEEE 30-bus system. Within this scope, the following four different cases are studied in this paper.

Case-1: Ploss minimization with continuous variables

Case-2: Ploss minimization with discrete variable transformer taps and shunt compensator outputs

Case-3: TVD minimization with continuous variables

Case-4: TVD minimization with discrete variable transformer taps and shunt compensator outputs

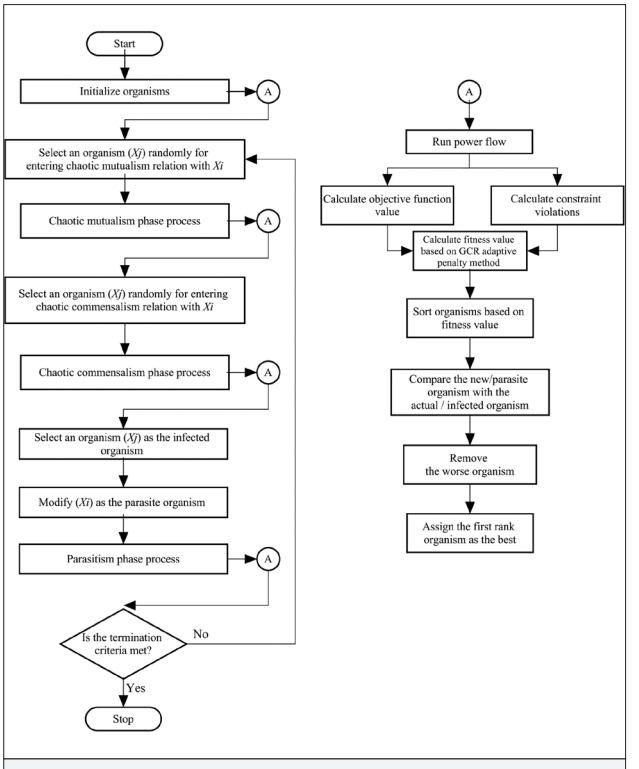

Figure 1 . The flow diagram of the solution of ORPD problem using A-CSOS

Table 1. The general description of IEEE-30 bus power systems

Parameters	IEEE 30-bus
N_B	30
N_{Gen}	6
N_{PQ}	24
N_T	4
N_C	9
$N_{reactor}$	-
N_{br}	41
$P_{load\ (MW)}$	283.2
$Q_{load\ (Mvar)}$	126.2
No. of equality contraints	60
No. of inequality contraints	125
No. of continuous variable (Case-1 and 3)	19
No. of discrete variable (Case-1 and 3)	-
No. of continuous variable (Case-2 and 4)	6
No. of discrete variable (Case-2 and 4)	13
Initial power loss (MW)	5.5713
Initial TVD (p.u.)	0.8603

Matpower [25] is used for the test power system data and load flow analysis of the simulations. The permissible maximum iteration is set to 100. The ecosystem consists of 30 organisms. The algorithm is tested with 30 runs of each test case and the best results are given. The general description and initial condition of test power systems are shown in Table 1 [26].

Table 2. The limits of control variables for IEEE 30-bus

V_G^{min}	V_G^{max}	V_l^{min}	V_l^{max}
0.95 p.u.	1.1 p.u.	0.95 p.u.	1.1 p.u.
T^{min}	T^{max}	Q_C^{min}	Q_C^{max}
0.9 p.u.	1.1 p.u.	0 Mvar	5 Mvar

The IEEE 30-bus system has 19 control variables which are 6 generator bus voltages, 4 tap ratios of transformers and 9 shunt VAR compensators. The limits of control variables are given in Table 2.

Results of Case-1 using the A-CSOS algorithm

As mentioned earlier, it is assumed that all control variables are continuous in Case-1. Table 3 presents the optimal value of control variables and the best objective value obtained from 30 test runs for Case-1. The results of the other well-known algorithms are also given in Table 3.

According to Table 3, A-CSOS are able to reduce the Ploss by 19% with respect to the base case. In comparison with the best result of other algorithms, A-CSOS algorithm gives 0.01621 MW better result.

Table 3. Optimal settings of the control variables for Case-1

Variable	A-CSOS	HFA [7]	QOCRO [12]	PSOGSA [6]	BBO [5]	DE [4]	QOTLBO [10]	CLPSO [3]	WOA [11]	IGSA-CSS [15]	MDE [14]
V_{G1}	1.10000	1.1000	NR	1.1000	1.1000	1.1000	1.1000	1.1000	1.1000	1.0813	1.07146
V_{G2}	1.09430	1.0543	NR	1.0944	1.0944	1.0931	1.0942	1.1000	1.0963	1.0722	1.06222
V_{G5}	1.07470	1.0751	NR	1.0749	1.0749	1.0736	1.0745	1.0795	1.0789	1.0501	1.0400
V_{G8}	1.07660	1.0868	NR	1.0767	1.0768	1.0756	1.0765	1.1000	1.0774	1.0502	1.0405
V_{G11}	1.10000	1.1000	NR	1.1000	1.0999	1.1000	1.1000	1.1000	1.0955	1.1000	1.0804
V_{G13}	1.10000	1.1000	NR	1.1000	1.0999	1.1000	1.0999	1.1000	1.0929	1.0688	1.0520
$T_{6\text{-}9}$	1.04320	0.9800	NR	1.0452	1.0435	1.0465	1.0664	0.9154	0.9936	1.0800	1.0834
$T_{6\text{-}10}$	0.90000	0.9500	NR	0.9000	0.9011	0.9097	0.9000	0.9000	0.9867	0.9020	0.9000
$T_{4\text{-}12}$	0.97905	0.9701	NR	0.9794	0.9824	0.9867	0.9949	0.9000	1.0214	0.9900	0.9913
$T_{28\text{-}27}$	0.96472	0.9700	NR	0.9651	0.9692	0.9689	0.9714	0.9397	0.9867	0.9760	0.9769
Q_{C10}	5.00000	4.7003	NR	5.0000	5.0000	5.0000	5.0000	4.9265	3.1695	0.0000	5.0000
Q_{C12}	5.00000	4.7061	NR	5.0000	4.9870	5.0000	5.0000	5.0000	2.0477	0.0000	5.0000
Q_{C15}	4.80690	4.7006	NR	5.0000	4.9910	5.0000	5.0000	5.0000	4.2956	3.8000	5.0000
Q_{C17}	4.99990	2.3059	NR	5.0000	4.9970	5.0000	5.0000	5.0000	2.6782	4.9000	5.0000
Q_{C20}	4.03010	4.8035	NR	3.9792	4.9900	4.4060	4.4500	5.0000	4.8116	3.9500	4.0670
Q_{C21}	5.00000	4.9025	NR	5.0000	4.9950	5.0000	5.0000	5.0000	4.8163	5.0000	5.0000
Q_{C23}	2.51700	4.8040	NR	2.4583	3.8750	2.8004	2.8300	5.0000	3.5739	2.7500	3.1570
Q_{C24}	5.00000	4.8052	NR	5.0000	4.9870	5.0000	5.0000	5.0000	4.1953	5.0000	5.0000
Q_{C29}	2.19760	3.3983	NR	2.1865	2.9100	2.5979	2.5600	5.0000	2.0009	2.4000	2.9840
BOFV	**4.51279**	**4.5290**	**4.5303**	**4.5309**	**4.5510**	**4.5550**	**4.5594**	**4.5615**	**4.5943**	**4.7660**	**4.8728**
TVD	2.05630	1.6250	2.0995	2.0504	NR	1.9589	1.9057	0.4773	NR	NR	0.9051

BOFV: Best Objective Function Value; TVD: Total Voltage Deviation; NR: not reported

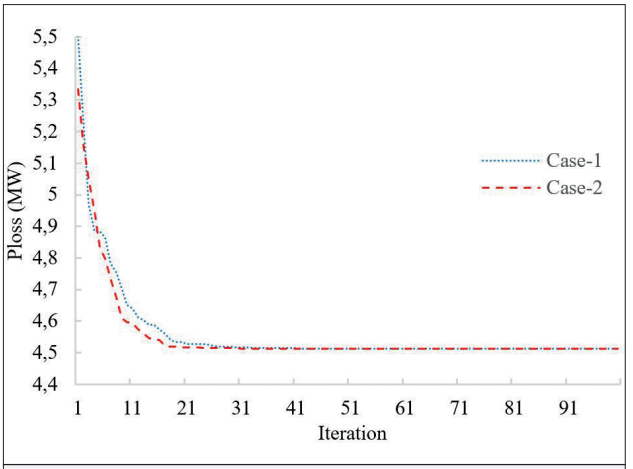

Figure 2 . The convergence characteristic of A-CSOS for Case-1 and Case-2

The convergence profile of A-CSOS algorithm over 100 iterations for Case-1 is shown in Figure 2. It is seen from the convergence performance of Case-1 optimization in Figure 2, the minimum value convergence obtained by the proposed algorithm is approximately twenty fifth iteration.

Results of Case-2 using the A-CSOS algorithm

In Case-2 optimization, it is assumed that the output of capacitors and tap ratios are discrete. The minimum value obtained by the A-CSOS algorithm and the other well-known algorithms for Case-2 analysis and the control parameter values for the best results are presented in Table 4.

Although the optimization problem is more difficult when the control parameters are discrete variables, it is seen that the A-CSOS algorithm achieves much better values than the results obtained with the other algorithms reported in Table 4.

Table 4. Optimal settings of the control variables for Case-2

Variable	A-CSOS	GSA [7]	FA [7]	ALO [9]	ABC [7]	GWO [9]	BFOA [7]	BA [9]	PSO [7]	MOCIPSO [16]
V_{G1}	1.1000	1.0999	1.1000	1.1000	1.1000	1.1000	1.1000	1.1000	1.1000	1.1000
V_{G2}	1.0943	1.07435	1.0644	1.0953	1.061	1.09380	1.026	1.0940	1.1000	1.1000
V_{G5}	1.0747	1.07498	1.07455	1.0767	1.0711	1.0737	1.0696	1.0740	1.0850	1.1000
V_{G8}	1.0761	1.07682	108690	1.0788	1.0849	1.0797	1.1000	1.0760	1.0838	1.1000
V_{G11}	1.1000	1.0999	1.09164	1.1000	1.1000	1.1000	1.1000	1.1000	1.1000	1.1000
V_{G13}	1.1000	1.0999	1.0990	1.1000	1.0665	1.0944	1.1000	1.1000	1.1000	0.9000
$T_{6\text{-}9}$	1.0400	1.0000	1.0000	1.0100	0.9700	0.9800	0.9800	0.9500	1.1000	0.9400
$T_{6\text{-}10}$	0.9000	0.9300	0.9000	0.9900	1.0500	0.9700	0.9400	1.0300	0.9000	1.0800
$T_{4\text{-}12}$	0.9800	0.9800	1.0000	1.0200	0.9900	1.0200	1.0500	0.9900	1.0200	1.1000
$T_{28\text{-}27}$	0.9600	0.9700	0.9700	1.0000	0.9900	0.9900	0.9800	0.9700	0.9900	0.9700
Q_{C10}	5.0000	3.7000	3.0000	4.0000	5.0000	2.0000	3.1000	5.0000	1.1000	6.0000
Q_{C12}	5.0000	4.3000	4.0000	2.0000	5.0000	5.0000	4.6000	0.0000	0.4000	3.0000
Q_{C15}	4.8600	3.7000	3.3000	4.0000	5.0000	4.0000	5.0000	5.0000	0.7000	7.0000
Q_{C17}	5.0000	2.2000	3.5000	3.0000	5.0000	4.0000	2.1000	5.0000	5.0000	6.0000
Q_{C20}	4.0600	3.1000	3.9000	2.0000	4.1000	4.0000	3.7000	0.0000	4.7000	0.0000
Q_{C21}	5.0000	3.9000	3.2000	4.0000	3.3000	0.0000	2.3000	0.0000	1.0000	12.000
Q_{C23}	2.5300	4.2000	1.3000	3.0000	0.9000	5.0000	1.9000	0.0000	3.0000	3.0000
Q_{C24}	5.0000	4.4000	3.5000	5.0000	5.0000	3.0000	2.3000	5.0000	0.8000	7.0000
Q_{C29}	1.7700	2.0000	1.4200	5.0000	2.4000	3.0000	0.1000	0.0000	1.2000	3.0000
BOFV	**4.51366**	**4.5400**	**4.5691**	**4.5900**	**4.6022**	**4.6119**	**4.6230**	**4.6280**	**4.6609**	**5.1700**
TVD	2.0708	1.9410	1.7752	NR	0.7378	NR	1.5300	NR	1.4600	NR

BOFV: Best Objective Function Value; TVD: Total Voltage Deviation; NR: not reported

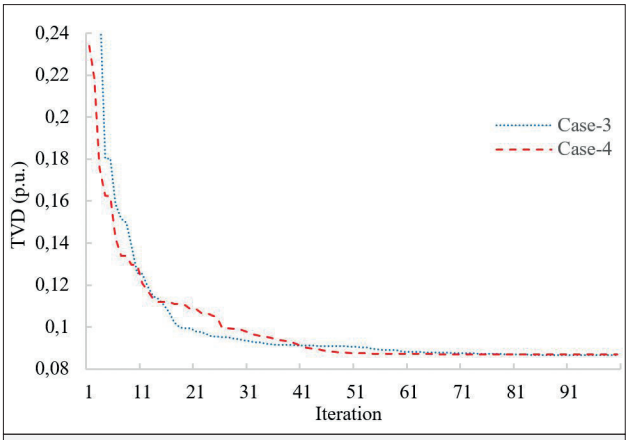

Figure 3. The convergence characteristic of A-CSOS for Case-3 and Case-4

The convergence profile of A-CSOS algorithm for Case-2 optimization is shown in Figure 2. As can be seen in Figure 2, with the contributions of chaos and adaptive penalty approaches, organisms in the ecosystem find the global minimum or near global minimum point in a very short time.

Results of Case-3 using the A-CSOS algorithm

The TVD minimization denoted Case-3 adjusts the values of the control parameters so that the voltage magnitudes of the buses can be operated as close as possible to the nominal value specified in the grid code of the countries. It is assumed that all control variables are continuous in Case-3.

Table 5 demonstrates the best TVD value and the value of control parameters within this aim. The TVD value, which is 0.8603 p.u. according to the base case scenario, is reduced to 0.08679 p.u. when optimized with the A-CSOS algorithm. Compared

Table 5. Optimal settings of the control variables for Case-3

Variable	A-CSOS	IGSA-CSS [15]	QOCRO [12]	PSOGSA [6]	MDE [14]	DE [4]	TLBO [10]	PSO [6]	GSA [7]	CPVEI HBMO [17]	CLPSO [3]
V_{G1}	1.00940	1.0085	NR	1.0153	1.0000	1.0100	1.0121	1.0264	0.9930	1.0728	1.1000
V_{G2}	1.00460	1.0057	NR	1.0122	1.0089	0.9918	0.9806	1.0162	0.9552	1.0408	1.1000
V_{G5}	1.01800	1.0191	NR	1.0185	1.0199	1.0179	1.0207	1.0185	1.0189	1.0379	1.0724
V_{G8}	1.01100	1.0103	NR	1.0107	1.0000	1.0183	1.0163	0.9987	1.0189	1.0401	1.0764
V_{G11}	1.00290	1.0184	NR	0.9889	1.0647	1.0114	1.0293	1.0427	1.0120	1.0841	1.0452
V_{G13}	1.01420	1.0080	NR	1.0083	1.0267	1.0282	1.0323	0.9965	1.0360	1.0220	1.1000
$T_{6\text{-}9}$	1.01760	1.0340	NR	1.0024	1.0852	1.0265	1.0435	1.0598	1.0578	0.9541	1.0177
$T_{6\text{-}10}$	0.90012	0.9000	NR	0.9000	0.9000	0.9038	0.9056	0.9144	1.0500	1.1000	0.9738
$T_{4\text{-}12}$	0.99588	0.9840	NR	0.9791	1.0106	1.0114	1.0195	0.958	0.9000	1.0260	1.0244
$T_{28\text{-}27}$	0.96900	0.9780	NR	0.9737	0.9744	0.9635	0.9492	0.9758	1.0500	1.0000	0.9896
Q_{C10}	4.82560	5.0000	NR	4.3048	5.0000	4.9420	4.8400	4.9995	0.9660	0.0000	0.7220
Q_{C12}	5.00000	5.0000	NR	2.3931	1.6290	1.0885	0.6600	0.0000	4.5000	0.0000	1.6812
Q_{C15}	4.99950	5.0000	NR	5.0000	5.0000	4.9985	5.0000	5.0000	2.5000	4.3906	2.6462
Q_{C17}	0.00000	0.0000	NR	0.0000	0.0000	0.2393	0.0900	4.9958	1.4000	3.3020	3.4105
Q_{C20}	5.00000	5.0000	NR	5.0000	5.0000	4.9958	5.0000	5.0000	4.0000	3.5085	1.9773
Q_{C21}	4.99740	5.0000	NR	5.0000	5.0000	4.9075	5.0000	5.0000	3.8000	0.0000	0.4767
Q_{C23}	5.00000	5.0000	NR	5.0000	5.0000	4.9863	4.9500	4.9988	2.9000	2.4534	3.5896
Q_{C24}	4.99880	5.0000	NR	5.0000	5.0000	4.9663	4.9300	5.0000	2.5000	5.0000	2.9998
Q_{C29}	2.61840	4.9500	NR	4.1670	5.0000	2.2325	0.2400	4.9994	3.1000	1.8260	1.1098
BOFV	**0.08679**	**0.08968**	**0.0899**	**0.0904**	**0.0910**	**0.0911**	**0.0913**	**0.1005**	**0.1180**	**0.1988**	**0.2450**
Ploss	5.8668	NR	5.6486	5.7344	5.9991	6.4755	7.1859	5.5192	5.8200	4.9948	4.6969

BOFV: Best Objective Function Value; TVD: Total Voltage Deviation; NR: not reported

with the best results of other algorithms, the A-CSOS algorithm solves the optimization problem better than the other algorithms by 3.22%.

The convergence profile of A-CSOS algorithm for Case-3 optimization is shown in Figure 3.

Results of Case-4 using the A-CSOS algorithm

In Case-4 optimization, it is assumed that the output of capacitors and tap ratios are discrete. The optimal value of control variables for the obtained minimum TVD value is presented in Table 6. The convergence profile of A-CSOS is shown in Figure 3.

According to Table 6, TVD is to be reduced by 89.89% (0.77329 p.u.) with respect to the base case. In comparison with the best result of declared state-of-art algorithms, A-CSOS algorithm gives 10.39% (0.01009 p.u.) better result.

It is seen from Figure 3 that A-CSOS finds the minimum and feasible TVD solution approximately in fifth iteration.

Conclusion

In this paper, SOS algorithm is hybridized with chaos theory and self-adaptive penalty approach in order to design a novel meta-heuristic Adaptive Chaotic Symbiotic Organisms Search Algorithm (A-CSOS) for solving highly nonlinear ORPD problem. The ability of the proposed A-CSOS algorithm is proofed by implementing on both continuos and discrete ORPD problem consisting of active power loss and total voltage deviation minimization in IEEE 30-bus.

According to Case-1 results, it is understood that the A-CSOS algorithm yields 19% better than the base case and 0.36% better than the best results of the other algorithms reported. According to Case-2 results, it is seen that the A-CSOS algo-

Table 6. Optimal settings of the control variables for Case-4

Variable	A-CSOS	MALO [8]	HFA [7]	CSA [8]	FA [7]	BA [7]	ALO [7]	ABC [7]	BFO [7]
V_{G1}	1.0079	1.0049	1.0035	0.9658	0.9977	1.0186	1.0131	1.0025	0.9500
V_{G2}	1.0034	0.9504	1.0164	1.0395	1.0217	0.9797	1.0262	1.0162	1.0702
V_{G5}	1.0181	1.0382	1.0195	1.0198	1.0167	1.0193	1.0194	0.9927	0.9645
V_{G8}	1.0110	1.0122	1.0182	0.9993	1.0010	1.0475	1.0264	1.0288	1.0258
V_{G11}	1.0145	1.0406	0.9823	1.0386	1.0481	0.9938	0.9949	1.0647	1.0375
V_{G13}	1.0090	1.0216	1.0155	1.0494	1.0191	0.9753	0.9732	1.0086	0.9914
$T_{6\text{-}9}$	1.0300	1.0700	0.9900	1.0500	1.0400	0.9800	0.9900	0.9700	0.9800
$T_{6\text{-}10}$	0.9000	0.9100	0.9000	0.9200	0.9000	0.9200	0.9200	1.0300	0.9600
$T_{4\text{-}12}$	0.9800	1.0100	0.9800	1.0500	0.9800	0.9600	0.9500	0.9700	1.0200
$T_{28\text{-}27}$	0.9700	0.9600	0.9600	0.9600	0.9600	0.9700	0.9700	0.9500	0.9900
Q_{C10}	5.0000	3.8000	3.2000	0.3900	3.6000	3.4700	4.4000	2.5000	4.8000
Q_{C12}	3.0400	4.7600	0.5000	2.7900	1.3000	2.4500	4.2000	0.0000	1.3000
Q_{C15}	5.0000	5.0000	4.9000	4.7800	2.7000	3.3700	2.6000	5.0000	4.5000
Q_{C17}	0.0000	2.2600	0.1000	5.0000	0.9000	3.6300	1.1000	0.0000	2.0000
Q_{C20}	5.0000	4.8400	3.8000	4.9600	4.2000	4.3400	3.7000	5.0000	4.3000
Q_{C21}	5.0000	5.0000	5.0000	5.0000	2.7000	3.6200	3.4000	5.0000	3.9000
Q_{C23}	5.0000	5.0000	5.0000	5.0000	3.0000	3.4100	3.6000	5.0000	4.0000
Q_{C24}	5.0000	5.0000	3.9000	4.3000	1.7000	4.0500	3.9000	4.7000	4.5000
Q_{C29}	2.8600	0.5800	1.5000	2.7200	1.8000	2.3500	1.9000	0.0000	3.4000
BOFV	**0.08701**	**0.0971**	**0.0980**	**0.1116**	**0.1157**	**0.1161**	**0.1177**	**0.1350**	**0.1490**
TVD	5.9157	5.9020	5.7500	7.9467	6.3400	5.6543	5.9138	5.8800	10.570

BOFV: Best Objective Function Value; TVD: Total Voltage Deviation; NR: not reported

rithm yields 18.98% better than the base case and 0.58% better than the best results of the other latest algorithms. According to Case-3 results, it is understood that the A-CSOS algorithm yields 89.91% better than the base case and 3.22% better than the best results of the other state-of-art algorithms. According to Case-4 results, it is inferred that the A-CSOS algorithm yields 89.89% better than the base case and 10.39% better than the best results of the other latest algorithms. Since the ecosystem is sorted in terms of the value of the objective functions and total constraint violation, the proposed algorithm requires more processing and computation time than the standard SOS algorithm. Considering the best results obtained with the proposed algorithm and the elimination of the determining process of penalty coefficients, the additional computation time is acceptable.

The obtained results indicate that the proposed algorithm yields a lower Ploss and TVD value than the best result of the other algorithms. When the results are evaluated, the proposed algorithm yields a lower Ploss and TVD value than the best result of the other algorithms.

Peer-review: Externally peer-reviewed.

Conflict of Interest: The authors have no conflicts of interest to declare.

Financial Disclosure: The authors declared that the study has received no financial support

References

1. K.Y. Lee, Y.M. Park, J.L. Ortiz, "A united approach to optimal real and reactive power dispatch", IEEE Trans Power Appar Syst, vol. 5, no. 5 , pp. 1147-1153, May, 1985. [CrossRef]
2. J. Carpentier, "Optimal power flows", Electr Power Energy Syst, vol. 1, no. 1, pp. 3-15, Apr, 1979. [CrossRef]
3. K. Mahadevan, P.S. Kannan, "Comprehensive learning particle swarm optimization for reactive power dispatch", Appl Soft Comput, vol. 10, no. 2, pp. 641-652, Mar, 2010. [CrossRef]
4. A.A. Abou El Ela, M.A. Abido, S.R. Spea, "Differential evolution algorithm for optimal reactive power dispatch", Electr Pow Syst Res, vol. 81, no. 2, pp. 458-464, Feb, 2011. [CrossRef]
5. A. Bhattacharya, P.K. Chattopadhyay, "Solution of optimal reactive power flow using biogeography-based optimization", International Journal of Electrical and Computer Engineering, vol. 4, no. 3, pp. 621-629, 2010.
6. J. Radosavljevic, M. Jevtic, M. Milovanovic, "A solution to the ORPD problem and critical analysis of the results", Electr Eng, vol. 100, no. 1, pp 253-265, Mar, 2018. [CrossRef]
7. A. Rajan, T. Malakar, "Optimal reactive power dispatch using hybrid Nelder-Mead simplex based firefly algorithm", Electr Power Energy Syst, vol. 66, pp 9-24, Mar, 2015. [CrossRef]
8. A. Rajan, K. Jeevan, T. Malakar, "Weighted elitism based Ant Lion Optimizer to solve optimum VAr planning problem", Appl Soft Comput, vol. 55, pp. 352-370, Jun, 2017. [CrossRef]
9. S. Mouassa, T. Bouktir, A. Salhi, "Ant lion optimizer for solving optimal reactive power dispatch problem in power systems", Eng Sci Technol Int J, vol. 20, no. 3, pp. 885-895, Jun, 2017. [CrossRef]
10. B. Mandal, P. K.. Roy, "Optimal reactive power dispatch using quasi-oppositional teaching learning based optimization", Electr Power Energy Syst, vol. 53, pp. 123-134, Dec, 2013. [CrossRef]
11. K.b.o. Medani, S. Sayah, A. Bekrar, "Whale optimization algorithm based optimal reactive power dispatch: A case study of the Algerian power system", Electr Power Syst Res, Oct, 2017, unpublished.
12. S. Dutta, S. Paul, P.K. Roy, "Optimal allocation of SVC and TCSC using quasi-oppositional chemical reaction optimization for solving multi-objective ORPD problem", Journal of Electrical Systems and Information Technology, vol. 5, no. 1, pp. 83-98, May, 2018. [CrossRef]
13. B. Shaw, V. Mukherjee, S.P. Ghoshal, Solution of reactive power dispatch of power systems by an opposition-based gravitational search algorithm, Electr Power Energy Syst, vol. 55, pp. 29-40, Feb, 2014. [CrossRef]
14. H. Singh, L. Srivastava, "Modified differential evolution algorithm for multi-objective VAR management", Electr Power Energy Syst, vol. 55, pp. 731-740, Feb, 2014. [CrossRef]
15. G. Chen, L. Liu, Z. Zhang, S. Huang, "Optimal reactive power dispatch by improved GSA-based algorithm with the novel strategies to handle constraints", Appl Soft Comput, vol. 50, pp. 58-70, Jan, 2017. [CrossRef]
16. G. Chen, L. Liu, P. Song, Y. Du, "Chaotic improved PSO-based multi-objective optimization for minimization of power losses and Lindex in power systems", Energy Convers Manage, vol. 86, pp. 548-560, Oct, 2014. [CrossRef]
17. A. Ghasemi, K. Valipour, A. Tohidi, "Multi objective optimal reactive power dispatch using a new multi objective strategy", Electr Power Energy Syst, vol. 57, pp. 318-334, May, 2014. [CrossRef]
18. M. Mehdinejad, B. Mohammadi-Ivatloo, R. Dadashzadeh-Bonab, K. Zare, "Solution of optimal reactive power dispatch of power systems using hybrid particle swarm optimization and imperialist competitive algorithms", Electr Power Energy Syst, vol. 83, pp. 104-116, Dec, 2016. [CrossRef]
19. M.Y. Cheng, D. Prayogo, "Symbiotic Organisms Search: A new metaheuristic optimization algorithm", Computers & Structures, vol. 139, pp. 98-112, Jul, 2014. [CrossRef]
20. U. Guvenc, S. Duman, M.K. Dosoglu, et al., "Application of Symbiotic Organisms Search Algorithm to solve various economic load dispatch problems", 2016 International Symposium on INnovations in Intelligent SysTems and Applications, Sinaia, Romania, 2016. [CrossRef]
21. B. Das, V. Mukherjee, D. Das, "DG placement in radial distribution network by symbiotic organisms search algorithm for real power loss minimization", Applied Soft Computing, vol. 49, pp. 920-936, Dec, 2016. [CrossRef]
22. D.C. Secui, "A modified Symbiotic Organisms Search algorithm for large scale economic dispatch problem with valve-point effects", Energy, vol. 113, pp. 366-384, Oct, 2016. [CrossRef]
23. A. Saha, A.K. Chakraborty, P. Das, "Quasi-reflection based symbiotic organisms search algorithm for solving static optimal power flow problem", Scientia Iranica, Feb, 2018.
24. T.P. Runarsson, X. Yao, "Constrained evolutionary optimization," in Evolutionary Optimization: International Series in Operations Research&Management Science, Boston, MA: Springer, 2003, vol. 48, pp. 87-113. [CrossRef]
25. R.D. Zimmerman, C.E. Murillo-Sanchez, R.J. Thomas, "MATPOWER: Steady-State Operations, Planning and Analysis Tools for Power Systems Research and Education", IEEE Trans Power Syst, vol. 26, no. 1, pp. 12-19, Feb, 2011. [CrossRef]
26. The IEEE 30-bus test system. (2017, Mar 15). Retrieved from http://www.ee.washington.edu/research/pstca/pf30/pgtca30bus.htm

Enes Yalçın received the B.Sc degree in Electrical and Electronics Engineering from Kırıkkale University in 2006 and M.Sc degree in Electrical and Electronics Engineering from Kırıkkale University in 2010. He is currently a Technical Inspector in TEİAŞ and Ph.D student at Gazi University. His research interests include power system optimization, optimal power flow, grid integration of renewable energy sources and transmission system planning.

Müslüm Cengiz Taplamacıoğlu graduated from Department of Electrical and Electronics Engineering, Gazi University. He received the degrees of M.Sc. in Industrial Engineering from Gazi University and in Electrical and Electronics Engineering from Middle East Technical University and received the degree of Ph.D. in Electrical, Electronics and System Engineering from University of Wales (Cardiff, UK). He has been a full time Professor of the Electrical and Electronics Engineering since 2000. He is currently working as a Professor at Gazi University. His research areas consist of high voltage engineering, optimization of power system operation and control problems, renewable energy source integration problems, electrical field computation, power systems and protection devices.

Ertuğrul Çam received the B.Sc degree in Electrical and Electronics Engineering from Dokuz Eylul University in 1996, the M.Sc degree in Electrical and Electronics Engineering from Ege University in 1999 and the Ph.D degree in Mechanical Engineering from Kırıkkale University in 2004. He is currently working as a Professor at Kırıkkale University. His research areas consist of power system control, renewable energy sources, fuzzy logic.

İSTANBUL UNIVERSITY
CERRAHPAŞA

RESEARCH ARTICLE
Electrica 2019; 19(1): 48-58

A Linear Stochastic System Approach to Model Symptom Based Clinical Decision Support Tool for the Early Diagnosis for Psoriasis, Seborrheic Dermatitis, Rosacea and Chronic Dermatitis

İnci Zaim Gökbay[1], Zeynep Beyza Zileli[2], Pelin Sarı[2], Türker Togay Aksoy[3], Sıddık Yarman[4]

[1]Department of Informatics, İstanbul University, İstanbul, Turkey
[2]Institue of Graduate Studies Science and Engineering, İstanbul University-Cerrahpaşa, İstanbul, Turkey
[3]Department of Biomedical Device Technology, İstanbul Aydın University, İstanbul, Turkey
[4]Department of Electrical and Electronics Engineering, İstanbul University-Cerrahpaşa, İstanbul, Turkey

Cite this article as: Zaim Gökbay İ, Zileli ZB, Sarı P, Aksoy TT, Yarman S. A Linear Stochastic System Approach to Model Symptom Based Clinical Decision Support Tool for the Early Diagnosis for Psoriasis, Seborrheic Dermatitis, Rosacea and Chronic Dermatitis. *Electrica*, 2019; 19(1): 48-58.

ABSTRACT

Prediction models provide the probability of an event. These models can be used to predict disease's outcomes, reccurencies after treatments. This paper presents an expert system called Symptom Based Clinical Decision Support Tool (SBCDST) for early diagnosis of erythemato-squamous diseases incorporating decisions made by Bayesian classification algorithm. This tool enables family practitioners to differentiate four types of erythemato-squamous diseases using clinical parameters obtained from a patient. In SBCDST, Psoriasis, Seborrheic Dermatitis, Rosacea and Chronic dermatitis diseases are described by means of well-classified set of attributes. Attributes are generated from the typical sign and symptoms of disorder. Based on our clinical results, tool yields 72%, 93%, 89% and 95% correct decisions on the selected dermatology diseases respectively. System proposed will provide the opportunity for early diagnosis for the patient and the expert medical doctor to take the necessary preventive measures to treat the disease; and avoid malpractice which may cause irreversible health damages.
Keywords: Clinical Decision Support Systems (CDSS), linear stochastic model, psoriasis, seborrheic dermatitis, rosacea and chronic dermatitis

Introduction

The diagnosis of erythemato-squamous diseases such as; psoriasis, seboreic dermatitis, lichen planus, pityriasis rosea, chronic dermatitis and pityriasis rubra pilaris is a difficult problem in dermatology [1]. Analyzing available information to determine the pathophysiologic explanation for a patient's symptoms is only one of the classic problems of diagnosis. But they all share the clinical features of erythema and scaling with very few differences [2]. In dermatological identification process, clinical information is at the forefront of the diagnostic process. A thorough history and total skin examination with emphasis on the duration, distribution, morphology and pattern of skin lesions are essential. Biopsy, patch testing and dermotoscopy examinations are also used to improve the quality of diagnosis.

Any computer program designed to help clinicians to make pre-diagnosis and also clinical decisions is called as clinical decision-support system. Intelligent decision support system can be based on various machine learning algorithms. Machine learning refers to how systems maps the learning process, which is often achieved by seeking and discovering patterns in data, or statistical pattern recognition.

Linear Discriminant Analysis [3, 4] is a well-known scheme for feature extraction and dimension reduction. It has been used widely in many applications. In this preliminary work, linear discriminant analysis is preferred to predict and built up a a reliable Symptom Based Clinical Decision Support Tool (SBCDST) that will be useful for the patients, for family physicians and internists to guide the patients to the dermatology expert is developed for psoriasis, seborrheic dermatitis, rosacea and chronic dermatitis.

Corresponding Author:
İnci Zaim Gökbay

E-mail:
inci.gokbay@istanbul.edu.tr

Received: 06.04.2018

Accepted: 08.11.2018

DOI: 10.26650/electrica.2018.081118

Psoriasis

Psoriasis is a primary dermal disease with chronic and recurrent properties and is widespread. It may be observed anywhere on the skin. It may affect the whole body; however, the severity of the disease differs from one individual to another. In some cases, the symptoms are local and observed in the form of plaques, whereas in other cases the symptoms may be observed in various body parts and cover large areas of the skin. The incidence of this widely common disease is between 1 to 3%. For example the prevalence of psoriasis in India ranges from 0.5% to 1.5%, 4 to 5.5% in Malaysia, 0.29 to 1.18% in Japan and 3.1 % in Kuwait, and in China, including Hong Kong ranges from 0.2% to 1.5% [5]

The most common locations where the symptoms occur are the knees, elbows, waist, scalp and the genital area. The disease typically presents itself with a thin layer of white scales on top of clearly outlined red patches, however it may also present itself in the form of red patches only or with pinhead sized infectious pustules on top of the red patches. Psoriasis is a genetic disease common in the age group of 20 to 40. As it is an inherited disease, if the parents have psoriasis, it is more likely that it will be observed in the child.

There are certain factors affecting the onset of the first attack or increasing the severity of the disease. The primary factors are physical and psychological stress, excessive exposure to sun and usage of certain drugs (pain killers, hormones, cortisone, antihypertensives). The psoriasis will be stable if the patient leads a comfortable life, avoids fatigue and consumes drugs as few as possible. One of the typical symptoms of psoriasis is that new psoriatic plaques are formed on itching or injured areas of the skin. This is known as "Koebner phenomenon" [6].

Psoriasis diagnosed based on clinical appearance may sometimes be confused with eczema or allergic dermal diseases. "Psoriasis Palmoplantaris" (psoriasis of hands and feet) is a local form of psoriasis presenting itself with blisters, cracked skin and desquamation [7].

Contrary to popular belief, chronic psoriasis is successfully cured however it may recur due to its chronic nature. The duration of and intervals between these recurrent attacks may differ between individuals [8-9].

Seborrheic Dermatitis

There are many kinds of skin disorders, seborrheic dermatitis is a kind of eczama. It is also known as seborrheic eczama. The name seborrheic dermatitis implies an oily inflammation of the skin where disease is much complex then the name given. Its most commonly seen on the scalp, nasolabial folds, ears, eyebrows and chest with complaints appearance of red, flaking, greasy areas of skin. Variations in seborrheic dermatitis clinical picture are common [10].

It may be seen in every age and gender. However, it is more frequently observed in infants, middle aged and elderly population. This kind of eczama is more common in people with oily skin. This dermal disease is caused by excessive oil secretion of the skin and it has a greater incidence in people with white complexion.

The first symptoms are itchy and red skin. Redness is accompanied by dandruff formation on the scalp, to a tiresome extent. In some cases, the skin gets disturbingly moistened and greasy. The dandruff formation on the scalp is excessive as if the skin was flaking. Minor acnes may form due to the disease itself or the irritation it causes. A yellow oil discharge stain may be formed as a result of significant moistening.

In 70% of the cases, a fungus species was found, this led to the idea that this disease is caused by or exacerbated by fungi though this has not been proven. The prevalance of seborrheic dermatitis is 1-5% in adults. This rate increases in three age groups: the first three months of infants, adolescense and ages between 40 and 60. The onset of the disease is commonly after adolescense, and lasts for years while the severity decreases or increases throughout the years. It is most common among males and the 20-40 age group [11].

Although the cause of seborrheic dermatitis is not clearly understood, it is associated with the factors like yeast Malassezia, hormones (androgens), sebum levels and immune response. The disease may be exacerbated by drugs, climate changes including temperature and humidity rate, diet, atopy, changes in pressure, neurological issues, microangiopathic vascular changes, alcohol consumption, metabolic changes, fatigue, stress and defficiency of riboflavin, pyridoxine or biotin. It is clear that Sebum has a role in the manifestation of the disease. However, sebum levels or sebum secretion is not found to be elevated in patients with seborrheic dermatitis [11-13].

Rosacea

It is a dermal disease presenting itself on central area of the face such as nose, chin, forehead and cheeks; the onset of the disease consists of rash and paraesthesia, as the disease progresses it may cause permanent redness of skin, dilation of the blood vessels, skin edema and tissue vegetation. It is also known as adult acne or acne rosacea as the symptoms are similar, however it differs from adolescence acnes as it is not caused by the activity of fat glands. The cause of Rosacea is not clearly known, some of the affecting factors are, genetic tendency, infectious causes, envorinmental factors, psychogenic factors, natural immune system respectively.

Rosacea is observed mostly in fair-skinned, colored-eyed adults of 30 to 60 years of age. Though more common among women, its course is more severe in men. Rosacea is a slow progressing disease and consists of stages (exacerbations). It has four clinical stages:

Stage 1: Relapsing paraesthesia and rash attacks on face,

Stage 2: The redness of central face area becomes permanent and obvious blood vessels form on nose and cheeks,

Stage 3: The redness on the face becomes darker and persistent, small, red swellings or pimples form on nose, cheeks, forehead and chin (diffrent from white or dark spots),

Stage 4: Burning eyes or continuous sensitiveness of the eyes (ocular rosacea) and development of a red, swelled nose (rhinophyma). The disease is often diagnosed based upon clinical findings and no biopsy is needed. There are no laboratuary findings spesific to the Rosacea diagnosis.

In 1/3 of the patients, there is involvement of the eyes. In 20% of the patients, only the eyes are involved without the involvement of the skin. It is very difficult to diagnose the disease when the skin is not involved. Ocular involvement is not related to the presence nor the severity of dermal findings. The symptoms of ocular involvement are blepharitis, conjunctivitis, ceratitis, photophobia, watering of eyes, burning of eyes, episcleritis, iridocyclitis, chronic edema around eyes, widespread pain around eyes, and blurred vision. Therefore, all patients with Rosacea shoud have ocular examination [14].

Chronic Dermatitis

Atopic eczama (endogen eczama, atopic dermetitis) is a type of itchy, chronically relapsing dermatitis seen in atopic individuals. The two most common clinical findings of atopy are atopic eczama and allergic rhinitis. The insidence of atopic eczema have been increasing over the last years [8].

Atopic dermatitis is an itchy, chronic skin disease. It may be observed at any age, however in 90 % of the cases, its onset is before 5 years of age and in 50% of these cases after the first two months of infant age. It is the most common dermal disease in children.

The insidence of the disease has increased after the second world war. The frequency of the disease is affected by industrialisation, urbanisation and climate changes. The insidence is 4.3% in 6-13 age group and 8.1% in 10-11 age group in our country.

The disease is developed as a result of interaction between envorinmental and genetic factors. Familial allergy is an important risk factor. The disease has a negative impact on the quality of life of patients of any age. The risk is three times more when both parents have allergy.

Clinical characteristics of atopic eczema and the course of the disease vary between infants, children and adults. In infants the symptoms are dark red patches and blisters on face and outer surfaces of arms and legs, as patients get older the skin gets thicker, rougher and darker. The symptoms are further observed on eye lids, skin folds of knees and elbows, and neck. The skin is dry and itchy at all stages. In 20 to 30% of the cases, skin lesions regress at the end of age two. Itchiness is the most significant finding. It gets worse towards the end of the day due to sweating and wool clothes.

The disease may be treated with topical medicine, oral drugs and sunlight (phototherapy) depending upon the severity and the surface area it covers, and the patient's age. If the disease is not treated, infections may arise [15-19].

Multi-Dimensional Linear Stochastic Model

A disease universe, $U_{\text{Skin-Diseases}}$, containing many subsets (all different types of skin disease sets) inside can be defined as shown Figure 1.

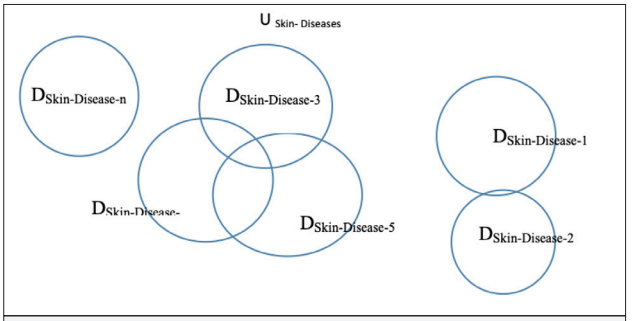

Figure 1. $U_{\text{Skin Diseases}}$ Universe and Subsets Inside Universe

Inside the $U_{\text{Skin- Diseases}}$ one subset, lets call as "D", may contain the individuals having dermatologic diseases. Subset D, can have another random set, "X" which may contain correlated variables x, with set "D". Where X, for example, is a set that is composed of the members whom owns the disease "D", then we can look for the probability P(X), of an individual to be a member of the set X. Pre-diagnosis of dermatological diseases (as other diseases), could be done by identifying the combination of some physical symptoms designated by; $\{D_1, D_2, \ldots, D_N\}$

$$D = \sum_{i=1}^{N} D_N \text{, here } N \text{ shows the total number of symptoms of disease } D \quad (1)$$

As mentioned before; patients having psoriasis, seborrheic dermatitis, rosacea or chronic dermatitis can complain similar symptoms such as erythema, scaling, definite borders and itching; that makes the diagnose difficult for family practitioners or primary care physician. This kind of basic system designs especially can support help to family practitioners or primary care physician to prevent misdiagnose. Therefore can also help to improve quality of patient's life. In our previous works [17], we proved that endocrinal diseases such as acromegaly, prolactinoma and Cushing's disease can be described by means of a stationary linear stochastic system (LSS) which is described by

$$y = \sum_{k=1}^{N} w_k x_k \quad (2)$$

Here w_k are the weight coefficients which works on the random inputs x_k's over a linear operator as specified in [15] and they are predicted employing a training set. In this work we establish the model to predict if one has the illness or what is the illness that the individual has and the possibility of having the disease. To do this we built up 4 seperate training set that contains various number of patients data who certainly has psoriasis, seborrheic dermatitis, chronic dermatitis disease and rosacea respectively Figure 2.

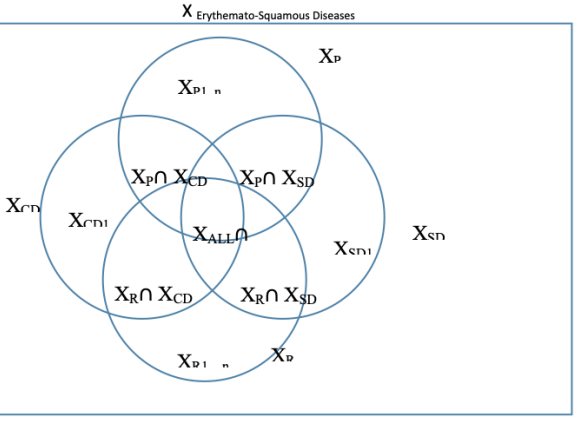

Figure 2. *$X_{Erythemato\text{-}Squamous\ Diseases}$ Universe (Subset of $U_{Skin\text{-}Disease}$) and Set Relations Inside Universe*

Steps Followed In Designing Algorithm 1: Building Sets, Determination of Attributes and Estimation of Weight Coefficients

Step 1: Ask an expert about frequent disease syndromes and develop an multiple choice anamnesis guide to obtain clinical data from patients whom certainly has the diagnose of the psoriasis, seborrheic dermatitis, chronic dermatitis disease and rosacea respectively. Also obtain more data from patients to include the coefficients of personal complaints.
Step 2: Classify the obtained clinical data base filled with anamnesis informations to extract complete set of attributes.
Step 3: Using the clinical data base construct a sample set X_S.
Step 4: Develop a module to decompose the sample set X_S into its attribute sets $\{X_s \cap X_n\}$,n=1,..N.
Step 5: Generate the training set X_T with $\sum_n^N n_k$ members.
Step 6: Estimate and store the LSS parameters for future use self tests, $w_k = \frac{n_k}{N_T}$
Step 7: Combine all steps in sequential manner under training block.

11 clinical and 22 histopathological data concerning four dermal diseases have been used in our study. Every property was graded with values of 0 1 2 or 3. The training set for psoriasis, $X_{P,}$ was formed with 100 patients who certainly had psoriasis. Every property was associated with a set and that set exhibits the severity of any property related to the patient with psoriasis. For example, set X_1 exhibits the property of dermal itchiness in psoriasis was graded 2.3 over 3. Total number of members calculated by adding of all severity grades is found to be N_T=29.98. The event set, grades of severity and weight coefficients are given in Table 1. training set for seborrheic dermatitis is established with 55 patients who certainly had seborrheic dermatitis. Total number of members of seborrheic dermatitis was found to be N_T=18.22. Calculated severities for seborrheic dermatitis disease and weight coefficients are given in Table 1. training set for chronic dermatitis disease and X_R training set for rosacea were established with 45 patients who were diagnosed. Calculated severities for chronic dermatitis disease and rosacea disease and weight coefficients are given in Table 1.

Application of Linear Stochastic System (LSS) Model

Aim of the self-test module is to enable a random user to enter attribute scores such as 1 and 0. Here 1 entrance means that individual has that complaint, 0 entrance to anamnesis means has no such a complaint. Clinical anamnesis form is designed in digital era with only choices "Have" which will be saved as 1 in database, "Dont Have" which will be saved as 0 in database.

Steps Followed In Designing Algorithm 2: Obtaining Self-Test Mode

Step 1: Design the clinical anamnesis
Step 2: Classify the obtained clinical data base filled with anamnesis informations to extract complete set of attributes.
Step 3: Using the clinical data base construct a sample set X_S.
Step 4: Develop a module to decompose the sample set X_S into its attribute sets $\{X_s \cap X_n\}, n = 1,..N$.
Step 5: Generate the training set X_T with $\sum_n^N n_k$ members.
Step 6: Estimate and store the LSS parameters for future use self tests, $w_k = \frac{n_k}{N_T}$
Step 7: Combine all steps in sequential manner under training block.

Self-tests for psoriasis, seborrheic dermatitis, chronic dermatitis and rosacea diseases were conducted using the weight coefficients from Table 2. It was checked if the patient formerly diagnosed had the properties given in Table 2, if the property was present $P(X_k)$=1; if not $P(X_k)$=0. Thus, every $P(X_k)$ value was calculated, added and a value between zero and one was reached. It was concluded that the related patient had the disease having the highest score value. In the test conducted for psoriasis the results were: $P(X_{Psoriasis})$=0.95, $P(X_{S.Dermatitis})$=0.72, $P(X_{C.Dermatitis})$=0.77 $P(X_{Rosacea})$=0.73. According to these results, the patient was supposed to have psoriasis 95%, chronic dermatitis 77%, Rosacea 73% and Seborrheic dermatitis 72%. As the highest score was reached for psoriasis, the patient may be diagnosed for psoriasis. The results are given in Table 2 in detail.

Table 1. Weight coefficients of the four dermal diseases

Event Sets	Clinical and Histopathological Properties	Psoriasis	Seborrheic Dermatitis	Chronic Dermatitis	Rosacea
X1	Erythema	0.076718	0.124751	0.086667	0.122449
X2	Scaling	0.073382	0.112774	0.061333	0.097668
X3	Definite Borders	0.070380	0.048902	0.053333	0.075802
X4	Itching	0.030354	0.094810	0.114667	0.030612
X5	Koebner Phenomenon	0.022682	0.001996	0.000000	0.080175
X6	Polygonal Papules	0.000000	0.000000	0.000000	0.000000
X7	Follicular Papules	0.001334	0.000998	0.016000	0.000000
X8	Oral Mucosal Involvement	0.000000	0.000000	0.000000	0.000000
X9	Knee and Elbow Involvement	0.052702	0002994	0.002667	0.000000
X10	Scalp Involvement	0.049700	0.006986	0.000000	0.000000
X11	Family History	0.030020	0.005988	0.000000	0.000000
X12	Melanin Incontinence	0.000000	0.000000	0.000000	0.000000
X13	Eosinophils in the Infiltrate	0.001334	0.025948	0.004000	0.002915
X14	PNL Infiltrate	0.039026	0.063872	0.000000	0.007289
X15	Fibrosis of the Papillary Dermis	0.000000	0.000000	0.137333	0.000000
X16	Exocytosis	0.010007	0.118762	0.042667	0.138484
X17	Acanthosis	0.069380	0.095808	0.136000	0.094752
X18	Hyperkeratosis	0.028019	0.009980	0.048000	0.021866
X19	Parakeratosis	0.065710	0.058882	0.049333	0.053936
X20	Clubbing of the Rete Ridges	0.069380	0.000000	0.005333	0.000000
X21	Elongation of the Rete Ridges	0.074716	0.009980	0.109333	0.000000
X22	Thinning of the Suprapapillary Epidermis	0.067045	0.000998	0.001333	0.000000
X23	Spongiform Pustule	0.031021	0.009980	0.001333	0.000000
X24	Munro Microabcess	0.036358	0.000000	0.000000	0.001458
X25	Focal Hypergranulosis	0.000000	0.000000	0.000000	0.000000
X26	Disappearance of the Granular Layer	0.035690	0.000000	0.000000	0.024781
X27	Vacuolisation and Damage of Basal Layer	0.000334	0.000000	0.000000	0.000000
X28	Spongiosis	0.000000	0.116766	0.021333	0.131195
X29	Saw-tooth Appearance of Retes	0.000000	0.000000	0.000000	0.001458
X30	Follicular Horn Plug	0.000000	0.000998	0.001333	0.000000
X31	Perifollicular Parakeratosis	0.000000	0.000998	0.000000	0.000000
X32	Inflammatory Monoluclear Inflitrate	0.063709	0.084830	0.106667	0.115160
X33	Band-like Infiltrate	0.001001	0.001996	0.001333	0.000000
		W_S=1	W_S=1	W_S=1	W_S=1

Table 2. Self-test results of psoriasis disease

Event Sets	Clinical and Histopathological Properties	Psoriasis	Seborrheic Dermatitis	Chronic Dermatitis	Rosacea	$P(X_k)$
X1	Erythema	0.076718	0.124751	0.086667	0.122449	1
X2	Scaling	0.073382	0.112774	0.061333	0.097668	1
X3	Definite Borders	0.070380	0.048902	0.053333	0.075802	1
X4	Itching	0.030354	0.094810	0.114667	0.030612	1
X5	Koebner Phenomenon	0.022682	0.001996	0.000000	0.080175	1
X6	Polygonal Papules	0	0	0	0	0
X7	Follicular Papules	0	0	0	0	0
X8	Oral Mucosal Involvement	0	0	0	0	0
X9	Knee and Elbow Involvement	0.052702	0.002994	0.002667	0.000000	1
X10	Scalp Involvement	0.049700	0.006986	0.000000	0.000000	1
X11	Family History	0.030020	0.005988	0.000000	0.000000	1
X12	Melanin Incontinence	0	0	0.000000	0	0
X13	Eosinophils in the Infiltrate	0	0	0	0	0
X14	PNL Infiltrate	0.039026	0.063872	0.000000	0.007289	1
X15	Fibrosis of the Papillary Dermis	0	0	0	0	0
X16	Exocytosis	0	0	0	0	0
X17	Acanthosis	0.069380	0.095808	0.136000	0.094752	1
X18	Hyperkeratosis	0.028019	0.009980	0.048000	0.021866	1
X19	Parakeratosis	0.065710	0.058882	0.049333	0.053936	1
X20	Clubbing of the Rete Ridges	0.069380	0.000000	0.005333	0.000000	1
X21	Elongation of the Rete Ridges	0.074716	0.009980	0.109333	0.000000	1
X22	Thinning of the Suprapapillary Epidermis	0.067045	0.000998	0.001333	0.000000	1
X23	Spongiform Pustule	0	0	0	0	0
X24	Munro Microabcess	0.036358	0.000000	0.000000	0.001458	1
X25	Focal Hypergranulosis	0	0	0	0	0
X26	Disappearance of the Granular Layer	0.035690	0.000000	0.000000	0.024781	1
X27	Vacuolisation and Damage of Basal Layer	0	0	0	0	0
X28	Spongiosis	0	0	0	0	0
X29	Saw-tooth Appearance of Retes	0	0	0	0	0
X30	Follicular Horn Plug	0	0	0	0	0
X31	Perifollicular Parakeratosis	0	0	0	0	0
X32	Inflammatory Monoluclear Inflitrate	0.063709	0.084830	0.106667	0.115160	1
X33	Band-like Infiltrate	0	0	0	0	0
		W_S=0.95	W_S=0.72	W_S=0.77	W_S=0.73	

Table 3. Self-test results of seborrheic dermatitis disease

Event Sets	Clinical and Histopathological Properties	Psoriasis	Seborrheic Dermatitis	Chronic Dermatitis	Rosacea	$P(X_k)$
X1	Erythema	0.076718	0.124751	0.086667	0.122449	1
X2	Scaling	0.073382	0.112774	0.061333	0.097668	1
X3	Definite Borders	0.070380	0.048902	0.053333	0.075802	1
X4	Itching	0.030354	0.094810	0.114667	0.030612	1
X5	Koebner Phenomenon	0	0	0	0	0
X6	Polygonal Papules	0	0	0	0	0
X7	Follicular Papules	0	0	0	0	0
X8	Oral Mucosal Involvement	0	0	0	0	0
X9	Knee and Elbow Involvement	0.052702	0.002994	0.002667	0.000000	1
X10	Scalp Involvement	0	0	0	0	0
X11	Family History	0.030020	0.005988	0.000000	0.000000	1
X12	Melanin Incontinence	0	0	0	0	0
X13	Eosinophils in the Infiltrate	0	0	0	0	0
X14	PNL Infiltrate	0.039026	0.063872	0.000000	0.007289	1
X15	Fibrosis of the Papillary Dermis	0	0	0	0	0
X16	Exocytosis	0.010007	0.118762	0.042667	0.138484	1
X17	Acanthosis	0.069380	0.095808	0.136000	0.094752	1
X18	Hyperkeratosis	0	0	0	0	0
X19	Parakeratosis	0.065710	0.058882	0.049333	0.053936	1
X20	Clubbing of the Rete Ridges	0	0	0	0	0
X21	Elongation of the Rete Ridges	0	0	0	0	0
X22	Thinning of the Suprapapillary Epidermis	0	0	0	0	0
X23	Spongiform Pustule	0	0	0	0	0
X24	Munro Microabcess	0	0	0	0	0
X25	Focal Hypergranulosis	0	0	0	0	0
X26	Disappearance of the Granular Layer	0	0	0	0	0
X27	Vacuolisation and Damage of Basal Layer	0	0	0	0	0
X28	Spongiosis	0.000000	0.116766	0.021333	0.131195	1
X29	Saw-tooth Appearance of Retes	0	0	0	0	0
X30	Follicular Horn Plug	0	0	0	0	0
X31	Perifollicular Parakeratosis	0	0	0	0	0
X32	Inflammatory Monoluclear Inflitrate	0.063709	0.084830	0.106667	0.115160	1
X33	Band-like Infiltrate	0	0	0	0	0
		W_S=0.58	W_S=0.93	W_S=0.67	W_S=0.87	

Table 4. Self-test results of chronic dermatitis disease

Event Sets	Clinical and Histopathological Properties	Psoriasis	Seborrheic Dermatitis	Chronic Dermatitis	Rosacea	$P(X_k)$
X1	Erythema	0.076718	0.124751	0.086667	0.122449	1
X2	Scaling	0	0	0	0	0
X3	Definite Borders	0.070380	0.048902	0.053333	0.075802	1
X4	Itching	0.030354	0.094810	0.114667	0.030612	1
X5	Koebner Phenomenon	0	0	0	0	0
X6	Polygonal Papules	0	0	0	0	0
X7	Follicular Papules	0	0	0	0	0
X8	Oral Mucosal Involvement	0	0	0	0	0
X9	Knee and Elbow Involvement	0	0	0	0	0
X10	Scalp Involvement	0	0	0	0	0
X11	Family History	0	0	0	0	0
X12	Melanin Incontinence	0	0	0	0	0
X13	Eosinophils in the Infiltrate	0	0	0	0	0
X14	PNL Infiltrate	0	0	0	0	0
X15	Fibrosis of the Papillary Dermis	0.000000	0.000000	0.137333	0.000000	1
X16	Exocytosis	0.010007	0.118762	0.042667	0.138484	1
X17	Acanthosis	0.069380	0.095808	0.136000	0.094752	1
X18	Hyperkeratosis	0	0	0	0	0
X19	Parakeratosis	0.065710	0.058882	0.049333	0.053936	1
X20	Clubbing of the Rete Ridges	0	0	0	0	0
X21	Elongation of the Rete Ridges	0.074716	0.009980	0.109333	0.000000	1
X22	Thinning of the Suprapapillary Epidermis	0	0	0	0	0
X23	Spongiform Pustule	0	0	0	0	0
X24	Munro Microabcess	0	0	0	0	0
X25	Focal Hypergranulosis	0	0	0	0	0
X26	Disappearance of the Granular Layer	0	0	0	0	0
X27	Vacuolisation and Damage of Basal Layer	0	0	0	0	0
X28	Spongiosis	0	0	0	0	0
X29	Saw-tooth Appearance of Retes	0	0	0	0	0
X30	Follicular Horn Plug	0	0	0	0	0
X31	Perifollicular Parakeratosis	0	0	0	0	0
X32	Inflammatory Monoluclear Inflitrate	0.063709	0.084830	0.106667	0.115160	1
X33	Band-like Infiltrate	0	0	0	0	0
		W_S=0.46	W_S=0.63	W_S=0.84	W_S=0.63	

Table 5. Self-test results of Rosacea disease

Event Sets	Clinical and Histopathological Properties	Psoriasis	Seborrheic Dermatitis	Chronic Dermatitis	Rosacea	$P(X_k)$
X1	Erythema	0.076718	0.124751	0.086667	0.122449	1
X2	Scaling	0.073382	0.112774	0.061333	0.097668	1
X3	Definite Borders	0.070380	0.048902	0.053333	0.075802	1
X4	Itching	0.030354	0.094810	0.114667	0.030612	1
X5	Koebner Phenomenon	0.022682	0.001996	0.000000	0.080175	1
X6	Polygonal Papules	0	0	0	0	0
X7	Follicular Papules	0	0	0	0	0
X8	Oral Mucosal Involvement	0	0	0	0	0
X9	Knee and Elbow Involvement	0	0	0	0	0
X10	Scalp Involvement	0	0	0	0	0
X11	Family History	0	0	0	0	0
X12	Melanin Incontinence	0	0	0	0	0
X13	Eosinophils in the Infiltrate	0	0	0	0	0
X14	PNL Infiltrate	0	0	0	0	0
X15	Fibrosis of the Papillary Dermis	0	0	0	0	0
X16	Exocytosis	0.010007	0.118762	0.042667	0.138484	1
X17	Acanthosis	0.069380	0.095808	0.136000	0.094752	1
X18	Hyperkeratosis	0	0	0	0	0
X19	Parakeratosis	0	0	0	0	0
X20	Clubbing of the Rete Ridges	0	0	0	0	0
X21	Elongation of the Rete Ridges	0	0	0	0	0
X22	Thinning of the Suprapapillary Epidermis	0	0	0	0	0
X23	Spongiform Pustule	0	0	0	0	0
X24	Munro Microabcess	0	0	0	0	0
X25	Focal Hypergranulosis	0	0	0	0	0
X26	Disappearance of the Granular Layer	0	0	0	0	0
X27	Vacuolisation and Damage of Basal Layer	0	0	0	0	0
X28	Spongiosis	0.000000	0.116766	0.021333	0.131195	1
X29	Saw-tooth Appearance of Retes	0	0.000000	0.000000	0	0
X30	Follicular Horn Plug	0	0.000998	0.001333	0	0
X31	Perifollicular Parakeratosis	0	0.000998	0.000000	0	0
X32	Inflammatory Monoluclear Inflitrate	0.063709	0.084830	0.106667	0.115160	1
X33	Band-like Infiltrate	0	0	0	0	0
		W_S=0.42	W_S= 0.80	W_S=0.62	W_S=0.89	

The results of the self test conducted for seborrheic dermatitis are given in Table 3. The results of the calculations were: $P(X_{S.Dermatitis})$=0.93, $P(X_{Rosacea})$=0.87, $P(X_{C.Dermatitis})$=0.67 and $P(X_{Psoriasis})$=0.58. The patient was diagnosed to have seborrheic dermatitis as the results indicated the highest probability rate for this disease.

The results of the self test conducted for chronic dermatitis are given in Table 4 and the results indicated that the patient had chronic dermatitis as this disease showed the highest probability rate. The results of the calculations were: $P(X_{C.Dermatitis})$=0.84, $P(X_{S.Dermatitis})$=0.63, $P(X_{Rosacea})$=0.63, and $P(X_{Psoriasis})$=0.46.

The results of the self test conducted for Rosacea are given in Table 5 and the results indicated that the patient had Rosacea as this disease showed the highest probability rate. The results of the calculations were: $P(X_{Rosacea})$=0.89 ,$P(X_{C.Dermatitis})$=0.62, $P(X_{S.Dermatitis})$=0.80, and $P(X_{Psoriasis})$=0.42.

Conclusion

Typical clinical prediction and prevention models provides the probability of an illness occurance or such as reccurence, stage and grade. With respect to knowledge lying behind, system can also support clinician in diagnose and treatment. In this work, we present an expert system called Symptom Based Clinical Decision Support Tool (SBCDST) for early diagnosis of erythemato-squamous diseases incorporating decisions made by Bayesian classification algorithm. Attributes are generated from the typical sign and symptoms of disorder. Based on our clinical results, tool yields 72%, 93%, 89% and 95% correct decisions on the Psoriasis, Seborrheic Dermatitis, Rosacea and Chronic dermatitis diseases respectively. In this kind of systems two major issues; usefulness and accuracy need to be addressed: In our presented study SBCDST addresses both major issues for family practitioners to prevent misdiagnose and mis-use of drugs. System also contains information and eutrophy suggestion pages for the patients having complaints similar to all four erythemato-squamous disease and provides guidance to the expert.

Peer-review: Externally peer-reviewed.

Conflict of Interest: The authors have no conflicts of interest to declare.

Financial Disclosure: The authors declared that this study has received no financial support.

References

1. E.D. Übeylı, I Güler, "Automatic detection of erythemato-squamous diseases using adaptive neuro-fuzzy inference systems", Comput Biol Med, vol. 35, no. 5, pp. 421-433, 2005. [CrossRef]
2. H.A. Guvenir, G. Demiro z, N. İlter, "Learning differential diagnosis of erythemato-squamous diseases using voting feature intervals", Artif Intell Med, vol. 13, pp. 147-165, 1998. [CrossRef]
3. R. O. Duda, P. E. Hart, D. G. Stork, "Pattern classification", John Wiley & Sons, 2012.
4. K. Fukunaga, "Introduction to statistical pattern recognition", Academic press, 2013.
5. S. P. Raychaudhuri, E. M. Farber, "The prevalence of psoriasis in the world", J Eur Acad Dermatol Venereol, vol. 15, no.1, pp. 16-17, Jan, 2001. [CrossRef]
6. L. Sagi, H. Trau, "The koebner phenomenon", Clin Dermatol, vol. 29, no.2, pp. 231-236, Apr, 2011. [CrossRef]
7. A. A. Pettey , R. Balkrishnan , S. R. Rapp , A. B. Fleischer , S. R. Feldman, "Patients with palmoplantar psoriasis have more physical disability and discomfort than patients with other forms of psoriasis: implications for clinical practice", J Am Acad Dermatol vol. 49. No. 2, pp. 271-275., Aug, 2003. [CrossRef]
8. S. P. Raychaudhuri, E. M. Farber, "The prevalence of psoriasis in the world." J Eur Acad Dermatol Venereol vol. 15, no. 1, pp. 16-17, Jan, 2001. [CrossRef]
9. C. O. McCall, "Psoriasis: Clinical features and pathology", AJSP: Reviews & Reports, vol. 16, no. 1, pp. 2-9, 2011. [CrossRef]
10. A. K. Gupta, R. Bluhm, "Seborrheic dermatitis", J Eur Acad Dermatol Venereol, vol. 18, no.1, pp. 13-26, Jan, 2004. [CrossRef]
11. R. A. Schwartz., A. C. Janusz, C. K. Janniger, "Seborrheic dermatitis: an overview", Am Fam Physician, vol. 74, no.1, pp. 125-130, Jul, 2006.
12. P. Milde , E. Hölzle, N. Neumann, P. Lehmann, U. Trautvetter, G. Plewig, "Chronic actinic dermatitis. Concept and case examples", Hautarzt, vol. 42, vol.10, pp. 617-622, Oct, 1991.
13. İ.Ü. Cerrahpaşa Tıp Fakültesi Sürekli Tıp Eğitimi Etkinlikleri Cilt Hastalıkları ve Yara Bakımı Sempozyumu 18-19 Ekim 2001, İstanbul, s. 57-59 Sürekli Tıp Eğitimi Etkinlikleri İ.Ü. Cerrahpaşa Tıp Fakültesi Sürekli Tıp Eğitimi Komisyonu Atopik Dermatit Prof. Dr. Oya Oğuz 10. http://turkdermatoloji.org.tr/public/media/hasta_bilgilendirme/Roza.pdf Access date: 12.10.2016.
14. Roza Hastalığı Bilgilendirme Broşürü, Available from: http://turkdermatoloji.org.tr/public/media/hasta_bilgilendirme/Roza.pdf.
15. E. Karakoç Aydıner, S. Barış, C. Özdemir, "Atopic Dermatitis and Diagnostic Tests", Turkiye Klinikleri J Dermatol-Special Topics vol. 4, no. 2, pp. 8-12, 2011.
16. F. S. Larsen, J. M. Hanifin, "Epidemiology of atopic dermatitis", Immunol Allergy Clin North Am vol. 22, no. 1, pp. 1-24, 2002. [CrossRef]
17. I. Z. Gökbay, S. L. Karaman, S. Yarman, B. S. Yarman, "An Intelligent Decision Support Tool for Early Diagnosis of Functional Pituitary Adenomas", TWMS J App Eng Math vol. 5, no. 2, pp. 169-187, 2015.
18. H. A. Güvenir, G. Demiröz, N. Ilter, "Learning differential diagnosis of erythemato-squamous diseases using voting feature intervals", Artif Intell Med, vol. 13, no. 3, pp.147-165, Jul, 1998.
19. A. N. Ünal, B. S. B. Yarman, "Milli Güç Unsurlarının Belirlenmesinde Siber Uzay Faktörü", in 7th International Conference on Information Security and Cryptology, İstanbul, 17-18 Oct, 2014.

İnci Zaim Gökbay, graduated from the Department of Electronics Engineering, Engineering Faculty, Işık University, in 2002, the M.S. degree with high honor from the Department of Electical and Electronics Engineering, Engineering Faculty, Bahcesehir University, in 2007 and Ph.D. degree in Biomedical Engineering from the Institute of Science, Istanbul University, in 2013. She was a Research and Teaching Assistant in the Department of Electrical and Electronics Engineering from 2004 to 2009, Lecturer in Vocational School from 2009 to 2014 in Bahcesehir University. She has been an Assistant Professor in the Department of Informatics, Istanbul University since 2014. She coordinated projects for handicapped individuals; Un-Handicapped House, Electronical Ramp Inspection System, My Colored Wheels, 2009, 2010 respectively. She has also been academic advisor for "Enhancing Employment Oppurtunities of Disabled People in EU through The Improvement of Their Competencies" EU Project in 2011. She is the general coordinator of the "A Child for Life, Life for a Child" project founded by Istanbul Development Agency (ISTKA). Her research interest covers decision support systems, clinical decision support systems, machine learning, biological image processing.

Zeynep Beyza Zileli was born in Istanbul, Turkey in 1989. She graduated from Department of Genetics and Bioengineering, Engineering Faculty, Fatih University, in 2011. She received her M.Sc degree in Biomedical Engineering from Fatih University in 2013. Her research interests cover biomedical signal processing, machine learning and decision support systems.

Pelin Sarı was born in Kırklareli,Turkey in 1984.She received her bachelor degree in Biology in 2006 from Marmara University, M.S. degree in Biomedical Engineering in 2010 from Istanbul University, started PhD education in Biomedical Engineering at Istanbul University in 2015 and now she is in the thesis stage.Since 2010 she has been working as an Biomedical Specialist at Istanbul University Cerrahpasa Medical Faculty, Biomedical and Clinical Engineering Unit.

Türker Togay Aksoy is currently working is İstanbul Aydın Üniversity. He is PhD candidate is department of Biomedical Engineering at İstanbul University-Cerrahpaşa. His research interests include biomedical signal processing and robotic control. He has made variety of presentations at national and international congress.

Sıddık Yarman received his BSc Degree from Technical University of Istanbul in 1974; MSc. Degree from Stevens Institute of Technology (1977), Hoboken, N.J., USA, and Ph.D. Degree from Cornell University (1982), Ithaca, NY, USA. He was a Member of Technical Staff at General David Sarnoff Microwave Technology and Research Center, in Princeton, NJ, USA. He served as professor and administrator at various Universities: Anadolu University, Middle East Technical University, Istanbul University, Isik University of Turkey; Ruhr University of Germany, Tokyo Institute of Technology of Japan, Wuhan Technology University of China. He is one of the founders of Savronik Group of Companies and recently serves as the Chairman of the Board of Directors. He was the founding president of Isik University (1996-2004). Currently serves as the Chairman of Board of Trustees. He published numerous papers in the field of Microwave Engineering, Circuit and Systems, Signal Processing, Mathematical Modeling and Decision Making. He has published 4 books: Design of Ultra - Wideband Antenna Matching Networks by Springer (2008), Design of Ultra - Wideband Power Transfer Networks by Wiley (2010), Intelligence Based Decision Making by Nobel Press of Turkey (2014) and He is one of the co-author of the book titled "Broadband Microwave and RF Power Amplifiers" by CRC (November 2015). He holds 4 US and 9 Turkish Patents. He was the recipient of Young Turkish Scientist Award (1986), Technology Award (1987) of Scientific and Research Council of Turkey. He is a member of New York Academy of Science (1994), selected as the Man of the year in Science and Technology of Cambridge Biography (1999). He is a Fellow of IEEE; Alexander Von Humboldt Fellow and Salzburg Fellow of USIS.

İSTANBUL UNIVERSITY
CERRAHPAŞA

RESEARCH ARTICLE
Electrica 2019; 19(1): 59-64

A New Formula for Hydrogen Consumption in Hybrid Systems Based on Fuel Cell Current Gradient and Peak Value

Yasin Özçelep, Gürcan Sarı, Ayten Kuntman

Department of Electrical and Electronics Engineering, İstanbul University-Cerrahpaşa, İstanbul, Turkey

Cite this article as: Özçelep Y, Sarı G, Kuntman A. A New Formula for Hydrogen Consumption in Hybrid Systems Based on Fuel Cell Current Gradient and Peak Value. *Electrica*, 2019; 19(1): 59-64.

ABSTRACT

In the study, we proposed a new formula for the hydrogen consumption of fuel cell under non-constant current behavior. We used supercapacitors as auxiliary energy source to form a hybrid system and change the current behavior of the fuel cell. We performed hybrid system tests for different supercapacitor values. We extracted the fuel cell current, voltage, hydrogen consumption for each configuration. We compared the measured values and expected values from known equations. We see that, results from hydrogen consumption equations does not match the hybrid system hydrogen consumption. Finally, we proposed a new formula for hydrogen consumption including the current gradient and current peak value for hybrid systems.

Keywords: Hydrogen fuel cell, hydrogen consumption, hybrid systems

Introduction

Due to advantages as low temperature, high energy density, small size and environment friendly clean energy; proton exchange membrane fuel cells (PEMFC) are considered to be one of the promising energy sources for the hydrogen fuel cell powered vehicles [1-4]. Besides the advantages, PEMFCs have some electrical disadvantages as poor dynamic response, low power density [5-7]. These disadvantages cause increase in hydrogen consumption and consumption related efficiency of the PEMFC. To suppress the effects of disadvantages, a hybrid powertrain is formed by using the PEMFCs with an auxiliary power source [5]. To form a hybrid powertrain mostly batteries and supercapacitors are used as an auxiliary power source [8-11].

Because of the purpose of forming hybrid powertrain reducing the hydrogen consumption, the hydrogen consumption, should be calculated in the design stage of the powertrain. Thus, the best solution can be achieved considering the size and the cost of the powertrain. The mathematical equations proposed by the authors [12-15] to calculate the hydrogen consumption of the fuel cell stack. The molar hydrogen consumption of the fuel cell is given in equation 1 [12-13];

$$n = \frac{I.N}{2F} \tag{1}$$

Here, I is the current and N is the cell number of the fuel cell stack. F is faraday constant, approximately 9.65 x 10^4 $Cmol^{-1}$. And n gives the molar hydrogen consumption. Using equation (2) hydrogen consumption in lpm (liter per minutes) can be calculated [14-15];

$$lpm = 0.00735xIxNxS_{H_2} \tag{2}$$

Here, I is the current and N is the cell number of the fuel cell stack. S_{H2} is stoichiometric ratio for hydrogen.

Corresponding Author:
Yasin Özçelep

E-mail:
ycelep@istanbul.edu.tr

Received: 14.08.2018

Accepted: 20.11.2018

DOI: 10.26650/electrica.2019.18013

In both equations, the consumption formula is dependent the time-independent value of the current. The equations do not contain how the current reaches this value. The current signal of the fuel cell stack will be changed by auxiliary power source, while the reducing hydrogen consumption and these equations cannot be used for calculating the hydrogen consumption.

In the study, we formed a hybrid powertrain using supercapacitors as auxiliary power source by connecting the fuel cell and supercapacitors parallel to each other. We performed our tests on a prototype hydrogen powered vehicle. We used different supercapacitor values in repeating tests and recorded the voltage, current and hydrogen consumption values during each test. Using measured results, we proposed a new hydrogen consumption formula including the fuel cell current gradient and peak value. The performed tests also provided us to determine the best configuration considering the hydrogen consumption.

Material and Method

We performed test in a prototype hydrogen powered vehicle. The system components are given in Table 1.

Table 1. System components

Description	Specification
Fuel Cell	700W, 40 cells, 37V/25A
Electrical Motor	500W, nominal voltage 48V
Supercapacitor	Each one 2.7V, 360F; in each test 18F, 36F and 54F supercapacitor banks are used
Prototype Vehicle	200kg with driver

W: watt; A: ampere; V: volt; F: Farad; kg: kilogram

Firstly, we performed a test without using supercapacitors for reference values. After reference measurements, we formed hybrid powertrain as in Figure 1.

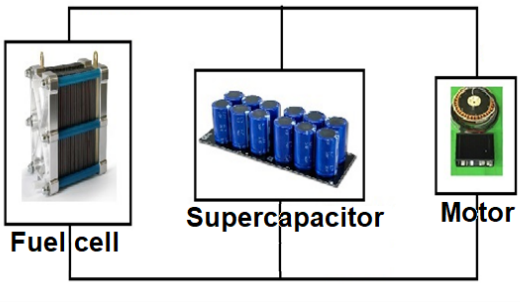

Figure 1. The hybrid powertrain performed in the tests

We performed same tests for supercapacitor values 18F, 36F and 54F. We measured the hydrogen consumption using Red-y flow meter.

Results

Figure 2 presents the fuel cell currents in hybrid powertrain with different supercapacitor values.

As seen in Figure 2 the peak value and gradient of the current curve changes depend on the supercapacitor value. The peak value and gradient of fuel cell current decrease with the increasing supercapacitor value. The hydrogen consumption of fuel cell is measured 2.85L for test without using supercapacitors and for hybrid power train 2.54L, 2.45L and 2.28L, for 18F,36F,54F respectively.

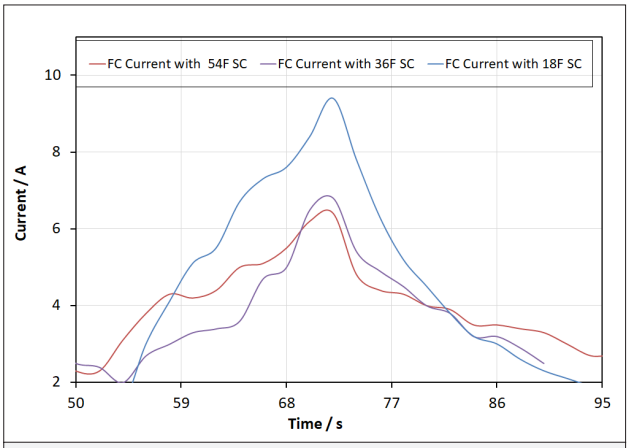

Figure 2. The fuel cell current for different supercapacitor values

After these results, we investigated relation between the measured hydrogen consumption and expected hydrogen consumption from equations current value directly determines the hydrogen consumption.

Firstly, we extracted peak current and hydrogen consumption curve (Figure 3) and see that, while peak current decreased around 60%, hydrogen consumption decreased only 20%.

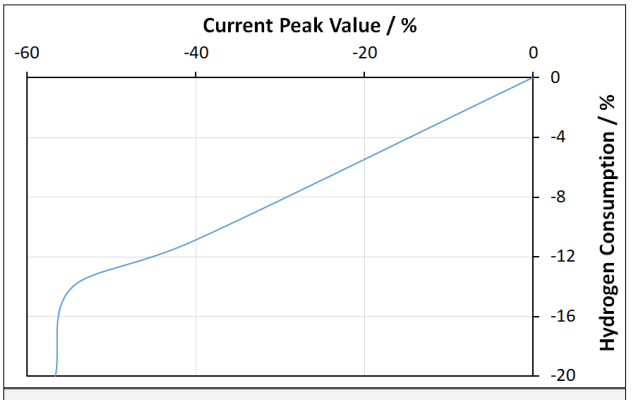

Figure 3. Hydrogen consumption and fuel cell peak current relation

Sure, the fuel cell does not deliver the peak current constantly during operation because of hybridization with supercapacitors, the conflict between measured and expected value can make sense. To remove the conflict and make the equations useful, we calculated the average value of the current by fitting mathematical equations to current curves. The hydrogen consumption and average current curve is presented in Figure 4. As seen in Figure 4 while the average current decreases nearly 70%, the hydrogen consumption is only decreased 20%. Here, there is a need for a new formula for non-constant currents which includes the gradient of current. We proposed a new formula which includes both peak value of the current and the gradient of the current.

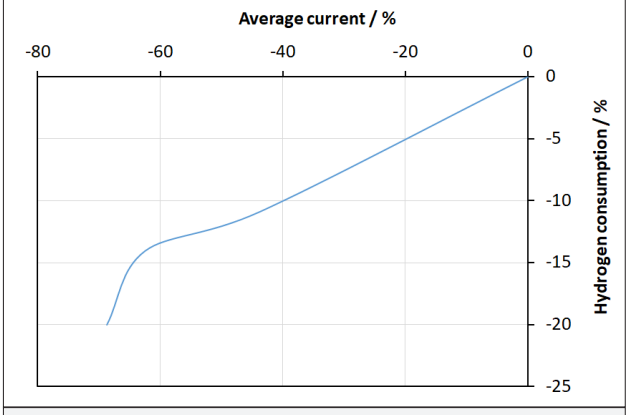

Figure 4. Hydrogen consumption and fuel cell average current relation

To form a new formula, we normalized the hydrogen consumption according to peak value of current and presented in Figure 5.

The mathematical equation of the curve in Figure 5 is expressed in equation 3.

$$H_{ncp} = -0.5062 x I_p^{-0.767} \quad (3)$$

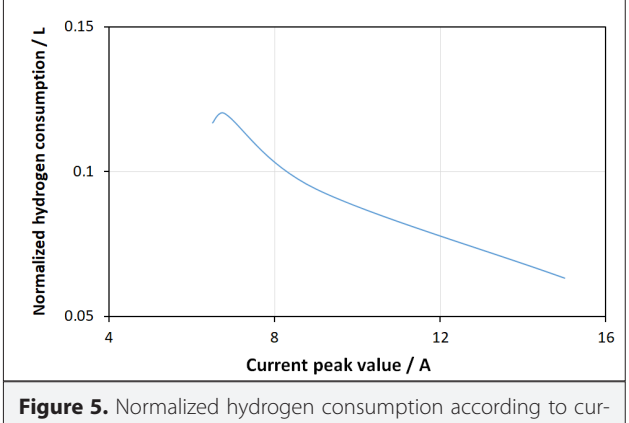

Figure 5. Normalized hydrogen consumption according to current peak value

Here, H_{ncp} stands for normalize hydrogen consumption according to peak value of the current and I_p is the peak current value.

We attributed the remaining hydrogen consumption to current gradient induced consumption and presented the consumption- current gradient curve in Figure 6.

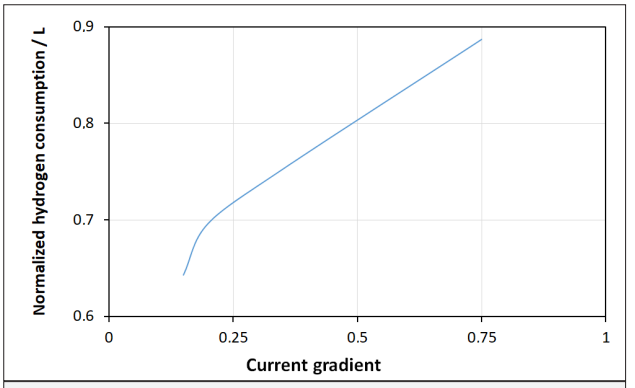

Figure 6. Normalized hydrogen consumption according to current gradient

The mathematical equation of the curve in Figure 6 is expressed in equation 4.

$$H_{ncg} = 0.9334 x G^{0.1924} \quad (4)$$

Here, H_{ncg} stands for normalize hydrogen consumption according to current gradient and G is the current gradient.

After determining the normalized consumptions, equation 3 and equation 4 combined as in equation 5 to form hydrogen consumption.

$$H_C = k_1 x (I_p x G)^{k_2} \quad (5)$$

Here, H_c stands for hydrogen consumption (L), k_1 (LA^{-1}) and k_2 are the constants. I_p is the peak value and G is the gradient of the current. In equation 5, k_1 and k_2 are 0.7755 and 0.0837; respectively.

To validate the results of curve fitting method, we compared the measured and calculated results as seen in Figure 7. The calculated results are in a good agreement with measured results.

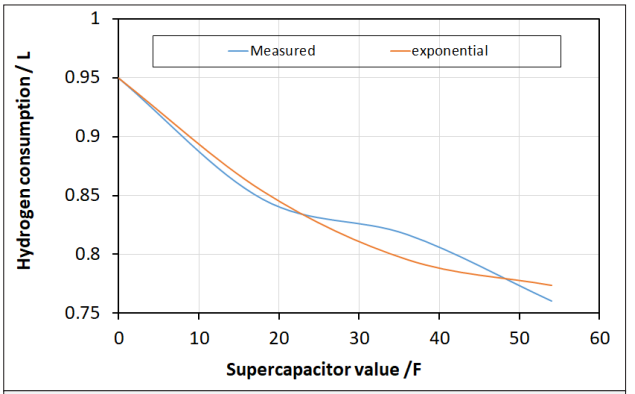

Figure 7. Comparison of measured and calculated results

Because of the peak value and the current gradient are change with supercapacitors we extracted the peak value and current gradient changes with supercapacitors. The peak current-supercapacitor curve is seen in Figure 8.

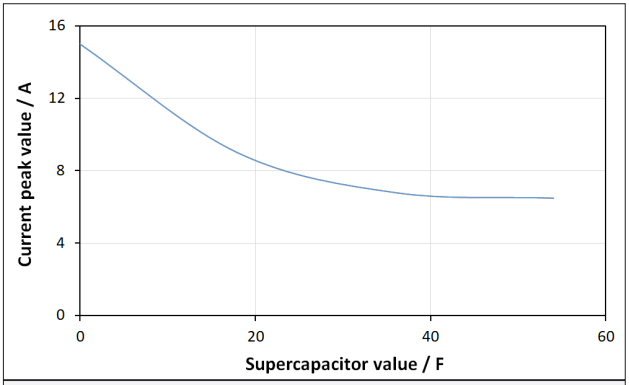

Figure 8. Current peak value change with the supercapacitors

We formulated the supercapacitor induced change in peak current as in equation 6, using curve fitting methods.

$$I_p = 21.52xC^{-0,308} \quad (6)$$

Here, I_p is the peak current and C is the supercapacitor value.

The current gradient-supercapacitor curve is seen in Figure 9.

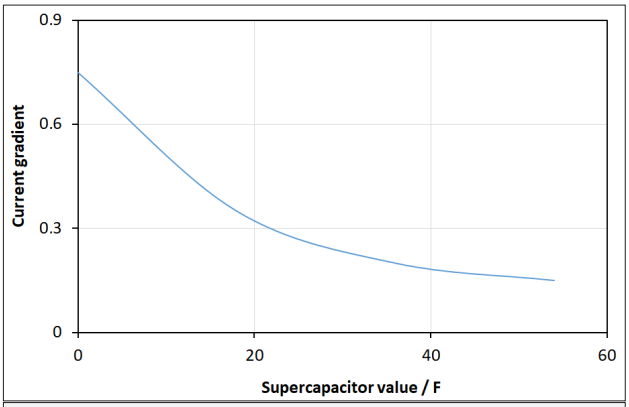

Figure 9. Current gradient change with the supercapacitors

We formulated the supercapacitor induced change in current gradient as in equation 7, using curve fitting methods.

$$G = 3.27xC^{-0,775} \quad (7)$$

Here, G is the current gradient and C is the supercapacitor value.

If equation 6 and 7 put into proposed hydrogen consumption equation, the supercapacitor effect on hydrogen consumption can be extracted for hybrid systems.

Conclusion

In the study, we proposed a new formula for the hydrogen consumption for hybrid systems. We used supercapacitors as auxiliary energy source to change the current behavior of the fuel cell. We performed tests on hydrogen powered vehicle for different supercapacitor values and for each test we extracted different current behavior. Using experimental results, we formed a new formula in exponential form, including peak current and current gradient. Seen in normalized hydrogen consumption curves, using supercapacitors decreases the peak current but increases the normalized hydrogen consumption. The increasing supercapacitor value decreases both the current gradient and hydrogen consumption. A new hydrogen consumption formula for hybrid systems is proposed which includes the supercapacitor induced peak current and current gradient changes. This study helps designers to find the best solution for size and the cost of the powertrain considering the hydrogen consumption at design stage.

Peer-review: Externally peer-reviewed.

Conflict of Interest: The authors have no conflicts of interest to declare.

Financial Disclosure: The authors declared that this study has received no financial support.

References

1. Y. Hou, C. Shen, D. Hao, Y. Liu, H. Wang, "A dynamic model for hydrogen consumption of fuel cell stacks considering the effects of hydrogen purge operation", Renew Energy vol. 62, pp. 672-678, 2014. [CrossRef]
2. M. Uzunoglu, M. S. Alam, "Dynamic modeling, design, and simulation of a combined PEM fuel cell and ultracapacitor system for stand-alone residential applications", IEEE Trans Energy Convers, vol. 21, pp. 767-775, 2006. [CrossRef]
3. D. Shin, K. Lee, N. Chang, "Fuel economy analysis of fuel cell and supercapacitor hybrid systems", Int J Hydrogen Energ, vol. 41, pp. 1381-1390, 2016. [CrossRef]
4. P. Ahmadi, E. Kjeang. "Realistic simulation of fuel economy and life cycle metrics for hydrogen fuel cell vehicles", Int J Energy Res. Vol. 41, pp. 714-727, 2017. [CrossRef]
5. Y. Hames, K. Kaya, E. Baltacioglu, A. Turksoy, "Analysis of the control strategies for fuel saving in the hydrogen fuel cell vehicles", Int J Hydrogen Energ, vol. 43, no. 23, pp. 10810-10821, June 2018. [CrossRef]
6. G. Sarı, Y. Özçelep, A. Kuntman, "On the optimum powertrain configuration of fuel cell powered vehicle for minimum hydrogen consumption", 9th International Conference on Electrical and Electronics Engineering (ELECO) Turkey, 2015, pp. 379-382. [CrossRef]
7. C. Kunusch, F. Castaños, "Extremum seeking algorithms for minimal hydrogen consumption in PEM fuel cells", American Control Conference (ACC), 2013, pp. 1144-1149. [CrossRef]
8. B. Morin, D. V. Laethem, C. Turpin, O. Rallières, S. Astier, A. Jaafar, O. Verdu, M. Plantevi, V. Chaudron, "Direct hybridization fuel cell-ultracapacitors", Fuel Cells Vol 14, pp. 500-5007, 2014. [CrossRef]
9. H. Fathabadi, "Novel fuel cell/battery/supercapacitor hybrid power source for fuel cell hybrid electric vehicles", Energy, vol. 143, pp. 467-477, 2018. [CrossRef]

10. Q Li, W. Chen, Y. Li, S Liu, J. Huang, "Energy management strategy for fuel cell/battery/ultracapacitor hybrid vehicle based on fuzzy logic", Int J Elec Power, vol. 43, pp. 514-525, 2012. [CrossRef]
11. M. Uzunoglu, M. S. Alam, "Dynamic modeling, design and simulation of a PEM fuel cell/ultra-capacitor hybrid system for vehicular applications", Energ Convers Manage, vol. 48, 1544-1553, 2007. [CrossRef]
12. A. Kabza, "Fuel Cell Formulary, can be found under" http://pemfc.de/FCF_A4.pdf, 2016.
13. J. Larminie, A. Dicks, "Fuel Cell Systems Explained", John Wiley & Sons, 2003. [CrossRef]
14. M.R.B. Mustaffa, W.A.N.B.W. Mohamed, R.B. Atan, "Analytical approach to predict hydrogen consumption of a lightweight PEM fuel cell vehicle", IEEE International Conference on Control System, Computing and Engineering (ICCSCE), 2012, pp. 489-494. [CrossRef]
15. F. Barbir, "PEM fuel cells: Theory and Practice", Elsevier Academic Press, California, USA, 2005.

Yasin Özçelep received the B.Sc., M.Sc. and PhD. degrees from Electrical and Electronics. Department, Istanbul University, Istanbul, Turkey, in 2002, 2004 and 2009, respectively. He is working as Associate Professor in same department. His research interests are hydrogen fuel cells, hydrogen powered vehicles, semiconductor device and circuit reliability, reliability modeling and electronic circuits.

Gürcan Sarı received the B.Sc. and M.Sc. degrees from Electrical and Electronics Department, Istanbul University, Istanbul, Turkey, in 2014 and 2017, respectively. He was the team leader of Istanbul university Hydrogen Powered Vehicle (HIDROIST).

Ayten Kuntman received her M.Sc. degree from Istanbul University in 1979 and her Ph.D. degree from Istanbul Technical University in 1989, respectively. In 1980 she joined the Electronics and Communication Engineering Department of Istanbul Technical University. From 1995 to 2001 she was an associate professor of Electrical Power Systems in the Electrical and Electronics Engineering Department of Istanbul University. Since 2001 she is a professor of Electrical Power Systems in the same department. Her research interest include dielectric properties of polymers, semiconductors, aging of cable polymers, microelectronics technologies, hydrogen fuel cells, thermodinamic properties of polymers and reliability of materials. Dr. Kuntman has authored many publications on polymers, semiconductors and microelectronics technologies.

İSTANBUL UNIVERSITY
CERRAHPAŞA

RESEARCH ARTICLE
Electrica 2019; 19(1): 65-71

Multifunctional Phototherapy Device Design

Mehmet Akşahin

Department of Biomedical Engineering, Başkent University, Ankara, Turkey

Cite this article as: Akşahin M. Multifunctional Phototherapy Device Design. *Electrica*, 2019; 19(1): 65-71.

ABSTRACT

Today, phototherapy devices are used to treat newborn jaundice. However, there are some cases that the commercial phototherapy devices are inadequate. Most of the device are controlled only at the certain interval that prevents instantaneous monitoring the newborn's vital parameters. For other cases, devices are one-way lighting. In addition, when the baby is taken away from the device, unnecessary lighting causes the decrease in LED's lifetime. In the scope of the study, intensive phototherapy device was developed to eliminate deficiencies that are mentioned above. Properties of the developed phototherapy device are; Automatic detection of newborn's presence, double-sided illumination, continuous monitoring with IP webcam, temperature measurement of the environment and also newborn's body temperature. The light intensity of the device was measured with a photometer as 28.6 μW/cm^2/nm that was obtained from 460nm wavelength LED illumination in both top and bottom in accordance with the American Academy of Pediatrics (AAP) guideline.

Keywords: Neonatal Jaundice, Phototherapy, Multifunctional System Design and Control

Introduction

Fetal red blood cells (RBCs) are different from normal ones. These cells contain fetal Hemoglobin (HbF). Red blood cells lose their function and start to disintegrate in a short period after birth. Thus, RBC's that contain new type hemoglobin (HbA) begin to be produced. As a result of the disintegrated RBC's containing HbF, the excessive amount of bilirubin substance occurs as a by-product. In a healthy adult, liver transforms bilirubin in into a form to be thrown from the body [1]. However, liver function of newborn is not adequate to destroy the high amount of bilirubin. So, the bilirubin, which is needed to be thrown out of the body, starts to accumulate in the blood. Bilirubin has yellow-colored pigments. As a result of the excessive amount of bilirubin accumulation and penetration, the newborn's the skin and eyes to have a yellowish appearance. This condition is called the neonatal jaundice [2]. If the high level of bilirubin cannot be removed out of the newborn's body, it can be seen clinical consequences such as bilirubin encephalopathy, hearing loss and kernicterus [3]. In order to make non-conjugated bilirubin into water soluble form, phototherapy method is applied [4].

The phototherapy device which is used in the treatment of neonatal jaundice, is based on the principle that the conversion of the non-conjugated bilirubin that accumulated on the skin surface into a water-soluble form by applying light in the visible region (blue light~460 nm). This non-invasive method is used and accepted by pediatricians for the treatment of neonatal jaundice [5]. The efficiency of phototherapy treatment depends on the factors like the surface area of the newborn (as the surface area increases, the total bilirubin decline rate increases), the spectral properties (460±10 nm wavelength) and the irradiation (brightness, light intensity: body surface area per square meter) of the light source (The current AAP guidelines recommends a light intensity of at least 30 μW/cm^2/nm for dense phototherapy under blue light and for the largest surface area), the distance between the light source and the newborn (The distance is at least 10 cm, provided that the newborn's body temperature is constantly monitored.), the type of light source, the thickness and pigmentation of the skin, the total

Corresponding Author:
Mehmet Akşahin

E-mail:
maksahin@gmail.com

Received: 06.09.2018

Accepted: 18.12.2018

DOI: 10.26650/electrica.2019.18022

bilirubin level at the beginning of treatment and the duration of phototherapy [3, 5-10].

In this study, a completely original conceptual phototherapy device was designed and the prototype was produced in order to eliminate the deficiencies of the existing commercial devices. In the design phase, it is aimed to obtain intensive phototherapy by providing higher light efficiency than the existing commercial devices have. In this context, in order to increase the light efficiency of the device, light sources are placed both of on the top and bottom covers of the device. Moreover, detection of the newborn's existence in the device, the load cells are used. In addition, temperature measurements are made and an IP webcam can be integrated into the system to assist in monitoring the newborn by both of the hospital staff and also the parents.

System Design

The overall design of the phototherapy system is as shown in Figure 1. In the design, a microcontroller is used for controlling the sensors (heat and weight) in the hammock and the image formed on the IP webcam. Besides, the control of the LED's in the lighting array operation and the drive circuit are also provided with a microcontroller.

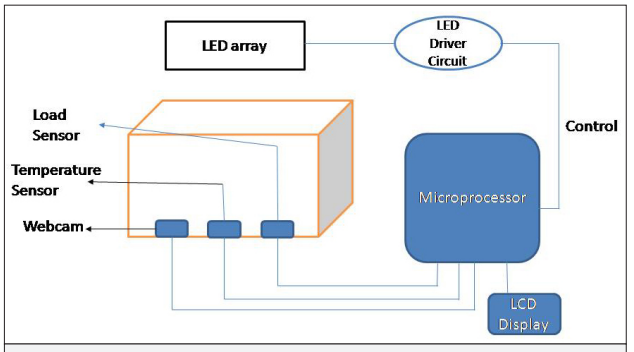

Figure 1. General block diagram of the device

Lighting Calculations

The luminous flux (lumen) is the amount of light that is delivered by a light source at the unit time and is calculated according to Equation 1 [11].

$$\phi = 4*\pi*I \quad (1)$$

The luminous intensity (lux) is the intensity of light falling on the unit surface and is calculated according to Equation 2 [11].

$$E=\Phi/A = 4*\pi*I/4*\pi*r^2 = I/r^2 \quad (2)$$

Light intensity is a parameter that also depends on the distance. The distance between the light source and target area is determined according to Equation 3 [11].

$$I=P/4\pi r^2 \quad (3)$$

In this equation, "P" is the maximum power of the light source to be used and "r" is the distance between the light source and the target area. For the top and bottom illumination, the distance between light source and the hammock of the device is adjusted by the inverse square law as described in Equation 4 [11].

$$\frac{I_1}{I_2}=\frac{d_2^2}{d_1^2} \quad (4)$$

Here, "I" represents the luminous intensity at a certain distance and "d" represents distance between the point where the intensity is known and the source. The current AAP guidelines recommend that the light intensity of blue light should be at least 30 μW/cm²/nm for the largest surface area for intensive phototherapy [3]. The distance between the light source to the infant is also calculated taking into account the AAP recommendation.

One of the most significant purposes of the preliminary design is to achieve a homogeneous distribution of light. For this purpose, the quantity and power of light sources must be determined correctly. In preliminary studies DIALuxevo simulation program is used for these calculations and the obtained illumination results are shown in Figure 2. Based on the obtained results, a light intensity of approximately 16μW/cm²/nm was obtained with a 5-row, 7.5W (240 Lumens) strip LED (for one lighting side of the device). In this case the total light intensity for the upper and lower side of the design was set at a minimum of 32 μW/cm²/nm.

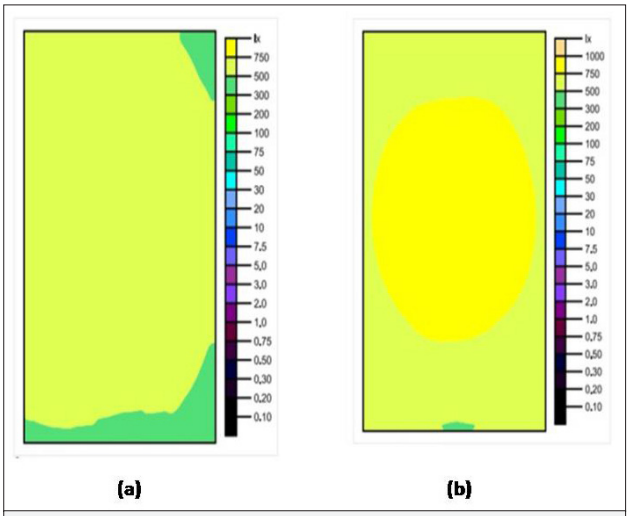

Figure 2. a-b. The surface area of the 4 Strip LEDs in lux units (Scale 1:10; vertical light surface; mean: 590lx; min: 395lx; max: 703lx; min/mean: 0.673; min/max:0.565) (a). The surface area of the 5 Strip LEDs in lux units (Scale 1:10; vertical light surface; mean:733lx; min: 491lx; max: 855lx; min/mean: 0.670; min/max:0.574) (b)

Light source and Circuit design

Power LEDs which have high lumen values are widely used in the lighting industry. In this study, Power Led's are used as a light source by virtue of the preliminary findings. To run the LED's with microprocessor, there must be an appropriate driver circuit and a power source. Figure 3 shows the block diagram of the LED system.

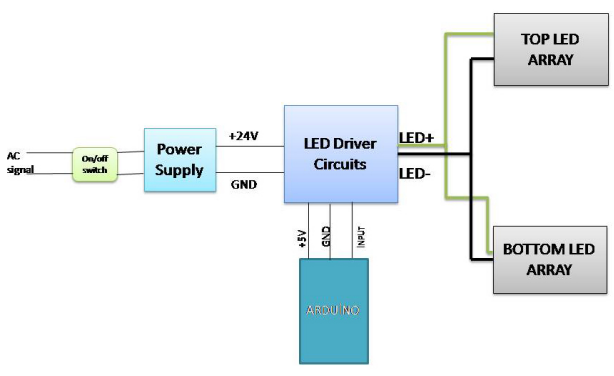

Figure 3. The block diagram of the LED System

The current levels of PowerLEDs are much higher than standard 5mm diameter LEDs. It is required that 3.2 V for each PowerLED. By this, six of 460nm wave PowerLED's are series connected to draw about 350mA current. The designed LED driver circuit is drawn and simulated in the Proteus program. The circuit that used to drive the LEDs is shown in Figure 4.

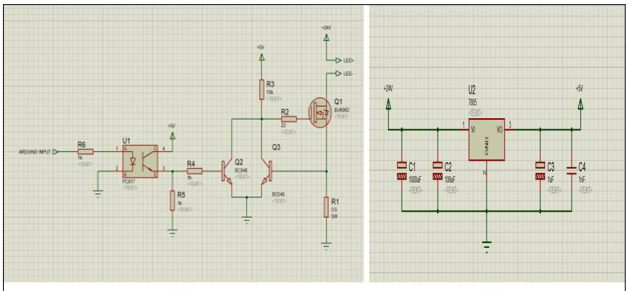

Figure 4. a-b. LED driver circuit (a) and voltage regulator (b)

In order to reduce the cost and the power consumption of the device, a 45˚ lens was used to not only increase the focusing but also decrease in LED number that determined at the preliminary work. In the designed circuit, a total of 60 PowerLEDs were used as 30 on the top and 30 on the bottom. Six of them were formed in parallel with 5 parallel strips connected in series. 6x5 matrix was created on this count. The current in a single plate is 1.75 A and the total current from two plates is 3.5 A. The LED array of the device is shown in Figure 5.

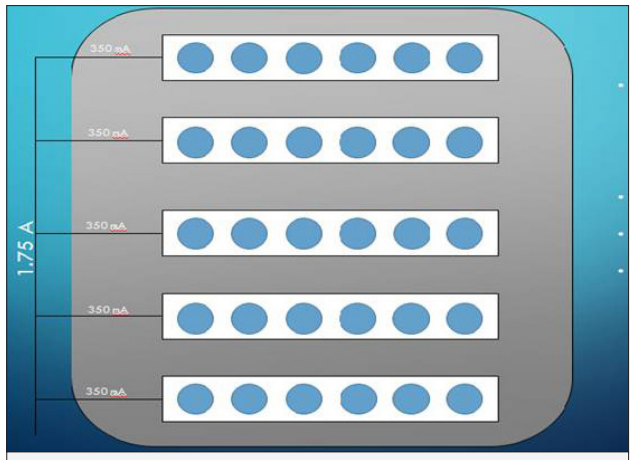

Figure 5. PowerLED array

Control Circuit Design

The control panel of the device was designed with a microprocessor-based circuit. The simulation of the circuit was made with Arduino Mega 2560 microprocessor card in Proteus shown in Figure 6. In the project, a load sensor is used to detect the newborn's existence in the device. For this purpose, a load cell has been integrated into the device control circuit and informed whether or not the baby is in the hammock has been determined through this sensor. The Load Cell generates a voltage output proportional to the pressure applied to it. The Load Cell's output is transferred to the Arduino board via the HX711 amplifier. When the weight information reached to the system, it is operated automatically.

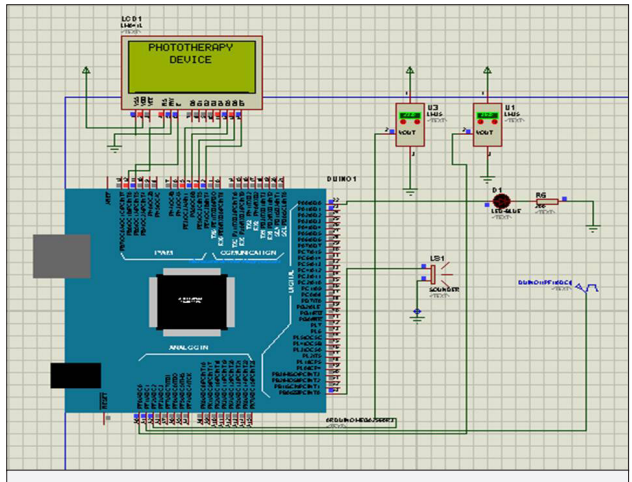

Figure 6. Device circuit

Instantaneous measurement of the ambient temperature was made with the digital temperature sensor DS18B20. The device uses a 20x4 LCD display to initiate the therapy, to adjust time and also to show warning information, ambient temperature and duration information. A buzzer has been used as an alert for

the situations where the device should give a warning during therapy. The duration of the therapy is set using the UP/DOWN buttons on the control panel and shown on the display as unit of minutes. At the end of the duration, the device gives audible and written warnings. In cases where the baby needs to be taken from the device during the therapy, the system goes into the 'pause' mode as soon as the baby is taken from the device. If the baby is returned to the device within 2 minutes, the system continues to therapy. Otherwise, the device is automatically turned off and gives an audible and written warning. The body temperature measurement system was provided by integrating the circuit of an IR thermometer, which was supplied from the market, into the Arduino circuit. In this way, the relevant hospital staff can routinely make a contactless measure of the infant's body temperature with the temperature measurement key located on the control panel.

The housing of the device is designed and scribed in the SolidWorks program (Figure 7).

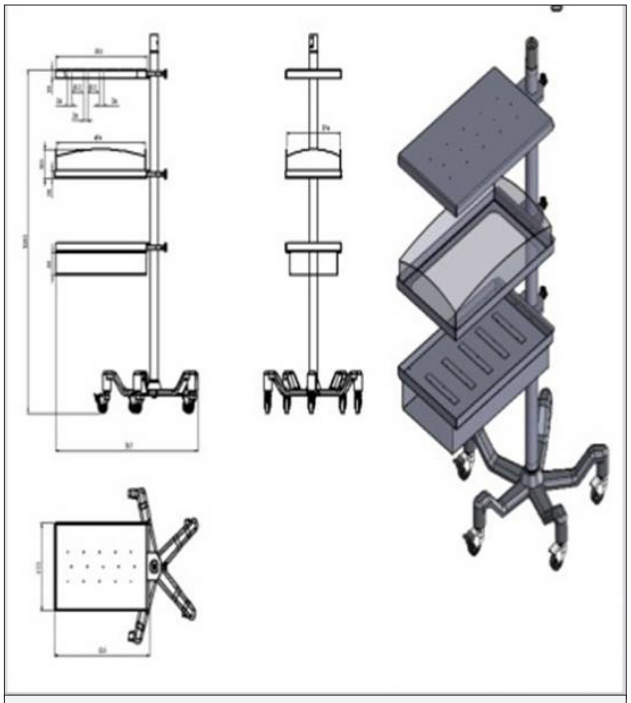

Figure 7. The housing of the device

Results

In this study, a phototherapy device that is used in the treatment of newborn jaundice was developed and a prototype was produced. The light intensity of the device was measured with a photometer and according to the AAP guide, light intensity of 28.6 μW/cm^2/nm was obtained by LED (460 nm wavelength) illumination in both top and bottom.

The control and driver systems designed in the scope of the study are shown in Figure 8. The produced phototherapy device is shown in Figure 9.

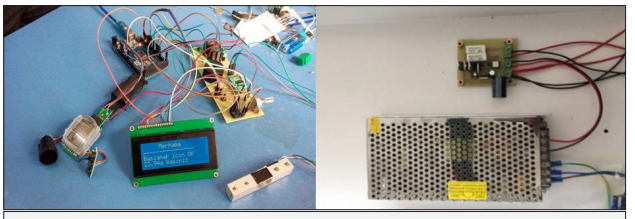

Figure 8. The control and driver systems

Figure 9. Phototherapy device

Discussion

The device prototype is designed as a double-sided lighting device. Since this will provide more effective treatment, it is thought to be able to shorten the duration and thence, increase the efficiency of the treatment.

With the use of a weight sensor that is not available in existing commercial systems, it is determined whether or not the baby is in the device and the system is automatically shut down when it is unnecessary. Thus, the lifetime of the light source will be prolonged and the efficiency of the device will be improved.

The biggest risk at the new born may encounter during phototherapy is eye damage, which is likely to result of the shift of the eye band. In order to prevent this condition, eyes are controlled at 4-6 hours intervals. Having such a long period of control is a particularly disturbing situation for parents. By the integration of The IP WEB cam, it is ensured that the baby can be monitored by both parents and health staff.

The developed system was compared with the similar commercial products in the market. Comparison is shown in Table 1. According to Table 1, the features of the presented phototherapy device are much more [12, 13, 14, 15]. The power consumption of the developed device is very low, especially in comparison to its two-sided illuminating commercial products. Due to the use of power led, the system has up to 50 000 hours of LED life [16]. However, as the energy consumption will be minimal due to the use of the weight sensor, the LED life of the developed device will be higher than its equivalent.

Table 1. Properties of presented and commercial phototherapy devices in market

Commercial Products	Technical Properties	Power Consumption	Cost
ERTUNÇ ÖZCAN BLUE ANGEL LED PHOTOTHERAPY DEVICE [12,13]	- 450-470 Nm Narrow Beam Emitting Light Emitting 24 Pcs Blue Led - Unilateral lighting - Focus light - Baby skin temperature monitoring (optional) - Up to 20,000 hours of LED life	45Watt	1000$
TENDE CAREBLUE-N LED PHOTOTHERAPY DEVICE [13]	- 460 Nm Narrow Beam Emitting Light Emitting 24 Pcs Blue Led - unilateral lighting - Up to 20,000 hours of LED life - Focus light	45Watt	1120$
TENDE BABYBLUE-N LED PHOTOTHERAPY DEVICE [13]	- 460 Nm Narrow Beam Emitting Light Emitting 24 Pcs Blue Led - unilateral lighting - Up to 20,000 hours of LED life - Focus light	45Watt	1000$
NOVOS BILISPHERE 360 LED PHOTOTHERAPY DEVICE [13]	- 420 - 480 Nm Narrow Beam Emitting Light Emitting 16 Pcs Led - double sided lighting - 20,000 hours of LED life	266Watt	5420$
OKUMAN BC 250 LCD LED PHOTOTHERAPY DEVICE [13]	- 16 Pcs Led - double sided lighting - Up to 50,000 hours of LED life	225Watt	4450$
OKUMAN BC 250 000 LED PHOTOTHERAPY DEVICE [13]	- 16 Pcs Led - double sided lighting - Up to 50,000 hours of LED life	225Watt	3550$
neoBLUECozy LED PHOTOTHERAPY DEVICE[14]	- 450-470 Nm Narrow Beam Emitting Light Emitting 24 Pcs Blue Led - unilateral lighting - Up to 20,000 hours of LED life	65Watt	399$
Lullaby neoBLUECozy LED PHOTOTHERAPY DEVICE [15]	- 450-465 Nm Narrow Beam Emitting Light Emitting 24 Pcs Blue Led - unilateral lighting - Up to 50,000 hours of LED life	20Watt	720$
Presented LED PHOTOTHERAPY DEVICE	- 460 Nm Narrow Beam Emitting Light Emitting 60 Pcs Blue Led - double sided lighting - Focus light - Up to 50,000 hours of LED life - contactless baby skin temperature monitoring - weight sensor - Web cam baby monitoring	65Watt	150$

Moreover, the cost of the developed system is very low compared to the sales prices of the similar commercial products in the market. Additional features added to the phototherapy device, such as IP webcams and contactless baby temperature measurement, double the production cost of the system. But even with this cost increase, it is seen that the proposed system is produced at a much lower price than the similar commercial products in the market.

Conclusion

A multifunctional phototherapy device was developed to treat newborn jaundice. Properties of the developed phototherapy device are; Automatic detection of newborn's presence, double-sided illumination, continuous monitoring with IP webcam, temperature measurement of the environment and also newborn's body temperature. The light intensity of the device was measured with a photometer as 28.6 μW/cm²/nm.

Peer-review: Externally peer-reviewed.

Conflict of Interest: The author have no conflicts of interest to declare.

Financial Disclosure: The author declared that the study has received no financial support.

References

1. J.T. Benjamin "Neonatal Jaundice", Medical College of Georgia, 2008.
2. S. Öztürkcan, "Yenidoğan Derisinin Fizyolojik Özellikleri", Dermatolojide Yeni yaklaşımlar, Dermatose, vol. 2, no. 4, pp. 202-208, 2003.
3. Subcommittee on Hyperbilirubinemia, ''Management of hyperbilirubinemia in the newborn infant 35 or more weeks of gestation", Pediatrics, vol. 114, no. 1, pp. 297-316, 2004. [CrossRef]
4. A. M. Hafkamp, ''Oral treatment of unconjugated hyperbilirubinemia", University Library Groningen, 2006.
5. H. J. Vreman, R. J. Wong, D. K. Stevenson, ''Phototherapy: current methods and future direction", In Seminars in perinatology, vol. 28, No. 5, pp. 326-333, WB Saunders, Oct, 2004.
6. N. Canbulat, M. Demirgöz, ''Newborn's light treatment: Phototherapyh", Zeynep Kamil Tıp Bülteni, vol. 40, no. 1, pp. 37-41, 2009.
7. T. Dağoğlu, F. Ovalı, ''İndirekt hiperbilirubinemi", T. Dağoğlu, Neonataloji, İstanbul, Nobel Tıp Kitabevleri Ltd, 2000 vol, 50, pp. 453-455, 2000.
8. U. Demirsoy, ''İndirekt Hiperbilirubinemi Nedeniyle Fototerapi Alan Term Yenidoğanlarda İntravenöz Sıvı Desteğinin Bilirubin Seviyesi Üzerine Etkisi", Zeynep Kamil Women and Children Diseases Training and Research Hospital, İst, 2005.
9. G. Hart, R. Cameron, ''The importance of irradiance and area in neonatal phototherapy", Archives of Disease in Childhood-Fetal and Neonatal Edition, vol. 90, no. 5, pp. F437-F440, 2005. [CrossRef]
10. P. Eggert, C. Stick, ''The pattern of bilirubin response to phototherapy for neonatal hyperbilirubinemia", Pediatric research, vol. 18, no. 7, pp. 682, 1984. [CrossRef]
11. A. Mickelson, ''Physical optics", Springer Science & Business Media, 2012.
12. E. Özcan. (11.12.2018). Available: http://www.ertuncozcan.com/images/dosyalar/Yeni_Dogan.pdf.
13. Devlet Malzeme Odası. (11.12.2018). Available:https://www.dmo.gov.tr/Katalog/Urun/Detay/1310_5645.
14. NeoBLUE cozy sistemi. (11.12.2018). Available:http://www.sgeyazilim.com/yonetimpaneli/upload/neoblue.pdf.
15. Colmed. (11.12.2018). Available: http://www.colmed.in/ge-lullaby-led-phototherapy-system.html.
16. Led Journal. Available: https://www.ledjournal.com/main/wp-content/uploads/2012/05/Philips_Understanding-Power-LED-Lifetime-Analysis.pdf.

Mehmet Feyzi Akşahin received the B.S degree in electrical and electronics engineering from Başkent University, and the Ph.D. degree in in electrical and electronics engineering from Middle East Technical University and Başkent University, Ankara, Turkey, in 2002, 2010 respectively. At 2003, he joined to Başkent University, biomedical engineering department as a research assistant. He made his postdoctoral study at the Roswell Park Cancer Institute, Buffalo, NY, USA in 2013. He has been working as an assistant professor at Başkent University, biomedical engineering since 2015. His research areas are signal processing, medical device design, intelligent systems and image processing.

İSTANBUL UNIVERSITY
CERRAHPAŞA

RESEARCH ARTICLE
Electrica 2019; 19(1): 72-84

Detection of Structural Vibration-Induced Noises with Modal Analysis in Diesel Generators

Uğur Ölmez[1], Nevra Bayhan[2], Hakan Doğan[1], Murat Uysal[1]

[1]Teksan Generator, İstanbul, Turkey
[2]Department of Electrical and Electronics Engineering, İstanbul University-Cerrahpaşa, İstanbul, Turkey

Cite this article as: Ölmez U, Bayhan N, Doğan H, Uysal M. Detection of Structural Vibration-Induced Noises with Modal Analysis in Diesel Generators. *Electrica*, 2019; 19(1): 72-84.

ABSTRACT

Diesel generators are one of the most common used energy sources for maintaining the continuity of electrical energy. Diesel generators cause high noises during their operation. There are many methods of eliminating the noise problems that diesel generators generate during energy production. However, these methods show differences according to the type of noise source. In this study, the problem of noise was emphasized that it is caused by structural vibrations of diesel generators. Therefore, the method of coherence function, which is an analytical method, was used for the detection of noise caused by structural vibrations. A test software and user interface was developed to perform sound and vibration measurement and analysis with using coherence function. The coherence analysis of sound and vibration data was made by performing various tests and measurements with the developed test software. In the coherence tests of diesel generator, the vibration frequencies that cause high noise at the measurement points were determined. In order to verify the coherence tests, the computer-aided 3D solid model of diesel generator used in the tests was created. Computer-aided modal analysis of the diesel generator was performed by using this model. The modal analysis was performed at the vibration measurement points and the frequencies that cause high noise. Coherence test results and modal analysis results were compared. It was seen that the results of the coherence measurement and the results of the computer-aided modal analysis supported each other. As a result of these studies, it was shown by computer-aided modal analysis that the high noise occurring in diesel generators can be determined by the coherence tests.
Keywords: Diesel generator, coherence, sound, vibration, modal analysis

Corresponding Author:
Nevra Bayhan

E-mail:
nevra@istanbul.edu.tr

Received: 12.12.2018

Accepted: 26.12.2018

DOI: 10.26650/electrica.2019.18048

Introduction

Today, electrical energy has entered into every aspect of our lives in parallel with the rapid development of technology. The use of electrical energy in many areas such as hospitals, data centers, telecommunication base stations, industrial facilities has reached critical levels. In these areas, an instantaneous energy interruptions can result in massive catastrophes that end in loss of life and property.

Diesel generators are widely used to maintain the continuity of the electric energy. Diesel generators which detect electricity interruptions quickly and connect to the mains in a very short time are one of the most preferred energy production sources in back-up of grid.

The problem of noise caused by the widespread use of diesel generators is becoming a more important problem especially in the living areas such as housing, hospitals and business centers. For this reason, methods of reducing noise levels of the generators to the lower values have been investigated. The first thing to do in these studies is to determine the noise sources.

Diesel generators have many noise sources that cause high noise. The main sources that give rise to noise in diesel generators are classified as engine block noise, radiator fan noise, alternator mechanical noise, alternator induction noise, exhaust noise and structural vibration-induced noises.

The equipments of the diesel generator consisting of rotating parts such as engine, alternator and radiator cause the structural vibrations to occur on the chassis where the generator is

fixed and surface of the sound attenuated enclosure connected to it. These structural vibrations cause the noise propagation from the chassis and sound attenuated enclosure surfaces. The main purpose of this study is to determine the vibration points and frequencies that cause noise on the generator chassis and sound attenuated enclosure.

At the beginning of this study, in order to determine the noises caused by the structural vibrations on the generator chassis and sound attenuated enclosure surfaces, the frequency analysis was applied to the noise and vibration data separately. Fourier Transform was used for frequency analysis of noise and vibration data. Fourier transform is an analytical method which is used to characterize linear systems and defines frequency components that create a continuous wave form [1].

Cooley and Tukey [2] developed an algorithm in 1965 that had the ability to calculate Fourier coefficients much faster than was needed in the past. This method is known as Fast Fourier Transform (FFT) nowadays. Frequency band analysis of noise and vibration data was performed by using FFT method.

As a result of studies which are done separately in the frequency band, there cannot be found direct relationship between noise and vibration data. For this reason, the coherence function was used to determine the relationship between sound and vibration data. The coherence function is defined as the counterpart of the normalized cross-correlation of time signals in the frequency domain.

The need for additional understanding of the noise generation process was enabled many studies on diesel engines at Herrick Laboratories. With the help of the obtained data from the noise studies that multiple input – single output (MISO) coherence models of diesel engines were created [3, 4].

In some studies on diesel engines, the coherence function has been used to determine the noise caused by cylinder pressures. Leclere et al. [5] performed a study to determine the relationship between cylinder pressure and noise. In this study, the relationship between vibration of cylinder pressure and the noise was investigated by coherence function. Narayan [6] has determined the relationship between the vibration of the cylinder pressures and the noise of diesel engines with the help of the coherence function. As a result of this study, Narayan [6] stated that engine noise control could be performed by controlling the injection parameters. Lamula et al. [7] examined the effect of different fuels such as diesel and gas on cylinder pressure. The effect of the vibrations which caused by the different cylinder pressures on the noise generation were obtained by the tests using the coherence function by Lamula et al. [7].

It is also possible to formulate in the time domain a MISO model which was used in some acoustic measurement applications by Goff [8] and also known as the correlation technique. Although, this method successfully has been applied in different work areas such as turbulence studies, it could not become widespread in noise control studies. However, Kumar and Srivastava [9] used this technique to get successful results for noise source identification of diesel engines.

Vibration-induced noise analysis with the coherence function has also been realized in different areas besides diesel engine applications. Pazara et al. [10] used the coherence analysis between noise and vibration to detect defects due to the production of bearings and other moving parts. Lukic [11] in his study, in order to analyse the noise and vibration problems which caused by hydraulic systems in the vehicles examined the sound pressure level and vibration levels of hydraulic pumps by using the coherence function.

In this study, the computer-aided 3D solid model of diesel generator used in the tests was created to verify the coherence tests. Computer-aided modal analysis of the diesel generator was performed by using this model. Modal analysis is the study of the dynamic properties of linear structures based on structural tests or simulaton-based finite element analysis. These dynamic properties include natural frequencies and structural modes. The dynamic properties depend on the mass, stiffness and damping distribution on the structure and determine the structural vibration behaviour when exposed to operational loads.

When linear structures exposed to a vibration at natural frequency values, they are resonated. This situation may cause to increase the amplitude of the vibration which the structure is exposed and cause permanent damages to the structure. Therefore, it is important to determine the natural frequency values of the structures. The natural frequency values of the structures can be determined by modal analysis method and necessary precautions can be taken.

Several studies have been carried out to determine the natural frequency values of various equipment of diesel generator. The majority of these studies have been performed for diesel engines which are the main power source of the generators. These studies have generally been concentrated on the crankshaft and cylinder block of diesel engines. In addition, it was also observed that modal analysis studies were performed for various equipments such as chassis and control panel of diesel generators.

Carrato and Fu [12] performed a study to determine the torsional vibrations on the crankshaft of diesel engines. Carrato and Fu used a method which based on modal analysis techniques in their study. Meng et al. [13] performed the stress and modal analysis of the crankshaft of a 4-cylinder diesel engine with the finite element method. Meng et al. [13] analysed the vibration modes, impact and stress conditions of the crankshaft in their study. With the results of analysis, they obtained information about optimization and improvement of diesel engine design.

Espador et al. [14] conducted a study to determine the cause of the breakage after the cylinder and liner break in a diesel

engine of a 7.5 MW (MegaWatt) generator which is operating in a power plant. It was seen that the critical areas which are determined by the finite element analysis of the liner match the fracture zones of the liner. Jiang and Yan [15] investigated the results of modal analysis with different mesh densities of a diesel engine block. The results which are obtained from the study constitute a reference for element selection in future modal analysis studies. The results also provide the basis for structural dynamic analysis and noise control studies in future studies.

Aher and Malave [16] conducted a study to understand how the excitation forces from engine and alternator mounting feet propagates to the rest of the generator structure. In addition to the study, modal analysis was also performed to determine the potential modes and natural frequencies of the diesel generator set. In the results of modal analysis, it was observed that several modes were close to motor harmonics and these modes could increase the vibration response of the generator set. Magdum and Yadav [17] examined the mechanical properties of the material which is used in the diesel engine test bed on the natural frequency, mode shape and frequency response of the test bed. In the study, the effect of two materials of different densities on the natural frequency and mode shape was investigated. Magdum and Yadav [17] concluded that the mechanical properties of the used material had a direct effect on the natural frequency and mode shape. Kadam and Zope [18] in their study discussed the design that will optimize the vibrations that the control panel of a diesel generator set can be resonated.

This study was performed to contribute to the literature studies to determine the relationship between the noise and vibration of diesel generators. Therefore, it was aimed to determine the noise which generated by the vibrations on the chassis and sound attenuated enclosure of diesel generators based on the coherence studies on diesel engines. Also in this study, a computer aided modal analysis study was performed to determine the natural frequency values of the diesel generator chassis and sound attenuated enclosure. The aim of this study to compare the vibration values which are obtained by the coherence analysis with the natural frequency values which are obtained from the computer aided modal analysis results.

Material and Method

In order to perform the coherence analysis of diesel generators, a test software was developed which can perform sound and vibration measurement and give the coherence values of the measurement for this experimental study. A user interface was also designed for this software. A test setup was established in order to perform coherence analysis and various tests were carried out with the developed software. In the tests, coherence analysis were performed by being taken sound and vibration measurements from different points of the generator [19].

In this study, unlike [19], modal analysis method was applied for the chassis and sound attenuated enclosure of the diesel generator. Natural frequency values of the chassis and sound attenuated enclosure parts of the generator were found by modal analysis method. The natural frequency values calculated by the modal analysis were compared with the structural vibration-induced noise points which are obtained in the tests.

Coherence function analysis

The mathematical method that uses determining the relationship between two or more signals is called coherence analysis. The normalized cross correlation of two analog signals in the time domain is defined as coherence in the frequency domain.

Single Input – Single Output (SISO) coherence model was used in this study. Figure 1 shows a block diagram which belongs to SISO coherence model.

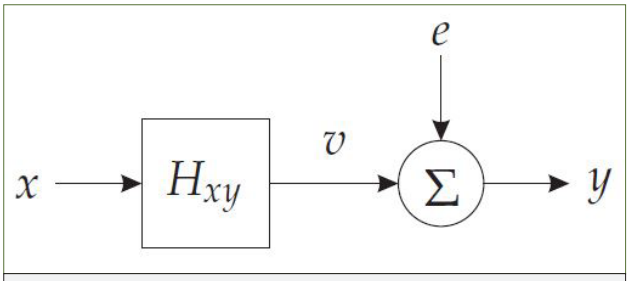

Figure 1. A block diagram of single input - single output coherence model [20]

Since the coherence technique is defined as the frequency domain equivalent of the normalized cross correlation of the analog signals, the self spectral power densities and cross-spectral power densities of the analog signals are used in the coherence calculations. The cross-spectral power density calculation is given as

$$S_{xy} = \frac{1}{KU}\sum_{k=1}^{K} X_k^* Y_k \quad (1)$$

where S_{xy} expresses the cross-spectral power density between the *x* and *y* signals, *K* expresses element number and X_k^* expresses complex conjugate of the signal *x*. The quantity constant *U* is defined as

$$U = f_s \sum_{n=1}^{M} W(n)^2 \quad (2)$$

where *W(n)* is a constant that takes into account the spectral weight of the data window. *W(n)* is used to properly scale the spectral power density, assuming that the input is measured as volts. *M* is the element length corresponding to the windowing length. f_s is the sampling rate.

The self spectral power density value S_{xx} of x signal is calculating by typing x instead of y in the equation specified in (2). The method of calculating the self spectral power density S_{xx} is given as

$$S_{xx} = \frac{1}{KU}\sum_{k=1}^{K}\left|X_k\right|^2 \tag{3}$$

The transfer function of the input and output signals which is given by Figure 1 can be expressed by

$$Y(f) = H(f)X(f) \tag{4}$$

where $H(f)$ is the expression of the system transfer function. The system transfer function $H(f)$ as spectral power density is given as

$$H(f) = \frac{S_{xy}(f)}{S_{xx}(f)} \tag{5}$$

The coherence function is expressed by using cross and self spectral power densities and given as

$$C_{xy} = \frac{\left|S_{xy}\right|^2}{S_{xx}S_{yy}} \tag{6}$$

where C_{xy} expresses to the coherence function between the two signals, S_{yy} expresses to the self sprectral power density of signal y. Equation (6) is a mathematical expression in which the linear relationship between x and y signals is scaled between 0 and 1. If the result of this function is 0 or close to 0, the x and y signals are unrelated; however, if the result of this function is 1 or close to 1, the x and y signals are linearly related [20].

Modal analysis method

The behavior of the mechanical equipments under dynamic loads is determined using dynamic parameters to have characteristic feature for each mechanical component. These dynamic parameters are obtained by analytical models or experimental studies. Analytical modeling is called as modal analysis in the literature. Natural frequency values and mode shapes of the mechanical structure are obtained by modal analysis. The natural frequency is the frequency that it depends only on elasticity and mass of an object and when it is stimulated, it vibrates at high amplitude continuously. The mode shape refers to the shape and direction of displacement occurring when a structure vibrates at its natural frequency. In short, the mode shape is an expression that gives the direction and amplitude of the vibration. In this study, natural frequencies and mode shapes of the diesel generator chassis and sound attenuated enclosure were determined by modal analysis.

For the analysis of mechanical systems, at first, a mathematical model which can express the system adequately is created. The mathematical model of mechanical systems is classified according to the degree of freedom and the state of damping. The degree of freedom is the number of coordinates which are required to define the position of each part of the mechanical system at any time. In this study, modal analysis calculations were explained on the mathematical model of a mechanical structure with single degree of freedom, undamped, free vibration. The mathematical model of an object with an undamped and single degree of freedom system was shown in Figure 2 [21].

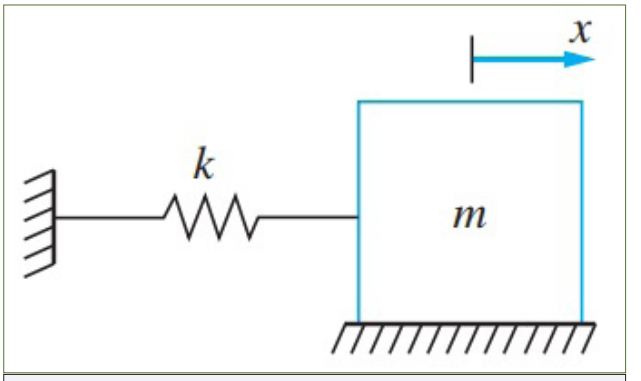

Figure 2. A mathematical model of mechanical system with undamped, free vibration and single degree of freedom [21]

The equation of motion of an undamped, single degree of freedom mechanical system is given as

$$M\ddot{X}(t) + KX(t) = 0 \tag{7}$$

where M is the mass of the mechanical structure and K is the elasticity coefficient of the mechanical structure. The $X(t)$ refers to the quantity of displacement of vibration motion. The $X(t)$ which is used in (7) is generally expressed as

$$X(t) = \phi\sin(wt + \varphi) \tag{8}$$

where φ is the amplitude vector, w is the frequency value, Ø is the phase angle. If derivative of (8) is taken twice, the expression is obtained as

$$\ddot{X}(t) = -w^2\phi\sin(wt + \varphi) \tag{9}$$

Substituting (9) and (8) into (7) and rearranging it results in

$$(K - w^2M)\phi = 0 \tag{10}$$

Equation (10) is in the format of numerical eigenvalue problem. The solution of this problem is found by equalizing the determinant of the coefficient matrix to zero. The mathematical expression of the coefficient matrix is shown as

$$\left|K - w^2M\right| = 0 \tag{11}$$

The solution of (11) causes the formation of n different roots with degree of w^2. The roots obtained in the form of w_1^2, w_2^2

, …, w_n^2 are expressed as the eigenvalues of the equation of motion. These obtained eigenvalues are also natural frequencies of the mechanical structure. There is a n dimensional ϕ_i eigenvector corresponding to each w_i^2 eigenvalue. ϕ_i eigenvectors are obtained by solving the expression given by

$$(K - w_i^2 M)\phi_i = 0 \tag{12}$$

These obtained eigenvectors are also called mode shape or natural mode of the mechanical structure. The mode shape is a vector which expresses the direction of vibration of the structure. A mathematical expression of eigenvectors is given as [22].

$$\phi_i = \left\{\phi_{1i}, \phi_{2i}, \ldots, \phi_{ni}\right\}^T \tag{13}$$

Software development for coherence analysis

The coherence function was used to determine the relationship between the noise and vibration of the diesel generators. For this reason, a test software was developed which can perform sound and vibration measurements and also perform coherence analysis of these measurements.

In the first phase of the software development, signal measurement and processing stages were carried out. The measured sound and vibration signals with the aid of a microphone and accelerometer are transmitted to the data acquisition device. The analog signals which are measured by the data acquisition device are transformed into a digital signal by sampling. In this study, sampling was performed in "continuous" mode and 18 kS/s sampling rate.

Following the coding studies related to signal reading stage, the signal processing phase was started such as FFT and coherence calculations. The codes for the calculation of the coherence function of the sound and vibration signals were written according to the equation which is given in (6) and the results were shown graphically in the frequency axis. In addition, the codes which are related to the FFT transformations of the sound and vibration signals were written separately and the results were shown graphically in the frequency axis. The codes which are related to the calculation of RMS (Root Mean Square) levels of sound and vibration signals were also written in the signal processing phase [23].

Fast Fourier Transform analysis of sound and vibration measurements was performed at 1500 Hz bandwidth. Because of the fact that the sound and vibration data of the diesel generators are concentrated at the low frequencies in the frequency axis, it was thought that 1500 Hz bandwidth will be sufficient.

Different analysis methods were added to the test software to be able to make more detailed sound and vibration analysis. With the help of these analysis methods, it is possible to perform octave band analyses of the sound measurement and the velocity and displacement analysis of the vibration measurement [23].

The software also includes sound recording capability in accordance with ISO 3744 standard in order to perform generator sound measurements [24]. A reporting interface that transfers measurement data to Excel was also added the software so that the measurement results can be backed up and reported.

Figure 3 shows a screenshot of the user interface of the developed software. In the right section of the software, there are

Figure 3. A screenshot of the user interface of the developed test software

frequency band analysis of the coherence, sound and vibration measurements. In the left section, there are tabs for the settings and measurement results, including sound recording and reporting features.

Experimental Results

Test setup

In this study, a test setup was prepared in order to determine the noise problems of the diesel generators due to the structural vibrations. In the test setup, a 4-cylinder diesel generator which is at 21 kVA standby power and operates at a constant speed of 1500 rpm was used. An acoustic microphone was used for generator noise measurements. An accelerometer was used for the vibration measurements. The sound and vibration signals were sampled using the data acquisition device and transferred to the test software. The obtained signals were analysed using the test software. An image of the test setup is shown in Figure 4.

Figure 4. Test setup for coherence analysis

In this study, noise measurements were performed according to the indicated methods and reference measurement points in the ISO 8528-10 standard [25]. However, the noise measurements as well as the vibration measurements were also carried out in this study. For this reason, noise measurements were taken only for surfaces where vibration was measured. Because of the fact that the effect of the vibration on the noise was felt less felt at the corner points, noise measurements were not carried out at the corner points. Figure 5 shows the reference points for generator noise measurement. The noise measurements for this study were performed at reference points 1, 2, 3, 4 and 9.

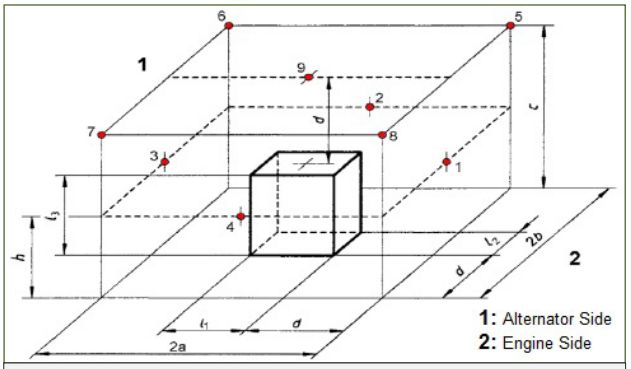

Figure 5. Reference measurement points used for noise measurements [25]

Noise measurements were made at a distance of 1 meter from the generator surface and the ground.

According to the ISO 8528-10 standard, the noise measurements of diesel generators are performed with power of %75 kW of the generator prime power. For this reason, noise measurements were performed at a load power of 11.4 kW which is %75 power of the diesel generator.

The vibrations of the generator chassis and sound attenuated enclosure surfaces are not known since any vibration measurements have not been taken before. Therefore, vibration measurements were taken from the center and end points of all parts on sound attenuated enclosure and chassis. Vibration measurements were taken from 59 different points including the front, rear, right, left and top surfaces of the generator sound attenuated enclosure and the top and side surfaces of the chassis. Figure 6 shows that an image of the reference points of vibration measurements taken from the sound attenuated enclosure and chassis.

Test results

Noise and vibration measurements were taken many points on the generator surfaces with using test setup and software. Noise and vibration measurements were made separately from each determined point on generator surfaces. Coherence analysis of the measured signals was carried out with the help of the developed test software. Frequency domain analysis of sound and vibration signals was performed separately using the test software and the frequency characteristic of the system was examined.

It was seen that only the coherence analysis was not sufficient to achieve a clear result. Therefore, frequency analysis of the sound and vibration values of the generator were included in the evaluation criteria. For this purpose, the velocity value of the vibration measurement according to the criteria specified in ISO 10816-1 standard was obtained and used to evaluate the results [26]. Here, the reference value for velocity magnitude was selected as 1.8 mm/s, which is the lower limit for small machines of Class-1 type specified in the ISO 10816-1 standard. In

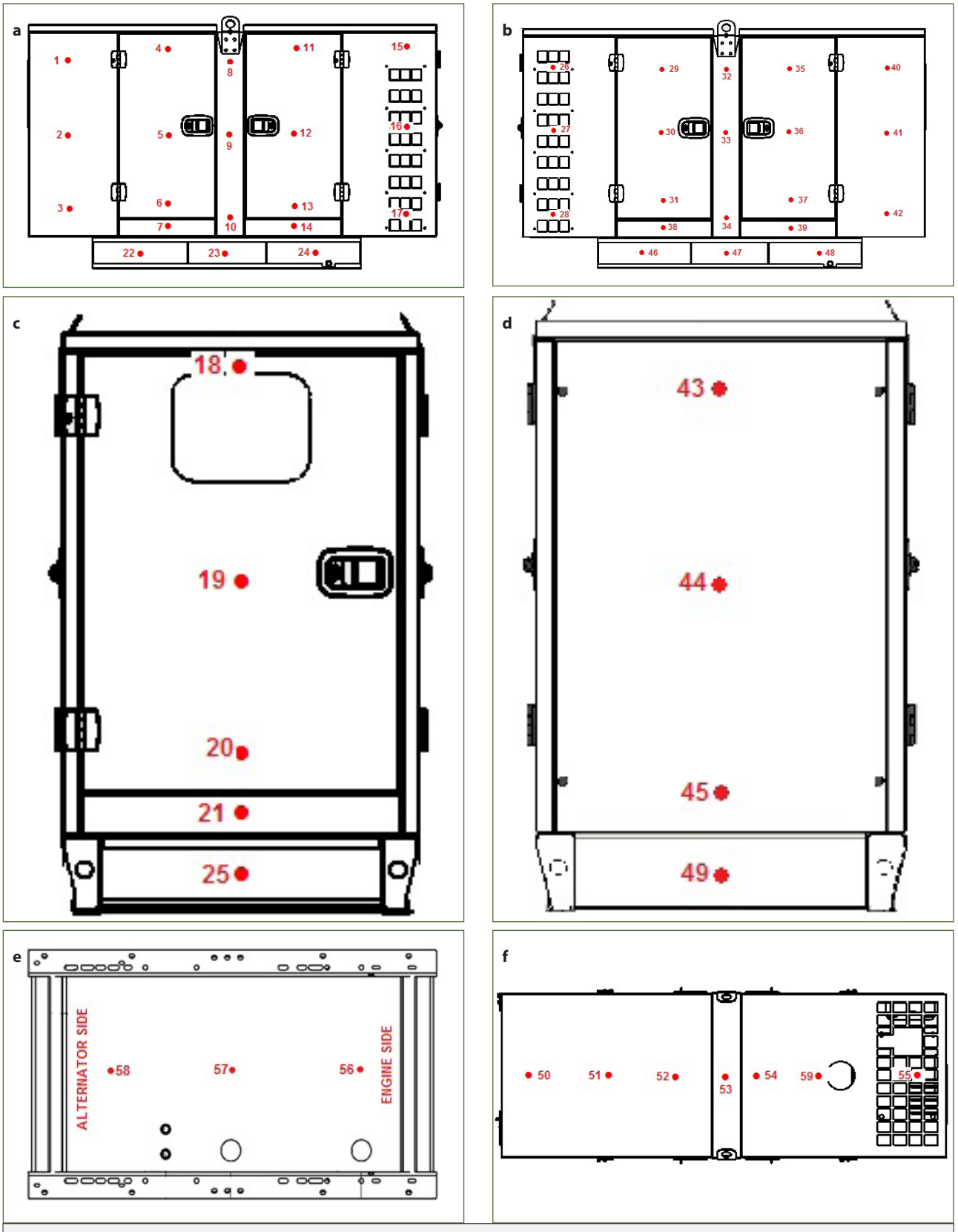

Figure 6. a-f. Reference measurement points for vibration measurements. From left side of generator (a). From right side of generator (b). From front side of generator (c). From back side of generator (d). From top side of chassis (e). From top side of generator (f)

this standart, machines up to 15 kW are considered as Class-1 machines.

The evaluation criterion for sound level measurement in this study is the octave band values of the measured sound levels on a frequency domain. The octave band values of the sound measurement were taken into account in the cases below 10 dBA of the Leq (Equivalent Continuous Sound Level) sound level of the same measuring points. The reason for selecting 10 dBA here is that the noise level difference between sources up to 10 dBA affects the ambient sound level.

The most important criterion in the evaluation of the test results is the coherence analysis. For the frequencies which are below 4000 Hz, the coherence limit is selected to 0.8 [27]. In this study, the coherence limit was chosen as 0.7 in order to be able to keep the evaluation scale slightly wider. However, it is already mentioned that only the coherence value is not sufficient to reach a clear result. Therefore, the octave band level and vibration velocity level was examined simultaneously for frequency values with high coherence value. The frequency values which have high octave sound level and high vibration velocity level were considered as frequency values that have noise problem related to vibration.

Figure 7 shows the measurement results for the vibration measurement point-15 graphically. The reason for selecting measurement point-15 is that it contains vibrations at the frequency of 150 Hz, which is the 3rd harmonic of the generator. All other measurement points were also measured in the same format. The graph shows the frequency curves of the coherence, sound pressure and vibration acceleration values. According to the graph given in Figure 7, it is observed that the frequency values such as 50 Hz, 100 Hz, 150 Hz, 200 Hz and 500 Hz have high coherence values. At the evaluation stage, the measured sound levels were converted from dB to dBA. Since the dBA sound levels at 50 Hz, 200 Hz and 500 Hz were considerably lower than Leq sound level, noises at these frequencies were not taken into account.

As a result of the detailed examination of the test results, it was determined that vibration induced noise problems occurred on 13 different vibration measurement points on the sound attenuated enclosure and the chassis of the generator. According to test results, it was seen that the noise related to the vibration occured at 63 Hz, 100 Hz, 125 Hz and 160 Hz octave frequencies. The test results were shared in Table 1. The values given in the Table 1 are the results of noise and vibration analysis of the diesel generator selected for this study. According to these values, it is concluded that vibration induced noise is generated at the given vibration measurement points.

Modal analysis results

The field of the study in which the effect of mechanical equipment under dynamic loads is determined with the help of dynamic parameters called as modal analysis in the literature. Natural frequency values that can cause deformation in mechanical structure are determined by modal analysis. In order to perform modal analysis of diesel generator which is used in

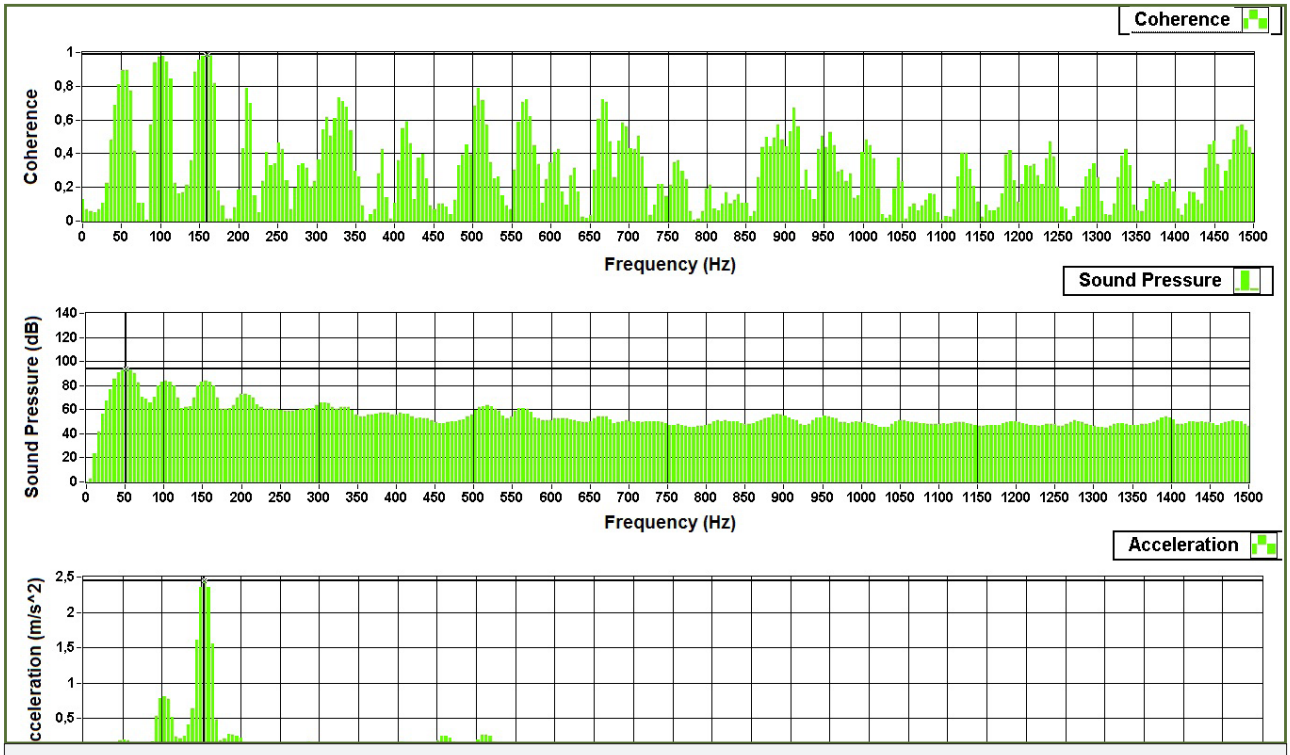

Figure 7. Graphical analysis of coherence, sound pressure and vibration acceleration values for measurement point-15

Table 1. Vibration points that cause high noise level

No	Frequency (Hz.)	Coherence Value	Velocity Value (mm/s)	Oktave Sound Level (dBA)	Leq. Sound Level (dBA)
2	97.3	0.83	2.32	69.11	72.49
	102.4	0.88	2.13		
3	92.2	0.91	3.35	66.44	72.25
	97.3	0.9	6,33		
	102.4	0.86	8.03		
	107.5	0.8	8.64		
	122.9	0.71	2.55	63.58	
4	61.4	0.9	1.82	62.02	72.96
15	102.4	0.95	1.82	70.32	72.78
	148.5	0.8	3.41	74.13	
	153.6	0.89	3.37		
	158.7	0.92	3.07		
	163.8	0.87	2.05		
17	158.7	0.78	1.9	74.73	72.65
18	92.2	0.95	2.16	65.93	73.45
	97.3	0.95	3.24		
	102.4	0.9	3.5		
	107.5	0.79	3.26		
42	153.6	0.81	1.85	74.46	72.69
50	97.3	0.9	2.09	66.96	73.43
	102.4	0.92	2.45		
	107.5	0.9	2.53		
51	92.2	0.87	1.97	67.77	73.33
	97.3	0.9	2.67		
	102.4	0.89	2.65		
	107.5	0.87	2.53		
	112.6	0.77	1.86	66.79	
55	56.3	0.93	3.76	62.59	72.84
	61.4	0.93	5.08		
	66.6	0.89	4.66		
57	61.4	0.82	2.27	63.31	73.8
	66.6	0.79	2.25		
	92.2	0.76	2.95	68.32	
	97.3	0.8	4.69		
	102.4	0.8	5.13		
	107.5	0.78	4.83		
58	92.2	0.81	3.17		73.71
	97.3	0.82	4.69		
	102.4	0.82	4.98		
	107.5	0.82	4.57	70.65	
	112.6	0.76	2.92	67.04	
59	61.4	0.71	2.36	63.18	73.69
	92.2	0.82	1.89	69.92	
	97.3	0.89	2.49		
	102,4	0.91	2.71		
	107.5	0.9	2.62		
	112.6	0.82	1.8	65.89	
	148.5	0.72	1.91	70.34	

Hz: hertz; mm/s: millimetre/second; dBA: a-weighted decibels; Leq: equivalent continuous sound level

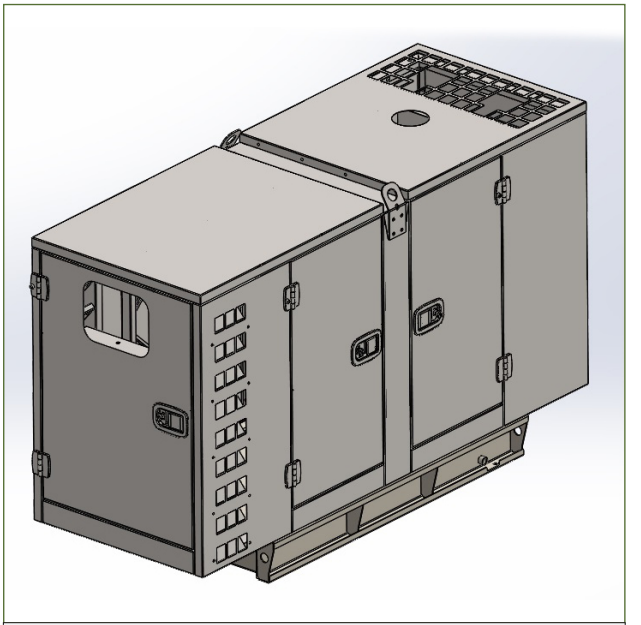

Figure 8. The 3D solid model of the diesel generator

the tests, a computer-aided 3D solid model of the generator was prepared. The 3D solid model of the diesel generator was designed using the SOLIDWORKS software. S235JR type steel was used in the design of the solid model. The thickness of the material which is used in solid model is 1.5 mm on the sound attenuated enclosure surfaces and 3 mm on the chassis surfaces. The designed solid model is physically similar to the diesel generator which is used in the tests. Figure 8 shows an image of the 3D solid model of the diesel generator.

The 3D solid model which is designed to perform modal analysis was transferred to the ANSYS software. ANSYS software is an analysis software that uses the finite element method (FEM). Mesh operation of designed solid model were performed in ANSYS software. The mesh opration is expressed as the process of splitting a physical definition range into smaller definition ranges. The aim of meshing is to facilitate the solution of the differential equation to be solved. Therefore, the accuracy of the results to be obtained in the finite element method depends on the type of element and the number of elements which are used in the mesh.

The number of elements that are used in the mesh operation of the diesel generator is 421010. The mesh element type which is used in the meshing is tetrahedron and the number of nodes is 923591. Figure 9 shows an image of the mesh type of the diesel generator.

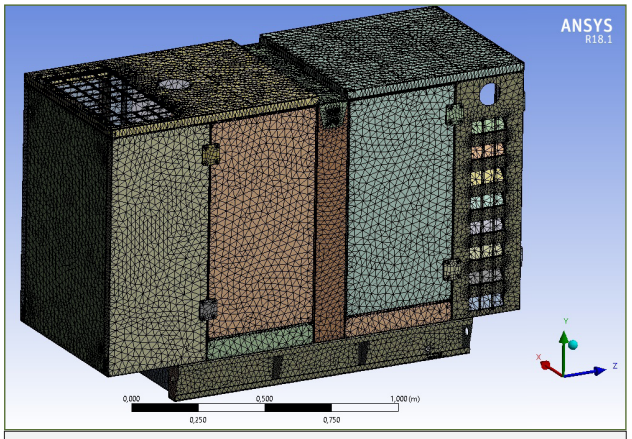

Figure 9. The mesh form of the diesel generator

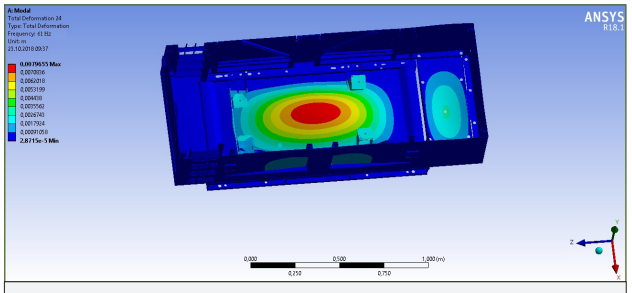

Figure 10. Modal analysis result, for the chassis upper surface at the frequency of 61 Hz

The designed 3D solid model was subjected to modal analysis in a frequency range of 0-200 Hz according to a free and unforced motion equation. The system was examined in such a way that it was not exposed to external force and the natural frequency values and mode shapes of the structure were obtained.

In this paper, the vibration points which were found by experimental studies and caused high noise were examined by modal analysis for each vibration point and frequency value. As a result of the analysis, it was observed that the natural frequencies determined by the modal analysis have the same values as the vibration points determined by the experimental studies and they were performed at the same measuring points.

Figure 10, 11 and 12 show the images which belongs to the modal analysis results. The modal analysis result of the chassis upper surface is shown in Figure 10. According to the results of the model analysis, it was seen that the vibration measurement point-57 on the chassis has a natural frequency at 61 Hz. The mode shape is as shown in Figure 10. The vibration levels were scaled with colors in the blue-red range. The structures that vibrate at the same frequency with the natural frequency value reach the higher vibration levels with the resonance effect. With the performed tests, it was observed that the vibration values which are obtained from the measurement

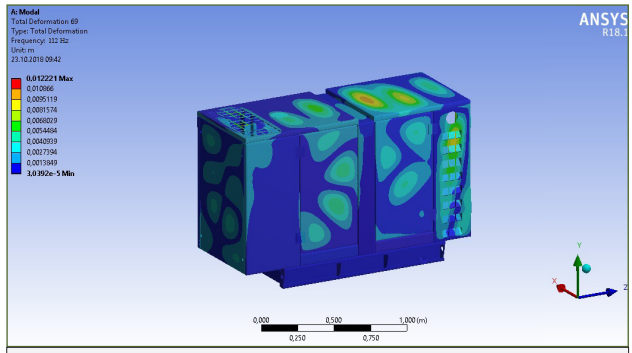

Figure 11. Modal analysis result, for the left and upper surface of sound attenuated enclosure at the frequency of 112 Hz

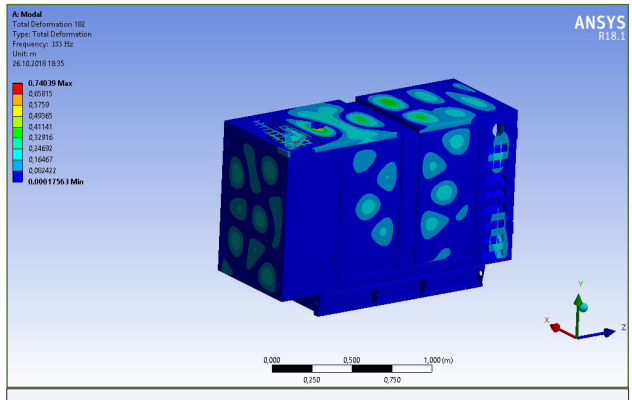

Figure 12. Modal analysis result, for the left and upper surface of sound attenuated enclosure at the frequency of 153 Hz

point-57 were high. This high vibration level causes an increasing on the noise level of the measurement point-57. The noise and vibration values of the measurement point-57 are shown in Table 1.

The modal analysis result of the left and upper surfaces of the sound attenuated enclosure are shown in Figure 11. According to the results of the model analysis, it was seen that the vibration measurement point-51 on the upper surface of the sound attenuated enclosure has a natural frequency at 112 Hz. The mode shape is as shown in Figure 11. With the performed tests, it was observed that the vibration values which are obtained from the measurement point-51 were high. This high vibration level causes an increasing on the noise level of the measurement point-51. The noise and vibration values of the measurement point-51 are shown in Table 1.

Similarly, the modal analysis result of the left and upper surfaces of the sound attenuated enclosure at 153 Hz are shown in Figure 12. According to the results of the model analysis, it was seen that the vibration measurement point-15 on the left surface of the sound attenuated enclosure has a natural frequency at 153 Hz. With the performed tests, it was observed that the vibration values which are obtained from the measurement point-15 were high. This high vibration level causes an increasing on the noise level of the measurement point-15. The noise and vibration values of the measurement point-15 are shown in Table 1.

According to the results of the modal analysis, it was seen that in all of the vibration points which are determined in Table 1, the mode shapes were formed related to the natural frequency at the determined frequencies. The obtained mode frequency in the analysis and the regions in which the mode shape occurring are consistent with the test results. According to this result, it is concluded that the computer aided modal analysis supports the results of the coherence tests for diesel generators.

As a result, modal analysis of the sound attenuated enclosure and the chassis surfaces of the diesel generator were made and compared with the results obtained from the tests. In the light of the data obtained, it was also supported by the modal analysis method that the diesel generator have noise problems caused by structural vibrations.

Conclusion

In this study, it was aimed to determine the noise problems related to the structural vibration of diesel generators. Therefore, a test software that can perform coherence analysis was developed. Furthermore, sound and vibration measurements were taken for the coherence analysis. In addition, a computer aided model of the generator was created and modal analysis were performed.

In the literature researches, the noises caused by the vibrations which formed with the combustion of the fuel in the diesel engines were investigated by using coherence function. The examined studies are the papers on how the raw noise of diesel engines is affected by the noise generated by the vibrations on the engine surface. In this paper, it was investigated how the noise level measured from outside the sound attenuated enclosure of diesel engines was affected by the noise generated from the sound attenuated enclosure and the chassis vibrations. At the same time, the generator chassis and sound attenuated enclosure were subjected to modal analysis and it was aimed to find the vibration points and frequencies that may cause noise. Modal analysis and test results were compared and it was investigated whether the vibration points that cause noise support each other.

When the tests and analysis results were examined, it was observed that the diesel generator had noise problem at 2, 3, 4, 15, 17, 18, 42, 50, 51, 55, 57, 58 and 59 numbered vibration measurement points. The noise problem at these vibration measurement points were observed at the octave frequencies of 63, 100, 125 and 160 Hz respectively. As a result of this information;

It was seen that diesel generators have noise problems caused by structural vibrations.

It was concluded that the vibration-induced noise points can be determined by using the modal analysis results.

Whether the test points which are obtained by the modal analysis results generate vibration-induced noise was determined by coherence tests.

At the vibration points numbered 2, 3, 4, 15, 17, 18, 42, 50, 51, 55, 57, 58 and 59 on the generator chassis and sound attenuated enclosure was seen that had noises related structural vibrations. These noises were seen at 63, 100, 125 and 160 Hz octave frequencies.

It was observed that the noise points related with vibration are generally concentrated in the cooling air inlets-outlets, on the doors, on the sound attenuated enclosure upper surfaces and also the chassis upper surfaces.

By using the data obtained as a result of this study, it is planned to reduce the determined noise problems in future studies. In this context, the studies planned to be carried out in the first step in order to reduce the level of structural vibration-induced noises are thought to be the selection of vibration dampers with better damping ability at the determined frequencies and increasing the wall thickness of the material to reduce the vibration levels at the vibration points that cause high noise.

Peer-review: Externally peer-reviewed.

Conflict of Interest: The authors have no conflicts of interest to declare.

Financial Disclosure: The authors declared that this study has received no financial support.

References

1. K. B. Howell, "Fourier Series", in Principles of Fourier Analysis, Boca Raton, USA: Chapman & Hall/CRC, 2001, ch. 2, pp. 93-242. [CrossRef]
2. J. W. Cooley, J. W. Tukey, "An algorithm for the machine calculation of complex fourier series", Mathematics of Computation, vol. 19, no. 90, pp. 297-301, Apr, 1965. [CrossRef]
3. M. J. Crocker, J. F. Hamilton, "Modelling of diesel engine noise using coherence", SAE Transactions, vol. 88, no 2, pp. 1263-1273, 1979.
4. M. J. Crocker, G. Anderkay, J. Y. Chung, "Controlling the noise radiated from diesel engines", Proceeding of First Interagency Symposium on Transportation Noise Research, California, USA, 28-30 March 1973, pp. 631-647.
5. Q. Leclere, J. Doruet, E. Parizet, "Extraction and analysis of diesel engine combustion noise", Proceedings of Exploratory Workshop on Modern Methods of Vibro-Acoustic Study with Application to Automative, Pitesti, Romania, 2011, pp. 37-43.
6. S. Narayan, "A review of diesel engine acoustics", FME Transactions, vol. 42, no. 2, pp. 150-154, 2014. [CrossRef]
7. L. Lamula, K. Saine, K. Saarinen, J. Hyrynen, "Cylinder pressure generated noise of medium speed diesel engine", Joint Baltic-Nordic Acoustics Meetings, Reykjavik, Iceland, 17-19 Aug, 2008.
8. K.W. Goff, "The application of correlation techniques to some acoustic measurements", J Acoust Soc Am, vol. 27, no. 2, pp. 336-346, 1955. [CrossRef]
9. S. Kumar, N.S. Srivastava, "Investigation of noise due to structural vibrations using a cross-correlation technique", J Acoust Soc Am, vol. 57, no. 4, pp. 769-772, 1975. [CrossRef]
10. T. Pazara, M. Pricop, I. C. Scurtu, C. Pricop, O. Radu, "Defect identification of moving parts of a mechanical installation using correlation between vibration and noise", Scientific Bulletin of Naval Academy, vol. 19, no. 2, pp. 504-509, 2016.
11. J. Lukic, "An approach to an NVH investigation of vehicle hydrolic pumps", Journal of Low Frequency Noise Vibration and Active Control, vol. 30, no. 2, pp. 137-147, 2011. [CrossRef]
12. P. J. Carrato, C. C. Fu, "Modal analysis techniques for torsional vibration of diesel crankshafts", SAE Transactions, vol. 95, no. 4, pp. 955-963, 1986. [CrossRef]
13. J. Meng, Y. Liu, and R. Liu, "Finite element analysis of 4-cylinder diesel crankshaft", IJIGSP, vol. 3, no. 5, pp. 22-29, 2011. [CrossRef]
14. F. J. Espadafor, J. B. Villanueva, M. T. Garcia, E. C. Trujillo, "Analysis of a diesel generator cylinder failure", Engineering Failure Analysis, vol. 17, no. 4, pp. 913-925, 2010. [CrossRef]
15. S. Z. Jiang, W. B. Yan, "FEM modal analysis of diesel engine block", Advanced Materials Research, vol. 971-973, pp. 481-484, 2014. [CrossRef]
16. P. B. Aher, S. K. Malave, "Vibration assessment of diesel engine genset mounts", International Conference on Ideas, Impact and Innovation in Mechanical Engineering – ICIIIME 2017, Pune, India, 1-2 Jun, 2017, pp. 1700-1706.
17. S. Magdum, S. D. Yadav, "A finite element analysis of diesel engine test bed using different materials for reducing diesel engine bed vibrations", IJCEA, vol. 12, special issue, pp. 1-8, 2018.
18. A. R. Kadam, S. B. Zope, "Analysis of diesel generator control panel using finite element method", International Conference on Ideas, Impact and Innovation in Mechanical Engineering – ICIIIME 2017, Pure, India, 1-2 Jun, 2017, pp. 577-581.
19. U. Ölmez, H. Doğan, M. Uysal, "Noise analysis of diesel generators with coherence function", Irditech 2018 International R&D, Innovation and Technology Management Congress, İstanbul, Turkey, 18 May, 2018, pp. 307-316.
20. T.C. Richards, "Dynamic testing of data acquisition channels using the multiple coherence function", in Data Acquisition Applications, Z. Karakehayov, Ed, London, United Kingdom: Intech Open, 2012, ch. 3, pp. 51-78.
21. S. G. Kelly, "Free vibrations of SDOF systems", in Mechanical Vibrations Theory and Applications, Si, SI ed., Stamford, USA: Cengage Learning, 2012, ch. 3, pp. 137-204.
22. Z. Q. Qu, "Theory of modal analysis," in Modal Order Reduction Techniques with Applications in Finite Element Analysis, London, United Kingdom: Springer-Verlag, 2004, ch. 3, pp. 31-46.
23. U. Ölmez, "Sound and vibration analysis of diesel generators with coherence function", M. S. thesis, Dept Electrical and Electronics Eng, İstanbul Univ, İstanbul, Turkey, 2018.
24. Acoustics - Determination of Sound Power Levels of Noise Sources Using Sound Pressure - Engineering Method in an Essentially Free Field over a Reflecting Plane, ISO 3744: 2010.
25. Reciprocating Internal Combustion Engine Driven Alternating Current Generating Sets - Part 10: Measurement of Airborne Noise by the Envoloping Surface Method, ISO 8528-10: 1998.
26. Mechanical Vibration - Evaluation of Machine Vibration by Measurements on Non-Rotating Parts - Part 1: General Guidelines, ISO 10816-1: 1995.
27. P. R. Donavan, D. M. Lodico, "Measuring tire-pavement noise at the source", Petaluma, CA, USA, NCHRP Report 630, 2009. [CrossRef]

Uğur Ölmez was born in Istanbul on September 3, 1989. He received his B.Sc degree in Electrical and Electronic Engineering from Pamukkale University in 2013. He completed his M.Sc. degree in Electrical and Electronics Engineering from Istanbul University in 2018. Currently, he is working as a Senior R&D Engineer in R&D Center of Teksan Generator. His research interests are electric power generation, renewable energy technologies, genetic algorithm and signal processing.

Nevra Bayhan was born in Istanbul. She received her B.Sc. and M.Sc. degrees in Electrical and Electronics Engineering from Istanbul University in 1997 and 2001, respectively. She completed her Ph.D. in Control and Automation Engineering at Istanbul Technical University in 2008. Since 2011, she has been working at the Electrical and Electronics Engineering Department of Istanbul University as an Assistant Professor. Her research interests are automatic control systems, control systems design, robust control, time-delay systems, digital control systems, energy, low order controller design and control of systems with parameter uncertainties.

Hakan Doğan was born in Istanbul on October 28, 1978. He received his associate's degree in Electronics Department from Marmara University in 1998. He completed his B.Sc. degree in Mechanical Engineering at Ataturk University in 2002. Since 2014, he has been working at the R&D Center of Teksan Generator as a R&D Manager. His research interests are acoustic, vibration, CFD, FEM and energy.

Murat Uysal was born in Izmir on April 25, 1983. He received his B.Sc. degree in Mechanical Engineering from Suleyman Demirel University in 2004. Currently, he is working at the R&D Center of Teksan Generator as a R&D chief. His research interests are passive type exhaust silencers, sound attenuated enclosures, FEM, vibration and airborne noise reduction techniques.

İSTANBUL UNIVERSITY
CERRAHPAŞA

RESEARCH ARTICLE
Electrica 2019; 19(1): 85-90

Assisting 3D Indoor Positioning for Robot Navigation

Ban Isam Rashid Albayati, Serkan Kurt

Department of Electronics and Communication Engineering, Yıldız Technic University, İstanbul, Turkey

Cite this article as: Albayati BIR, Kurt S. Assisting 3D Indoor Positioning for Robot Navigation. *Electrica*, 2019; 19(1): 85-90.

ABSTRACT

With the increasing employment of mobile robots to achieve different tasks in various applications, the need for localization and body position for these robots is increasing rapidly. Many techniques are proposed to calculate the precise coordinates of a robot based on the distances measured between the robot and a set of reference points. Also, internal sensors, such as accelerometers and gyroscopes, are used to detect the body position and the direction of the robot. However, the effect of obstacles in an indoor environment and sensor drifts still limit the applicability of such systems. Thus, in this study, a novel technique that uses one or more robots to compensate for the missing stationary points is proposed. The robots in the proposed technique collaborate to improve the positioning accuracy, by providing reference points to each other. Per each movement execution of one robot, the remaining robots remain stationary, to provide the required reference points. When the robot finishes the movement execution, its position is updated based on the signals collected from the other robots, in addition to the position calculated by the onboard sensors. Then, another robot is selected to execute its movement.. The results show that the proposed method has been able to improve the positioning accuracy, by increasing the number of collaborating robots, when the median function if used to select the coordinates of the robot, among the candidate positions.
Keywords: Indoor positioning, majority vote, robots

Introduction

In recent years, the need for indoor positioning is rising rapidly, given the growing use of robots in accomplishing different tasks. In general, global positioning system (GPS) is used in most tasks that require positioning objects outdoors. This system uses radio waves transmitted from specialized GPS satellites orbiting around the earth. Even in outdoor positioning, the accuracy of the position computed by the GPS can vary from a few meters to tens of meters, which is not accurate enough with respect to indoor scales. Moreover, the radio waves transmitted from the GPS satellites are difficult to receive indoors, considering the obstacles they need to pass through in order to reach the receiver [1]. Thus, several studies are proposed recently to provide alternative systems for indoor positioning.

Similar to the methodology used in GPS, indoor positioning uses known coordinates as reference points to calculate the new coordinates for the object being positioned. This positioning relies on computing the distances between the given object and each of the reference points in range of that object. The new coordinates are calculated by finding all the coordinates that satisfy the measured distances from these points. Most of the earlier studies emphasize on developing techniques that improve the accuracy of the distance measured from the reference points to improve the accuracy of the calculated coordinates. Obstacles between the object and the reference points, from which the distance is being calculated, is one of the most crucial factors that affect the accuracy of the measured distance, hence, the accuracy of the calculated position [2-4].

In this study, a method is proposed to allow positioning robots that have lost communication with one or more of the stationary reference points. The remainder of this study is organized as follows: Section Two reviews previous studies related to this one; Section Three describes the proposed methodology and the computations behind it; Section Four summarizes the

Corresponding Author:
Ban Isam Rashid Albayati

E-mail:
albayati.ban90@gmail.com

Received: 25.10.2018

Accepted: 12.01.2019

DOI: 10.26650/electrica.2019.18038

experiments conducted to evaluate the performance of the proposed method, and the results gathered from these experiments; Section Five shows the conclusions acquired from this study.

Related Work

An indoor positioning technique is proposed by Zhang et al. [5] that uses visible light to send on-off keying (OOK) messages to the receivers from light-emitting diode (LED) bulbs. Each bulb sends an identifying message that can be used to retrieve the position of that bulb in a specific time slot, to avoid receiving more than one message by the receiver. By measuring the intensity of the light at the receiving end and the angle that the light is projected on the sensor, the linear least square estimation method is used to calculate the position of the object. The results of this method show that a positioning accuracy of up to 5.9 cm can be achieved, using such a technique in an environment with indirect sunlight and proper installation of the LED bulbs. However, the visible light is highly affected by obstacles that may interrupt the line of sight between the bulb and the receiver and prevent the receiver from considering that reference point, or by receiving a reflection of the light that results in a wrongfully calculated distance.

The method proposed by Wang et al. [6] uses WiFi signals transmitted from access points (AP) located in known positions to calculate the position of an indoor object. The distance between the object and each AP is calculated by measuring the power of the received WiFi signal. Then, a *k*-nearest neighbor (*k*-NN) classifier is used to integrate pseudo-odometry (P-O) with the WiFi data to eliminate the effect of obstacles, using measurements collected using pedestrian dead-rocking simulation. The results of the experiments show that a one-meter accuracy can be achieved using this approach. However, the use of the *k*-NN classifier to reduce the effect of the obstacles in the building imposes the need of collecting new simulation data for that classifier, whenever the location of the obstacles in the building are changed.

Lin et al. [7] propose an indoor positioning system that uses Bluetooth low-energy (BLE) device to transmit beacons that include identification information about the device transmitting those beacons. It is possible to position the object based on the positions of the BLE devices in range with the object by identifying that device and the distance between it and the receiving object and by measuring the received signal strength (RSS). Instead of calculating the exact coordinates of the object, the proposed system partitions each region into four sub-regions, where the position of the object is described by the sub-region that it is predicted to be in. This system is proposed to increase the efficiency of the services provided in an emergency room, which illustrates the importance of some indoor positioning applications. As the BLE devices transmit a beacon every second, the position is updated once every five seconds, in which five beacons are received in order to reduce the effect of the noise. The results show that 97.22% of the predicted positions in this technique are correct. However, as the position of the object is described using the sub-region that it is located in, no coordinates are calculated for the object to measure the accuracy of that positioning.

In addition to the coordinates of the robot, it is also important to calculate the angle and the direction that the robot is heading, in order to calibrate the gyroscope and accelerometer on the robot for short-term navigation. By calibrating these sensors, the robot gains the ability to navigate without the need of stationary points. However, such navigation suffers from drifting, in which the error caused by noise signals collected from these sensors are accumulated [8]. Different techniques are proposed to minimize such drifting, where the use of Kalman filter has shown better results by eliminating the noise from the signals collected from the sensors [9]. However, in the case of multiple robots existing in one domain, the collaboration between these robots can improve the position computations, where each robot uses the positions of other robots, calculated based on their gyroscopes and accelerometers.

Method

To calculate the 3-dimensional coordinates of an object using reference points, the distance between that object and a minimum of four reference points, alongside with their coordinates, is required. By measuring the distance between the object and a single reference point, the object may have coordinates that position it anywhere in the circumference of a sphere centered at each reference point, with a radius equal to the measured distance. Using another reference point, the object may have coordinates that position it anywhere in the circle that results from intersecting the spheres centered at these reference points. Using the third reference point, the coordinates are limited to only two possible locations, which are at intersects of the circle computed from the first two points with the sphere of the third. To obtain the coordinates of the object between these two candidate points, a fourth sphere centered at the fourth reference point is used, where the point that belongs to the circumference of that sphere is selected among those two candidates. The equation of the sphere centered at the reference point with coordinates (x_1, y_1, z_1) and radius of r_1 is shown as

$$(x - x_1)^2 + (y - y_1)^2 + (z - z_1)^2 = r_1^2 \quad (1)$$

Using (1) and the equations of spheres from other reference points, the following can be concluded.

$$x^2 - 2xx_1 + x_1^2 + y^2 - 2yy_1 + y_1^2 + z^2 - 2zz_1 + z_1^2 = r_1^2 \quad (2)$$

$$x^2 - 2xx_2 + x_2^2 + y^2 - 2yy_2 + y_2^2 + z^2 - 2zz_2 + z_2^2 = r_2^2 \quad (3)$$

$$x^2 - 2xx_3 + x_3^2 + y^2 - 2yy_3 + y_3^2 + z^2 - 2zz_3 + z_3^2 = r_3^2 \quad (4)$$

$$x^2 - 2xx_4 + x_4^2 + y^2 - 2yy_4 + y_4^2 + z^2 - 2zz_4 + z_4^2 = r_4^2 \quad (5)$$

To eliminate the squares of the variables x^2, y^2 and z^2, (5) is subtracted from (2), (3), and (4) which illustrates the use of the fourth reference point to select one of two candidate points calculated using

$$x(2x_1 - 2x_4) + y(2y_1 - 2y_4) + z(2z_1 - 2z_4) = r_4^2 - r_1^2 + x_1^2 - x_4^2 + y_1^2 - y_4^2 + z_1^2 - z_4^2 \quad (6)$$

$$x(2x_2 - 2x_4) + y(2y_2 - 2y_4) + z(2z_2 - 2z_4) = r_4^2 - r_2^2 + x_2^2 - x_4^2 + y_2^2 - y_4^2 + z_2^2 - z_4^2 \quad (7)$$

$$x(2x_3 - 2x_4) + y(2y_3 - 2y_4) + z(2z_3 - 2z_4) = r_4^2 - r_3^2 + x_3^2 - x_4^2 + y_3^2 - y_4^2 + z_3^2 - z_4^2 \quad (8)$$

$$\begin{bmatrix} (2x_1 - 2x_4) & (2y_1 - 2y_4) & (2z_1 - 2z_4) \\ (2x_2 - 2x_4) & (2y_2 - 2y_4) & (2z_2 - 2z_4) \\ (2x_3 - 2x_4) & (2y_3 - 2y_4) & (2z_3 - 2z_4) \end{bmatrix}^{-1} \times \begin{bmatrix} (r_4^2 - r_1^2 + x_1^2 - x_4^2 + y_1^2 - y_4^2 + z_1^2 - z_4^2) \\ (r_4^2 - r_2^2 + x_2^2 - x_4^2 + y_2^2 - y_4^2 + z_2^2 - z_4^2) \\ (r_4^2 - r_3^2 + x_3^2 - x_4^2 + y_3^2 - y_4^2 + z_3^2 - z_4^2) \end{bmatrix} = \begin{bmatrix} x \\ y \\ z \end{bmatrix} \quad (9)$$

the other reference points, i.e., the square root of these variables, where $\sqrt{x^2} = \pm x$, for example. This subtraction results the equations (6), (7) and (8). The values of *x*, *y*, and *z*, which represent the coordinates of the object, can then be calculated from these equations using the matrices operations shown in (9). Regardless of which equation is subtracted from the other equations, the described procedure always results in the same coordinates. However, the use of a fifth reference point can result in four different combinations of equations that can be used to calculate four coordinates for the object. Moreover, when a new reference point is added to the existing set of points, four more combinations can be added to the calculations of the position, which results in a more accurate computation.

Moreover, as each robot has a gyroscope and an accelerometer that can be used to calculate the distance traveled by the robot, with respect to the last known position, the last position of the robot can also be considered as a reference point, while the distance from that point is calculated using the onboard sensors. However, the effect of the drifting can occur in these sensors, resulting in an inaccurate positioning, unless other reference points are used to improve the positioning accuracy. Thus, in addition to the use of the onboard sensors to calculate the distance traveled by the robot, it is possible to use only three reference points to position the robot but a perfect positioning accuracy cannot be guaranteed, when considering the drifting effect.

In the proposed method, the robot is expected to have access to four reference points under normal operation. However, in certain conditions, the robot may end up in certain positions where the stationary reference points are no longer accessible. At such positions, one or more robots are sent to assist the stuck robot in recalculating its position. By making use of the collaboration among these devices, it is possible to improve the accuracy of the positioning of each of these robots.

When one robot moves, the remaining robots are required to stay in stationary, i.e., they do not change their positions. As soon as the requested movement command is completed by the first robot, according to the measurements collected from the gyroscope and the accelerometer, this robot becomes stationary as well. Then, the coordinates of its new position are calculated based on the measurements collected from its sensors as well as the distances collected from the other robots and stationary reference points, if they exist. The calculated position is then used by this robot instead of the older coordinates, calculated based on the gyroscope and the accelerometer. At this instance, a command is sent to another robot to execute the required movement.

As the ratio of robots used to assist the positioning process increases, the effect of drifting that occurs in the onboard sensors of the calculated coordinates increase, with respect to the stationary reference points. However, as the total number of reference points used in the coordinate's calculations, including the last position and the distance measured using the onboard sensors, exceeds four reference points, multiple candidate positions can be calculated. Selecting certain coordinates from the candidates list can be achieved by averaging these candidates, or by selecting the median value.

Experiments

To evaluate the performance of the proposed method, a model is created using MATLAB development environment. A mobile robot is simulated to travel from a position where the positioning process relies on four stationary reference points to a position where no stationary reference points are accessible. Thus, the robot starts losing the signals incoming from these stationary points, one by one.

As soon as the first signal is lost, the robot starts to use its onboard accelerometer and gyroscope to calculate the distance traveled from one position to another. However, another robot is sent to that robot to assist in the positioning process, and by performing various random motions while depending on its onboard accelerometer and gyroscope, the stuck robot can calculate its new location. When another signal is lost, another assisting robot is sent, until the entire positioning process becomes based on the collaborating robots, while the stationary reference points have no role in the positioning process. When a robot is moving, the positions of the remaining robots are fixed. A maximum of 1% of the traveled distance is simulated as an error in the calculated distance between the current and previous positions, to cover the drifting effect of the onboard sensors.

When more than one candidate set or coordinates are available, the position of the robot is selected using the average and median functions. By the end of the trip, the mean error in the actual and calculated positions is calculated for the positions of both functions. The robot is set to travel to the destination coordinates in five steps. Per each step the position

of the robot is fixed and the remaining robots are moved, one by one. Per each position where a robot requires assistance, three robots are used to evaluate the positioning accuracy. The first robot requires the use of onboard sensors to satisfy the minimum of four reference positions. The second robot allows the computations using four reference points, including the onboard sensors, while the third robot acts as an extra in order to achieve a more precise computation. The mean error per each experiment, for the average and median functions, is shown in Table 1.The results show that the use of the median function has been able to achieve more accurate positioning. In addition to the known immunity of the median function against noise values, the use of the average function to select the position of the robot from the candidate coordinates has reduced the positioning accuracy. This reduction is a result of the accumulated drifting that occurs in the accelerometer and gyroscope sensors. Moreover, the results show that the positioning accuracy based on the median function increases when the number of assisting robots are increased, but it is reduced when the average function is used instead.

Table 1. Mean error measured for the different steps of the robot

Reference Points		Mean Error (%)	
Stationary	**Robots**	**Average**	**Median**
4	0	0	0
3	0	0.17	0.17
3	1	0.23	0.07
3	2	0.21	0
2	1	0.34	0.34
2	2	0.34	0.13
2	3	0.29	0.08
1	2	0.42	0.42
1	3	0.56	0.38
1	4	0.58	0.31
0	3	0.77	0.76
0	4	0.78	0.59
0	5	0.83	0.46

Conclusion

The focus on indoor positioning is increasing recently, based on the rapid growth of using automated robots in different tasks. Many techniques are proposed to provide these robots with precise coordinates by measuring the distance between each robot and a set of stationary reference points, located in known positions in the environment, or based on the onboard accelerometer and gyroscope sensors. However, obstacles in the environment are one of the primary challenges that are faced by indoor positioning techniques, whereas an obstacle may block the communication between the robot and the reference points or affect it sufficiently to result in wrong distance measurements, while drifting is the main problem that faces the use of onboard sensors to calculate the coordinates of the robot. This drifting occurs due to the accumulating effect of noise signals collected by the sensors.

Moreover, robots that end up in blind spots, where the number of stationary reference points that are within the range of the robot in that environment is not sufficient to accurately calculate the coordinates, can no longer calculate their positions. Relying on the onboard sensors accumulates to significant differences between the calculated and actual coordinates. Thus, a contemporary technique is proposed in this study to enable robots of being positioned with the assistance of a designated one or more robot that transmit signals similar to those transmitted by the stationary reference points and uses their positions to assist robots that have lost communication with the stationary reference points calculating their positions.

The results of the simulated model show that the collaboration among the robots to improve their positioning accuracy has significantly improved when the median function is used to select the coordinates of a robot from the candidate coordinates. The existence of more than three external reference points, other than the use of onboard sensors and previous positions, can produce multiple candidate positions. The average and median functions are used to calculate the coordinates of the robot, based on those candidates. The average function has shown high sensitivity to the accumulated error of the onboard sensors, which is accumulated further when the robot executes other steps. However, the median function has been able to eliminate such accumulations by improving the positioning of each step.

Increasing the number of robots that collaborate in the positioning process has improved the positioning accuracy when the median function is used in the computations, while this accuracy is reduced when the average function is used. This behavior in the average-based computations is caused by the accumulating error caused by the drifting of all the sensors on the robots, where each robot executes its own movement while the others are in stationery. In the median-based computations, the error is limited to the drifting that occurs in the robot that have the selected coordinates.

As a future work, the ability of sending one or more robot to a position where the stationary reference points are accessible may be evaluated. Such an approach can be used to reset any accumulated drifting that occurs in the computations in order to improve the positioning accuracy.

Peer-review: Externally peer-reviewed.

Conflict of Interest: The authors have no conflicts of interest to declare.

Financial Disclosure: The authors declared that this study has received no financial support.

References

1. R. Momose, T. Nitta, M. Yanagisawa, N. Togawa, "An accurate indoor positioning algorithm using particle filter based on the proximity of bluetooth beacons", in Consumer Electronics (GCCE), 2017 IEEE 6th Global Conference, pp. 1-5, 2017. [CrossRef]
2. S. He, S. H. G. Chan, "Wi-Fi fingerprint-based indoor positioning: Recent advances and comparisons", IEEE Communications Surveys & Tutorials, vol. 18, pp. 466-490, 2016. [CrossRef]
3. A. Alarifi, A. Al-Salman, M. Alsaleh, A. Alnafessah, S. Al-Hadhrami, M. A. Al-Ammar, eAl-Khalifa HS, "Ultra wideband indoor positioning technologies: Analysis and recent advances", Sensors, vol. 16, p. 707, 2016. [CrossRef]
4. P. Nazemzadeh, F. Moro, D. Fontanelli, D. Macii, L. Palopoli, "Indoor positioning of a robotic walking assistant for large public environments", IEEE Transactions on Instrumentation and Measurement, vol. 64, pp. 2965-2976, 2015. [CrossRef]
5. W. Zhang, M. S. Chowdhury, M. Kavehrad, "Asynchronous indoor positioning system based on visible light communications", Optical Engineering, vol. 53, p. 045105, 2014. [CrossRef]
6. J. Wang, A. Hu, C. Liu, X. Li, "A floor-map-aided WiFi/pseudo-odometry integration algorithm for an indoor positioning system", Sensors, vol. 15, pp. 7096-7124, 2015. [CrossRef]
7. X.-Y. Lin, T.-W. Ho, C.-C. Fang, Z.-S. Yen, B.-J. Yang, F. Lai, "A mobile indoor positioning system based on iBeacon technology", in Engineering in Medicine and Biology Society (EMBC), 2015 37th Annual International Conference of the IEEE, pp. 4970-4973, 2015.
8. L. P. N. Sekar, A. Santos, O. Beltramello, "IMU Drift Reduction for Augmented Reality Applications", in International Conference on Augmented and Virtual Reality, pp. 188-196, 2015.
9. M. Narasimhappa, A. D. Mahindrakar, V. C. Guizilini, M. H. Terra, S. L. Sabat, "An improved Sage Husa adaptive robust Kalman Filter for de-noising the MEMS IMU drift signal", in Indian Control Conference (ICC). 2018, pp. 229-234, 2018. [CrossRef]

Ban Isam Rashid Albayati received the B.Sc. degree in computer engineering from Al Yarmouk University College, Baghdad, IRQ, in 2012. Since 2015 She is a student the M.Sc. degree in of Electronics and Communication Engineering programme , Institute of Natural And Applied Sciences, YTU.

Serkan Kurt was born in Kirikkale in 1976. He has obtained his B.Sc in Electrical and Electronics Engineering from Istanbul University in 1999. He has obtained M.Sc degree in Computer Engineering from Gebze Technical University in 2002. He has obtained Phd degree in Electrical Engineering in Yildiz Technical University in 2007. His areas of research includes Sensor Network, Control and Automation, Robotics, System Design. He has been working at Yıldız Technical University since 2002.